

DOT/FAA/TC-20/1

Federal Aviation Administration
William J. Hughes Technical Center
Aviation Research Division
Atlantic City International Airport
New Jersey 08405

Simplified Joint Modeling for Large-Scale Crashworthiness Structures—Single-Point Load Transfer

April 2020

Final Report

This document is available to the U.S. public through the National Technical Information Services (NTIS), Springfield, Virginia 22161.

This document is also available from the Federal Aviation Administration William J. Hughes Technical Center at actlibrary.tc.faa.gov.



U.S. Department of Transportation
Federal Aviation Administration

NOTICE

This document is disseminated under the sponsorship of the U.S. Department of Transportation in the interest of information exchange. The U.S. Government assumes no liability for the contents or use thereof. The U.S. Government does not endorse products or manufacturers. Trade or manufacturers' names appear herein solely because they are considered essential to the objective of this report. The findings and conclusions in this report are those of the author(s) and do not necessarily represent the views of the funding agency. This document does not constitute FAA policy. Consult the FAA sponsoring organization listed on the Technical Documentation page as to its use.

This report is available at the Federal Aviation Administration William J. Hughes Technical Center's Full-Text Technical Reports page: actlibrary.tc.faa.gov in Adobe Acrobat portable document format (PDF).

Technical Report Documentation Page

1. Report No. DOT/FAA/TC-20/1	2. Government Accession No.	3. Recipient's Catalog No.	
4. Title and Subtitle SIMPLIFIED JOINT MODELING FOR LARGE-SCALE CRASHWORTHINESS STRUCTURES—SINGLE-POINT LOAD TRANSFER		5. Report Date April 2020	
		6. Performing Organization Code	
7. Author(s) Olivares G., Zinzuwadia C., Keshavanarayana S., Bhasin A., Acosta, J.F.		8. Performing Organization Report No.	
9. Performing Organization Name and Address National Institute for Aviation Research Wichita State University 1845 Fairmount Wichita, KS 67260-0093		10. Work Unit No. (TRAIS)	
		11. Contract or Grant No.	
12. Sponsoring Agency Name and Address FAA Orlando CMO-29 8427 South Park Cir, Ste 500 Orlando, FL 32819		13. Type of Report and Period Covered	
		14. Sponsoring Agency Code AIR-600	
15. Supplementary Notes The FAA William J. Hughes Technical Center Aviation Research Division COR was Allan Abramowitz.			
16. Abstract Although powerful finite element modeling (FEM) computing capabilities are currently available, several shortcomings still exist when it comes to modeling elemental structures such as rivets or bolts (fasteners) in large models. One short coming is that due to the size of the aircraft and number of fasteners it is not practical to model all the fasteners in detail. Therefore it is important to understand the limitations of simplified bolt modeling techniques under static and dynamic loading conditions. To accomplish this, the results of four simplified finite element (FE) joint models (SJMs)—pertaining to aircraft structural assemblies – were compared to those of a detailed three-dimensional (3D)/solid joint FE model (DJM). The DJM was validated using test data and served as the reference for the study. The four SJMs studied were a rigid beam element bolt model with a hole, a mesh independent spotweld beam model, a mesh independent spotweld beam with an elastic patch model and a rigid beam element bolt model with no hole. A single shear lap joint specimen under tension was used as the bases for the comparison. The load transfer (LT), failure modes, stresses, strains, energy levels, and bolt loads of the SJMs were compared to the results of the DJMDJM (at quasi-static loading). In addition, LT at higher loading rates (stroke rates) was also studied. A slack-inducer (SL) system was used to test the joint specimen at the higher stroke rates. A FEM of the SL system was required to capture the change in LT through simulation. The use of SJMs resulted in reasonable comparisons to those of the DJM and in significant savings in computational cost. Thus they may be employed for a quick evaluation of design concepts or for preliminary studies. For areas where detailed information is required, it is recommended to use a DJM. It is rather difficult, a priori, to determine if the a SJM will suffice as a replacement for the DJM, as they are subject to the end use and purpose of the particular overall model. SJMs have been used to model large structures successfully however a clear understanding of their limitations, selection and use are necessary.			
17. Key Words Simplified joint modeling techniques, Shear lap joint, Load transfer, Simplified joint modeling, Joint modeling		18. Distribution Statement This document is available to the U.S. public through the National Technical Information Service (NTIS), Springfield, Virginia 22161. This document is also available from the Federal Aviation Administration William J. Hughes Technical Center at actlibrary.tc.faa.gov .	
19. Security Classif. (of this report) Unclassified	20. Security Classif. (of this page) Unclassified	21. No. of Pages 147	22. Price

ACKNOWLEDGEMENTS

The authors would like to thank the project's technical monitor, Allan Abramowitz, from the FAA for his technical support throughout this project. The authors also thank the National Institute for Aviation Research Composite Lab staff for assistance with testing equipment.

The authors acknowledge the expert contributions of colleagues Nilesch Dhole, Luis Gomez, and Adrian Gomez for their expertise with testing and finite element modeling.

TABLE OF CONTENTS

	Page
EXECUTIVE SUMMARY	XV
1. INTRODUCTION	1
1.1 Approach	2
1.1.1 Definition of Specimen Used for this Study	3
1.2 Literature Review	5
1.2.1 Finite element Modeling of Bolted Joints	5
1.2.2 Experimental Research on Bolted Joints	6
1.2.3 Performance of Bolted Lap Joints	7
1.2.4 Factors Affecting Bolted Joints	8
2. EXPERIMENTAL TESTING	10
2.1 Clamping Force Measurements	11
2.1.1 Description of the HI-LOK Fastener System [37, 38]	11
2.1.2 Test Article	11
2.1.3 Test Setup and Procedure	12
2.1.4 Clamping Force Test Results	14
2.2 Material Characterization Tests	15
2.2.1 Test Specimen Geometry	15
2.2.2 Test Setup and Procedure	16
2.2.3 Test Results	17
2.3 LT Tests	17
2.3.1 Test Article	17
2.3.2 Test Setup and Procedure	18
2.3.3 LT Test Results	22
3. FINITE ELEMENT MODELING	24
3.1 Mesh Discretization	24
3.1.1 DJM	24
3.1.2 SJMs	26
3.2 Element Definitions	33
3.3 Boundary Conditions and Constraints	34

3.4	Contact Modeling	34
3.4.1	LS-DYNA Contact Option: *CONTACT_SPOTWELD	35
3.4.2	LS-DYNA Contact Option: *CONTACT_TIED_NODES_TO_SURFACE_OFFSET	36
3.5	Preload Application	37
3.5.1	Preload in Solid Bolt Model	37
3.5.2	Preload in Beam Bolt Model	37
3.6	Material Modeling	38
3.6.1	Material Strain-Rate Dependency	40
4.	FEM RESULTS	41
4.1	Calculations	41
4.1.1	LT for Simulations	41
4.1.2	LT by Bolt and by Friction	41
4.2	Quasi-Static	42
4.2.1	DJM	42
4.2.2	SJMs	47
4.3	High Speed	80
4.3.1	DJM	80
4.3.2	Mesh-Independent Spotweld Beam Model	92
5.	RESULTS AND DISCUSSION	102
5.1	Experimental Testing	103
5.2	Validation of FE Modeling Methods	103
5.3	Joint Performance at Quasi-Static Stroke rates - SJMS versus DJM	103
5.4	Joint Performance at high Stroke rates—Mesh-Independent Spotweld Beam Model Configuration 2B versus DJM	107
5.4.1	LT	107
5.4.2	Stresses and Strains	107
5.4.3	Fastener Loads	108
5.4.4	Energies	108
6.	CONCLUSIONS	109
7.	RECOMMENDATIONS AND FUTURE WORK	110

APPENDICES

A—HI-LOK™ FASTENERS DETAIL

B—SIMPLIFIED JOINT MODELING TECHNIQUES

C—LOAD TRANSFER TEST RESULTS

D—STRAIN COMPARISON FOR HIGHER STROKE RATES

LIST OF FIGURES

Figure	Page
1 LT test specimen	4
2 Main part dimensions	4
3 Transfer part dimensions	5
4 Single lap joint connected with a bolt, and the corresponding forces	7
5 Static force distribution in detailed 3D joint model	8
6 Plate with a circular hole	9
7 Failure modes in single-shear lap joint	10
8 HI-LOK fastener system	11
9 Test specimen for preload measurement	12
10 Test setup for preload measurement using load cell	13
11 Applied load vs. voltage from load cell tested on MTS machine	14
12 Clamping force vs. torque for clearance fit hole	14
13 Clamping force vs. torque for interference fit hole	15
14 Bolt condition after preload test	15
15 Geometry of specimen used for material characterization	16
16 Material characterization test setup	16
17 Stress vs. strain (from SG) for aluminum 2024-T3 clad at 0.05 inch/min	17
18 Stress vs. strain (from extensometer) for aluminum 2024-T3 clad at 0.05 inch/min	17
19 ABF for LT tests	18
20 LT test setup	19
21 High-rate servo hydraulic MTS testing machine at NIAR	21
22 SL mechanism fabricated at WSU/NIAR	21
23 SG locations on LT specimen	22
24 LT test results comparison for different stroke rates	23
25 Failure on specimen for the LT test for QS stroke rate	24
26 DJM setup	25
27 FE discretization of main part and transfer part of LT specimen	25
28 FE discretization of HI-LOK bolt and nut	26
29 FE discretization of doubler and ABF	26
30 Model setup of RBE joint model	27

31	Variations of RBE joint models	28
32	FE model setup of mesh-independent spotweld beam joint model	29
33	Variations of mesh-independent spotweld beam joint model—same mesh on main part and transfer part	29
34	Variations of mesh-independent spotweld beam joint model—different mesh on main part and transfer part	30
35	FE model setup of mesh-independent spotweld beam model with EP	31
36	Variations of mesh-independent spotweld beam model with EP model	31
37	FE model setup of RBE joint model with no hole	32
38	Variations of RBE joint model with no hole	33
39	FE model boundary conditions for LT specimen	34
40	Components of *CONTACT_SPOTWELD	35
41	Shape functions for *CONTACT_SPOTWELD	36
42	Preload on solid bolt model	37
43	Preload on beam bolt model	38
44	Effective stress vs. effective plastic strain for aluminum 2024-T3 at quasi-static rate	40
45	Clad aluminum 2024-T3 material data for quasi-static and strain rate 187.5/s	40
46	CS plane locations on LT specimen for simulations	41
47	CS plane location on bolt for simulations	42
48	Comparison of DJM results to experiment results	43
49	Clamping stresses due to preload application on DJM	44
50	Von Mises stress on main part on DJM	44
51	LT by the bolt using the DJM	45
52	Axial force on bolt using the DJM	46
53	Energy levels using DJM for QS loading	46
54	Internal energy distribution using DJM at QS loading	47
55	LT comparison of RBE joint models with hole vs. DJM	48
56	Stresses due to preload on RBE joint model with hole	48
57	Von Mises stress comparison on main part in RBE joint models with hole	49
58	Axial strain vs. remote stress for DJM and RBE joint models with hole	50
59	Comparison of LT and shear force on bolt—DJM vs. the RBE joint models with hole	51
60	Comparison of axial force on bolt—DJM vs. RBE joint models with hole	52
61	Energy levels in RBE joint model with hole Configuration 1B at QS loading	53

62	Internal energy distribution in RBE joint model with hole Configuration 1B at QS loading	53
63	Comparison of strain energy per volume in main and transfer patch area for DJM vs. RBE joint models with hole	53
64	Comparison of strain energy in bolt shank for DJM vs. RBE joint models with hole	54
65	LT Comparison of solid and mesh-independent spotweld beam joint models with same mesh on main part and transfer part	54
66	LT Comparison of solid and mesh-independent spotweld beam joint models with different mesh on main part and transfer part	55
67	Contact points on main part vs. transfer part for analysis of mesh-independent spotweld beam	55
68	Nodes and elements affected by contact point on transfer part of mesh-independent spotweld beam model	56
69	LT comparison of mesh-independent spotweld beam models	56
70	Out-of-plane displacements (mm) of mesh-independent spotweld beam models on transfer part of Configuration 2B, 2L, 2M, and 2N	57
71	Stresses due to preload application in mesh-independent spotweld beam model with same mesh on main part and transfer part	58
72	Stresses due to preload application in mesh-independent spotweld beam models with different mesh on main part and transfer part	58
73	Von Mises stresses distribution in main part at failure initiation, for mesh-independent spotweld beam model configurations, with identical mesh on main and transfer part	59
74	Von Mises stresses distribution in main part at failure initiation, for mesh-independent spotweld beam model configurations, with different mesh on main and transfer part	60
75	Axial strain introduced in the DJM and the mesh-independent spotweld models for Configurations 2, 2A, 2B, and 2E	61
76	Axial strain introduced in mesh-independent spotweld models for Configurations 2K, }2L, 2M, and 2O	62
77	Comparison of LT by the bolt for the DJM and the mesh-independent spotweld beam models—identical mesh on main and transfer part	63
78	Comparison of LT by bolt for the DJM and the mesh-independent spotweld beam models—different mesh on main and transfer part	64
79	Axial load in the DJM and the mesh independent spotweld beam models	65
80	Energy level in spotweld beam model at QS loading for Configuration 2B	65
81	Internal energy distribution in spotweld beam model at QS loading for Configuration 2b	66
82	Strain energy per volume in a main part patch for spotweld beam models Configurations 2, 2A, 2B, and 2E	66

83	Strain energy per volume in the main and transfer patch area for the DJM and the spotweld beam models Configurations 2K, 2L, 2M, and 2O	67
84	Comparison of bolt internal energy for the DJM and the mesh-independent spotweld models	67
85	LT comparison of DJM and the mesh-independent spotweld beam models with EP	68
86	Stresses due to preload application of mesh-independent spotweld beam models with EP	68
87	Von Mises stresses on main part at initiation of failure of mesh-independent spotweld beam models with EP	69
88	Axial strain introduced in mesh-independent spotweld model with EP	70
89	Comparison of LT by bolt for the DJM and the mesh-independent spotweld beam models with EP	71
90	Comparison of axial force on bolt for the DJM vs. the mesh-independent spotweld beam models with EP	71
91	Energy level in spotweld beam model with EP at QS loading for Configuration 3B	72
92	Internal energy distribution in spotweld beam model with EP at QS loading for Configuration 3B	72
93	Strain energy per volume in the patch areas for the DJMs and the spotweld beam models with EP	73
94	Comparison of bolt internal energy for the DJM vs. spotweld beam models with EP	73
95	LT comparison of DJM vs. RBE joint models without hole	74
96	Stresses due to preload application of RBE joint models without hole	75
97	Von Mises stresses distribution in main part at initiation of failure for RBE joint models without hole	76
98	Axial strain introduced in the DJM and the RBE joint models without hole	77
99	Comparison of LT by bolt for the DJM vs. the RBE joint models without hole	78
100	Comparison of axial force on bolt for the DJM and the RBE joint models without hole	78
101	Energy levels in RBE joint model with no hole at QS loading for Configuration 4G	79
102	Energy levels in RBE joint model with no hole at QS loading for Configuration 4G	79
103	Strain energy per volume in patch areas for the DJM and the RBE joint models without hole	80
104	Comparison of bolt internal energy for the DJM and the RBE joint models without hole	80
105	LT Comparison at different stroke rates for DJM	81
106	LT comparison of DJM vs. test results at 100 in./s	81
107	Solid FE model with SL	82

108	LT Comparison at different stroke rates for DJM using SL	83
109	Load vs. displacement comparison of DJM with vs. without SL at 100 in./s stroke rate	83
110	LT results comparison for solid bolt model with SL vs. test results at 100 in./s	83
111	SL modeled with rubber washer	84
112	LT results for the SL model with rubber washer at 100 in./s	85
113	LT simulation results for DJM with rigid SL at 100 in./s	85
114	Von Mises stresses at failure initiation for DJM at different stroke rates	86
115	Von Mises stresses at failure initiation for DJM at different stroke rates—main part	86
116	Strain comparison for DJM at high stroke rate simulations	87
117	Strain comparison for DJM vs. test at 100 in./s stroke rate	88
118	Strain-rate comparison of test and DJM for different stroke rates at SG 1 location	89
119	Strain-rate comparison on main part patch area of DJM at different stroke rates	89
120	Comparison of bolt loads and LT by bolt for different stroke rates—DJMs	90
121	Total energy comparison for specimen at different stroke rates—DJM	91
122	Internal energy comparison for specimen at different stroke rates—DJM	92
123	LT comparison at different stroke rates for DJM vs. mesh-independent spotweld joint model Configuration 2B	93
124	Stress distribution of main part and maximum load for mesh-independent spotweld beam model Configuration 2B at different stroke rates	94
125	Strain comparison for high stroke rates for mesh-independent spotweld beam model Configuration 2B	95
126	Strain comparison of the mesh-independent spotweld beam model Configuration 2B to the DJM at 100 in./s stroke rate	96
127	Strain-rate comparison for mesh-independent spotweld beam model 2B vs. DJM for high stroke rates at SG 1 location	97
128	Strain-rate comparison for mesh-independent spotweld beam model 2B vs. DJM for high stroke rates near fastener	97
129	Comparison of bolt loads of the mesh-independent spotweld beam model 2B at different stroke rates	98
130	Energy distribution for different rates on specimen using—mesh-independent spotweld beam model Configuration 2B	99
131	Internal energy comparison for different stroke rates on specimen using mesh-independent spotweld beam model Configuration 2B	100
132	Joining mechanism showing two nodes constrained in the mesh-independent spotweld beam model Configuration 2B and solid elements in DJM	101

133	Plastic strain distribution at initiation of failure on main part of DJM for different stroke rates	101
134	Plastic strain distribution at initiation of failure on main part of mesh-independent spotweld beam model Configuration 2B for different stroke rates	102

LIST OF TABLES

Table		Page
1	Test matrix for LT tests and estimated clamping force	20
2	Mesh quality criteria	24
3	Mechanical properties of materials used in FE model	39
4	Element size and runtime summary of DJM and selected simplified RBE joint models	104
5	Comparison of remote stress at failure and energy after failure for solid and RBE joint models	105
6	Comparison of LT for solid and simplified joint models	106
7	Comparison of internal energy for high stroke rate simulations for the DJM vs. RBE Configuration 2B joint model	109

LIST OF ACRONYMS

ABF	Anti-buckling fixture
AC	Advisory Circular
CBA	Certification by analysis
CS	Cross section
DJM	Detailed three-dimensional (3D)/solid joint finite element model
EP	Elastic patch
FE	Finite element
FEM	Finite element modeling
LT	Load transfer
NIAR	National Institute for Aviation Research
RBE	Rigid body element
SG	Strain gauge
SL	Slack-inducer
SJM	Simplified finite element joint model
WSU	Wichita State University

EXECUTIVE SUMMARY

With recent improvements in computing technology, simulation of large structural models (aircraft) and associated complex event phenomena can be studied with the use of analytical tools such as finite element modeling (FEM). Therefore, there is a significant desire from the aircraft industry, academia, and certification authorities to use FEM in the design and certification process to minimize expensive testing and reduce the time to certification.

However, although powerful FEM computing capabilities are currently available, several shortcomings still exist when it comes to modeling elemental structures such as rivets or bolts (fasteners) in large models. One shortcoming is that, because of the size of the aircraft and number of fasteners, it is not practical to model all the fasteners in detail. Therefore, it is important to understand the limitations of simplified bolt modeling techniques under static and dynamic loading conditions.

To accomplish this, the results of four simplified finite element (FE) joint models (SJMs) pertaining to aircraft structural assemblies were compared to those of a detailed three-dimensional (3D)/solid FE joint model (DJM). The DJM was validated using test data and served as the reference for the study. The four SJMs studied were the rigid beam element bolt model with a hole (Configuration 1), the mesh-independent spotweld beam model (Configuration 2), the mesh-independent spotweld beam with an elastic patch model (Configuration 3), and the rigid beam element bolt model with no hole (Configuration 4). Configurations 3 and 4 are extensions of Configurations 2 and 1, respectively. A single-shear lap joint specimen under tension was used as the basis for the comparison. The load transfer (LT), failure modes, stresses, strains, energy levels, and bolt loads of the SJMs were compared to the results of the DJM (at quasi-static loading). In addition, LT at higher loading rates (stroke rates) was also studied. A slack-inducer (SL) system was used to test the joint specimen at the higher stroke rates. A FEM of the SL system was required to capture the change in LT through simulation.

In comparison to the DJM, the LT was up to 10% higher for Configuration 1, 9% higher to 17% lower for Configuration 2, 11% higher to 8% lower for Configuration 3, and 3% higher to 10% lower for Configuration 4. The SJMs were deemed to satisfactorily capture the LT. However, similar to the LT parameter, all of the parameters varied to some degree as compared to the DJM. Therefore, the selection of an acceptable SJM needs to be matched to the task at hand. The SJMs exhibited higher load-carrying capability than the DJM, mainly because of the absence of a modeled fastener hole (typically the weak point in a joint) and the effect of the joining methods (constraint-based methods) employed in the finite element analysis.

The test and model results also showed that higher stroke rates affected the LT. Further analysis of the DJM subjected to high-stroke rates revealed that at high strain rates, the total energy, total internal energy, stress fields, strains, and maximum load increased. However, the internal energy distribution changed with 10% less internal energy at the joint 1-inch patch area for 100 in/s stroke rate compared to quasi-static.

The use of simplified joints did result in significant savings in computational cost, and therefore may be employed for a quick evaluation of design concepts or preliminary studies. For areas in which detailed information is required, it is recommended to use detailed joint modeling methods.

It is rather difficult, a priori, to determine if the SJMs suffice as a replacement for detailed joint models because they are subject to the end use and purpose of the particular overall model.

Simplified joints have been used to model large structures successfully; however, a clear understanding of their limitations, selection, and use is necessary.

1. INTRODUCTION

Aircraft structures contain several subcomponents, such as sub-floor sections, engines, seats, and radomes, which require extensive destructive testing for certification purposes. Additionally, aircraft structures also require certification for events such as bird strike, lightning strike, and survivable crash scenarios. Physical testing of different subcomponents for events such as bird strike can be expensive because several variations exist for each case. With recent improvements in computing technology, simulation of such large structural models and associated complex event phenomena can be handled by analytical tools such as finite element (FE) modeling (FEM) [1–3]. Therefore, there is a significant desire from industry, academia, and certification authorities to use certification by analysis (CBA) in the design and certification process to minimize expensive testing [4–8] and reduce the time to certification.

CBA offers a rapid and less expensive way to evaluate design concepts and changes. CBA minimizes the requirement for physical testing by using baseline models over a range of scenarios. An example of CBA is Advisory Circular (AC) 20-146 [8], developed by the FAA for aircraft seat certification. As per the AC 20-146, FE models can replace physical testing when:

1. Demonstrating compliance to standard test requirements for changes to a baseline seat design.
2. Establishing the critical seat installation/configuration (configuration) in preparation for dynamic testing.

Large structural assemblies use fasteners as the primary joining entity to facilitate slip resistance and load transfer (LT) between joined parts [9–11]. Fasteners can be classified as either bolts or rivets, and although both have significant differences in appearance, structure, and installation methods, they serve the same purpose. Fastener joints are also common sites for fatigue crack initiations arising at the hole boundary because of stress concentrations resulting from bypass and bearing loads [11]. During a crash, a structure and its associated joints are required to fail in a controlled manner, to absorb energy and alleviate impact loading effects on occupants. In general, the energy is absorbed by the plastic collapse of thin-walled structures, which often contain fastener joints. Therefore, it is important to understand the behavior of fastener joints within a context for improving crashworthiness characteristics. Researchers have conducted several crash tests and generated FE models of large structural assemblies [3–4] to evaluate the survivability of the occupants, but little has been reported in terms of specific joint behavior and fastener failures.

Although powerful FEM computing capabilities are currently available, several shortcomings still exist when it comes to modeling elemental structures such as fasteners in large models [7] [12]. For example, the computational cost in any explicit FE software is controlled by the size of the mesh, specifically the minimum element length [13]. In aircraft structures, the size of a rivet or bolt is considerably small when compared to the full aircraft. Therefore, when an FE model of such size is generated, it is not practical to model all the fasteners in detail so the computational cost can be controlled. For example, in LS-DYNA, the minimum time step (Δt) is calculated using the minimum element length (l) and the wave speed through the material (C), as shown in equation 1 [13]. This indicates that the smaller the element length, the smaller the time step and, therefore, the higher the computational cost.

$$l = \Delta t \times C \quad [13] \quad (1)$$

Furthermore, modeling the fasteners in detail is a time-consuming task because the discretization of each component has to be controlled to ensure the mesh at fastener locations corresponds to the detailed fastener modeling method. As a result, FE models of large structures usually simplify the fastener joints by eliminating the subject clearance holes and idealizing the actual fastener with beam elements. The approximation of fasteners as beams can capture the simple mechanism of LT in a bolted joint to a certain extent. Nevertheless, the underlying mechanisms of a joint are in reality much more complex because of the presence of stress concentrations around the hole, clamp-force-induced friction at faying surfaces, fastener rotations, and end-fixity conditions on the fastener due to the presence of the head and nut [9, 10, 11, 14]. In addition, at times crashworthiness analyses require the consideration of dynamic strain-rate effects, which may also affect the behavior of the joint. Numerous studies, both experimental and analytical, have addressed these issues under fatigue and static loading conditions [14–17] but the consideration of high strain rates and dynamic loading is still open for investigation. To accurately simulate the effects of the above-mentioned mechanisms, a good quality FE model of the joint, capturing all the geometrical features with three-dimensional (3D) elements, is necessary. While providing useful information, it has been shown [5, 7] that such models are not practical when simulating large structural models. Today, the idealization of fasteners with simplified techniques is the only practical alternative solution for large FE models. With advancements in CBA, it is increasingly popular to use large models for crashworthiness analysis. Therefore, it is important to understand the limitations of simplified bolt modeling techniques under both static and dynamic loading conditions.

1.1 APPROACH

At a broader scale, this study of joints is aimed at understanding the limitations of simplified forms of joint modeling used for crashworthiness analysis, and to identify areas where improvements to simplified joint models can be made. Achieving this goal requires extensive research with many different aspects, such as studying riveted joints versus bolted joints, axially loaded fasteners, shear loaded fasteners in tension and compression, and performing component level tests and numerical analyses. Given that, this report specifically focuses on axially loaded single-shear bolted lap joints. The fastener is shear-loaded while the parts connected by the fastener undergo tensile loading.

In general, an FE model and analysis produces far more outputs than an experiment. Therefore, in this study, first, a detailed three-dimensional (3D)/solid finite element FE joint model (DJM) was used as a baseline for comparing simplified FE joint model (SJM) techniques. To obtain credibility for the DJM, it was important to compare it to experimental data. In addition, certain parameters, such as material properties, friction, and fastener preload, are required for accurate and predictive FE models. Such parameters can be obtained only from experiment or literature.

This investigation summarizes the experiments, validation of the DJM, and evaluation of simplified FE models for structural crashworthiness applications. The most basic structure comprising a joint—a lap shear specimen—is used for this study to characterize the load transferred at quasi-static and high-loading rates (stroke rates). To generate an accurate FE model for a lap shear joint, detailed material properties are required. Therefore, experiments were

conducted to characterize the subject material systems. Another important factor to consider is the bolt preload. The lap joint used within this investigation is secured using a HI-LOK™ bolt, which is designed for a fixed range of preload. The range specified by the manufacturer is fairly large; therefore, experiments were performed to quantify the bolt preload as related to this specific application. Finally, tensile tests were performed on the lap joint to evaluate its performance at quasi-static and high-stroke rates.

1.1.1 Definition of Specimen Used for this Study

The study was performed with a half dog-bone-type single lap shear assembly, as shown in figure 1. The assembly consisted of two parts, a main part and a transfer part, which were connected using a HI-LOK fastener [11] widely used in aircraft structural assemblies. A doubler was used to eliminate any eccentricity in loading of the specimen. An illustration of the assembled specimen, and the terminology used, is shown in figure 1. The specimen assembly used in this study has also been used by previous researchers [14, 18].

The main part that carries the applied load was a dog-bone-shaped coupon. It was gripped at one of the tab regions, where a constantly increasing displacement was applied until failure. When the load was transferred, the remaining load was carried by the bypass side of the coupon. The dimensions of the main part are shown in figure 2.

The LT part is a half dog-bone coupon, as shown in figure 3. Load was transferred from the main part to this part through the fastener and through friction between faying surfaces. The transfer part and the main part were gripped and constrained at the bypass end. Both the main part and transfer part were manufactured using 2024-T3 aluminum. The fastener was a HI-LOK system with an HL-18 steel pin and an HL-70 aluminum nut. Details of the pin and the nut can be found in appendix A. Note that the stiffness of the fastener pin was much greater than the stiffness of the plates it connects, and therefore fastener failure was not anticipated.

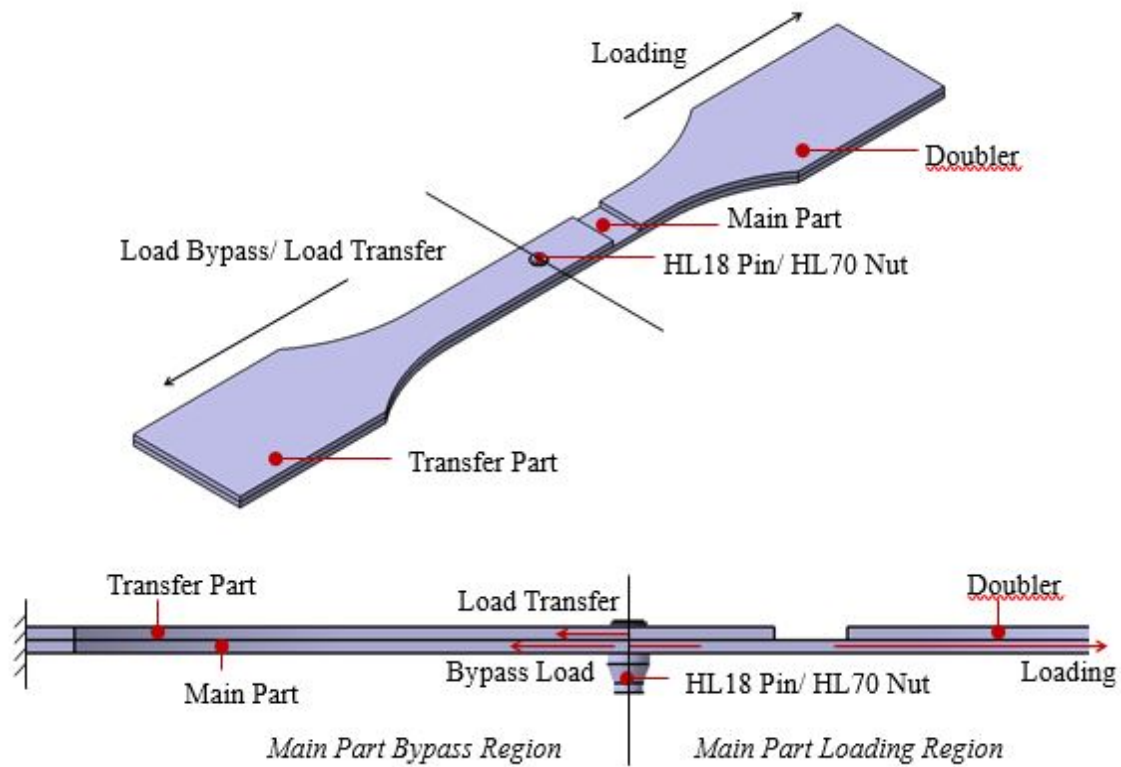
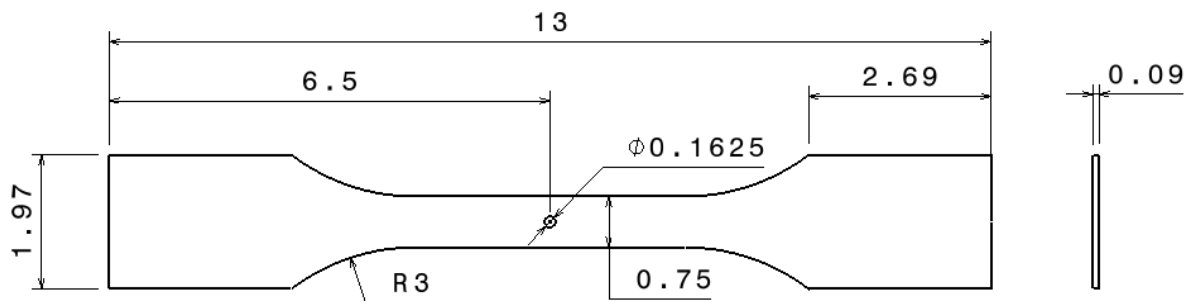
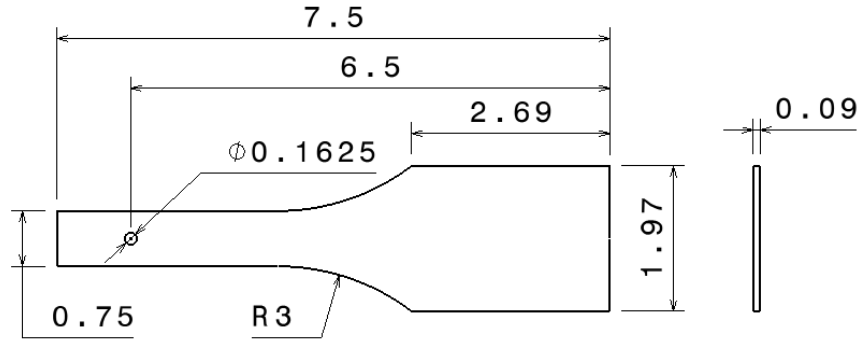


Figure 1. LT test specimen



Note: All Dimensions are in Inches

Figure 2. Main part dimensions [14]



Note: All dimensions are in Inches

Figure 3. Transfer part dimensions [14]

1.2 LITERATURE REVIEW

A thorough review of experimental and analytical investigation of joints was performed. In the following sections, a review of the FE modeling of joints and experimental testing of bolted lap joints is summarized. In addition, an overview of factors affecting the performance of bolted joints is also included.

1.2.1 Finite element Modeling of Bolted Joints

Research using FEM for detailed mechanical joint models[18–20] and simplified FE joint models [21–24] has been conducted under various loading conditions. Gadekar et al. [17] and U. Sonnenschein [25] have also developed ways of representing a bolt using simplified elements. Whereas these methods are simpler in terms of computation, they can be very tedious for large models because these methods use three to four different element and material types for defining a single joint. An illustration and a short description of several joint modeling methods is provided in appendix B.

Whereas each simplified joint model has its advantage and disadvantage, the simplified joints of interest are evaluated based on their applicability to large structural crashworthiness FE models. Based on the review of simplified methods, the best method for large FE models is the mesh-independent spot weld beam option [23, 26].

The effect of joint parameters such as clamp loads, coefficient of friction, and material plasticity on the LT and structural response of detailed joint systems was studied by Ghods [18] using FEM. The study was performed using a similar coupon assembly as used in this research. Ghods documented the LT, stress concentrations, and fastener rotation. This study was used as a baseline for designing experiments for this research.

The performance of SJM techniques—when compared to detailed joints—has been studied under both static and dynamic loading conditions [21, 24]. Kang, Kim, and Yoon [21] compared three simplified joint modeling techniques using static loading, bending and shear loading, and modal analysis. Major difference in stress distribution around the fastener hole was observed for static, bending, and shear loading. This research found up to 62% savings in computational time when

using simplified techniques. However, the detailed model provided the best results for modal analysis. Sonmez, Tanlak, and Talay [24] compared 11 different SJMs using an impact test. An impactor was dropped at the center of two plates fastened on each end and connected to a main frame. Sonmez et al. found 80% to 90% of computational time savings for SJMs. But the model—with fastener hole—most accurately predicted the behavior of the structure for various loading cases and mesh densities.

These studies highlighted the importance of inclusion of the fastener hole and the head and nut of the fastener in simplified joints for more accurate simulation results. However, in the present context of practicality for large FEM models undergoing dynamic crash analysis, both of these are not favorable because of computational constraints; therefore, this research studies the limitations of the alternate methods currently employed.

1.2.2 Experimental Research on Bolted Joints

Physical testing is a key aspect for any structural development. It is used for validation, certification, and documentation purposes. A variety of different tests by several researchers have been performed on bolted joints including, but not limited to, fatigue, tension, compression, dynamic loading, and torsion. The review of several previous tests on bolted joints provides insight into test methods and expected test outcomes.

In a study performed by Keshavanarayana et al. [14], medium LT specimens like those used in this study were joined using HI-LOK fasteners and were subjected to cyclic tension and compression loading at a quasi-static stroke rate. A clearance hole was used in the specimen with the HI-LOK fastener and LT was measured for the tension compression cycle. The specimen with the HI-LOK fastener experienced an initial drop in the percentage load transfer (%LT), after which the %LT stayed at slightly below 40% for the rest of the tensile loading phase.

Dynamic failure of structural joint systems has been extensively studied by Birch and Alves [27]. Several single lap-bolted specimens were tested at different stroke rates. The specimens were divided into two sets. Set-A specimens were connected using a bolt that had 3-mm socket diameter and 5.3-mm head diameter, and no washer was used. Set-B specimens were connected using a 5-mm diameter hexagon headed bolts with 9.7-mm diameter steel washers. The plates were constructed from 1-mm-thick cold rolled mild steel. A high-speed servo-hydraulic tensile test machine was used to load the specimens. In-plane shear load was introduced and measured using a high-frequency response piezoelectric load cell placed as close as possible to the grip mechanism. Displacements were measured using a linear variable differential transformer transducer located on the hydraulic ram of the test machine.

Similar failure patterns for both specimen sets were observed. For set A, the head of the bolt always pulled through the parent material. No change in failure mode with respect to pull velocity was observed. There was little bending across the lateral axis of the joined plates. The absorbed energy and mean loads increased significantly with respect to pull velocity. This could be attributed to material strain-rate sensitivity [27].

1.2.3 Performance of Bolted Lap Joints

When two plates are joined with a bolt, the bolt shank experiences pretension loads and, therefore, opposing clamping forces are introduced on the plates by the bolt head and nut. When an axially non-perpendicular force is applied, shear forces develop in the fastener, and bearing stresses and friction forces develop on the joined plates. Figure 4 shows the loads in a single-shear lap joint [17].

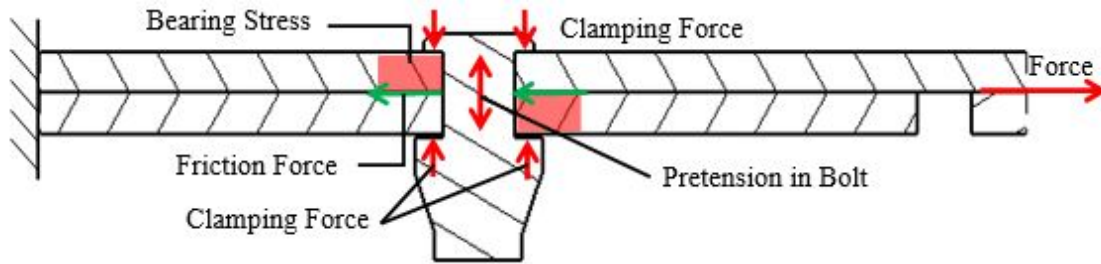


Figure 4. Single lap joint connected with a bolt, and the corresponding forces

The primary objective of mechanically fastened joints is to facilitate LT [11]. In doing so, many factors such as stress concentrations, secondary bending, fastener rotation, fastener bending, clamp loads, and friction affect the performance of the joint [11, 14, 28]. Many of these factors are also interrelated. A brief description of LT and factors that affect joint performance are provided in subsequent sections.

1.2.3.1 Load Transfer

In a single lap shear joint, when a force (F) is applied, because of the displacement compatibility between the main part and transfer part [11], F is divided into LT force (F_{transfer}) and bypass force (F_{bypass}). F_{bypass} is the load that remains in the main part, and F_{transfer} is the load that is transmitted to the transfer part. F_{transfer} is generated from a bearing force (F_{bearing}) resulting from pressure exerted by the bolt shank on the hole surface and a friction force (F_{friction}) resulting from mating of the sheets. Because of bolt preload, friction effects are largely localized under the bolt head and nut surface where maximum clamp force is distributed.

Figure 5 shows only a basic force distribution encountered by the specimen setup. Note that LT is a rather complex phenomenon, and factors such as the deformation of the hole, rotation of the joint, fastener bending, bolt clamp-up, hole preparation, and friction level will affect the LT [14, 18].

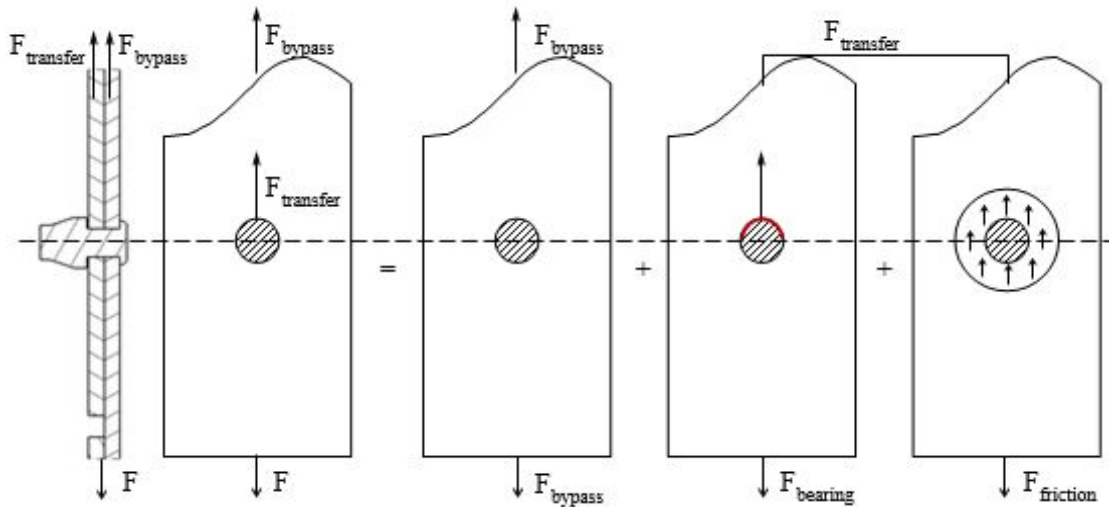


Figure 5. Static force distribution in DJM

1.2.4 Factors Affecting Bolted Joints

The static, dynamic, and fatigue performance of the joint under different loading conditions is affected by several parameters. Some of these parameters are discussed in this section.

1.2.4.1 Installation Parameters

The quality of the constituent joint components and the conditions induced on installation of these components have a significant effect on the performance on the joint [9]. In addition, many of these installation conditions are interrelated. Some of the installation parameters are: the surface condition and quality of the mating parts, fastener hole preparation (interference/clearance), fastener type and finish, and clamping load.

Surface finish(es) dictates the values of static and dynamic coefficients of friction on the faying surfaces of the joint. The strength of a shear joint is in turn dependent on these values [9]. Initial residual stresses in the plates due to the hole preparation, or cold working, also affect the strength of the joint.

Fastener hole preparation is also known to affect the strength and fatigue life of the joint. Interference-fit fastener holes have shown improved fatigue life compared to clearance-fit fastener holes [29].

Zeng L. and Haylock L. [30] have shown in their study that fastener coating and shear strength have an effect on the lap shear performance of the joint.

Clamping load is the load introduced to the fastened plates due to the tightening of the nut. Rivets have low clamping load relative to bolts, and that load cannot generally be controlled as well. Studies have shown that higher clamping load increases the fatigue life of joints [19]. Higher clamping load decreases the stress concentrations around the fastener hole and increases the slip resistance [19].

1.2.4.2 Loading Parameters

A joint can be designed for pure shear loads, tensile loads, or combined loading. In aircraft structures, combined and shear loading are common. The design of a joint can vary based on the principal load it experiences. The rate at which a joint is loaded also affects the strength of a joint. A study by Birch and Alves [27] shows that increasing pull velocity increased the mean load and the absorbed energy.

1.2.4.3 Stress Concentrations

Stress concentrations occur in loaded structures near section changes; examples are holes, grooves, notches, sharp corners, cracks, and other features [31]. Because of the presence of a fastener hole, stress concentrations are also expected in the single lap shear joint specimen of this study. In mathematical terms, a stress concentration factor (K_T) is defined as the ratio of the maximum localized stress (σ_{max}) to the nominal stress in the member (σ_{nom}), as shown in equation 2 [31].

$$\sigma_{max} = K_T \times \sigma_{nom} \quad (2)$$

In a plate with a circular hole, as shown in figure 6, it has been found that stress concentrations occur when $\theta = (1/2)\pi$ or $\theta = (3/2)\pi$ [31].

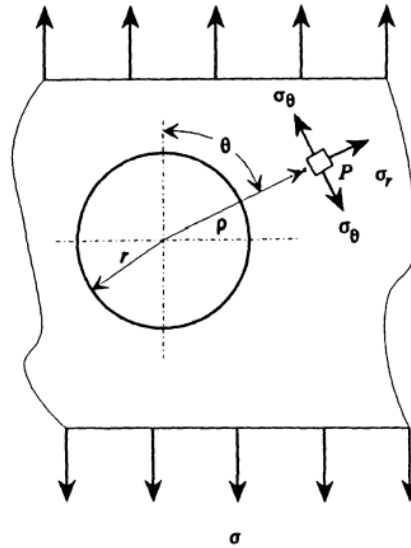


Figure 6. Plate with a circular hole [31]

Studies have shown that tensile load passing through the hole, bearing loads, and loads on the hole surface due to fastener bending and rotation contribute to the stress concentration factor of a fastener joint [15, 16].

1.2.4.4 Secondary Bending

Secondary bending is a phenomena that occurs in single lap shear joints in which the bolt and joint plates undergo bending due to loading eccentricities, resulting in a non-uniform stress distribution through the thickness of the joined plates [18, 28]. Experimentally, several ways of using strain gauges (SGs) to quantify secondary bending have been documented [14, 32]. In this study, because of limited resources, these methods have not been employed.

Local LT, fastener diameter, plate thickness, and clamping force are some of the parameters known to affect secondary bending [32–35]. Secondary bending is known to have a major effect on the fatigue life of single-shear joints [36].

1.2.4.5 Fastener Rotation/Bending

Fastener rotation/bending, commonly known as fastener flexibility, depends on the joint geometry, clamp loads, and the sheet and fastener materials [11]. It is an important parameter for determining the LT distribution in joints with multiple fastener rows [11]. Fastener rotation and bending are dependent on the end-fixity provided by head and nut, clamp force, induced friction, and material plasticity [18]. The joint compliance increases with excessive fastener rotation, causing a decrease in LT.

1.2.4.6 Failure Modes

Failure modes depend on the strength(s) of the joint members versus the strength of the bolt. It is also affected by the distance between the bolt and the edges [9]. In the case of single-shear lap joint, the following failure modes exist (also shown in figure 7):

- a. Tear out or marginal failure, in which bolts are too close to an edge of the plate.
- b. Net section failure, in which the plate is too thin, or soft compared to the bolt.

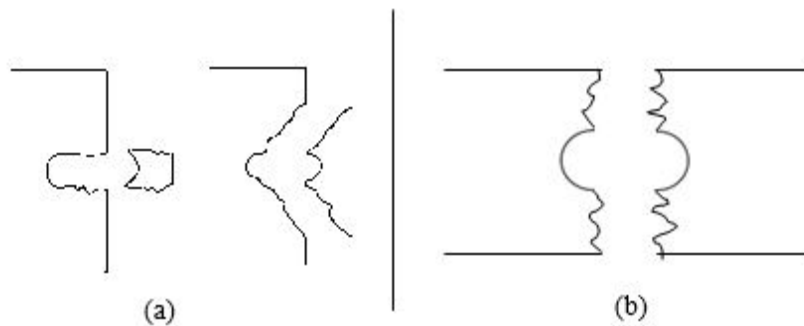


Figure 7. Failure modes in single-shear lap joint [9]

2. EXPERIMENTAL TESTING

This chapter contains information regarding the LT tests performed on a single lap joint specimen. As already mentioned, additional tests were conducted to quantify the clamping load introduced

on the specimen when the HI-LOK fastener was installed, and the material properties for the aluminum specimens under consideration.

2.1 CLAMPING FORCE MEASUREMENTS

The HI-LOK fasteners are designed for a fixed range of preload, but the manual specifies a large range [37, 38]. Ghods [18] found that fastener preload affects LT, stress concentration factors, and fastener rotations only at low levels of applied loading. He found that LT increases with increasing fastener preload, whereas the stress concentration factors decrease. Therefore, bolt preload was quantified to produce accurate FE models. The effect of fastener hole preparation was also studied. Fastener holes can be machined for an interference fit or a clearance fit. Therefore, plates with these two configurations were used for the experiments.

2.1.1 Description of the HI-LOK Fastener System [37, 38]

A HI-LOK fastener consists of a pin and a collar as shown in figure 8. HI-LOKs are designed with a predefined range of preload. To achieve the design preload the collar consists of a hex nut that shears off at a certain torque value. The process of fastening involves the use of a hex key that is inserted into the pin, which prohibits the pin from spinning. The torque on the nut is applied while the pin is held using the hex key. Therefore, this process requires the use of a box-end head for the torque wrench. It is important to ensure that the pin does not spin so that all the torque applied is used for fastening and not to overcome friction between the pin and the plates. The HI-LOK fastening system is shown in figure 8.

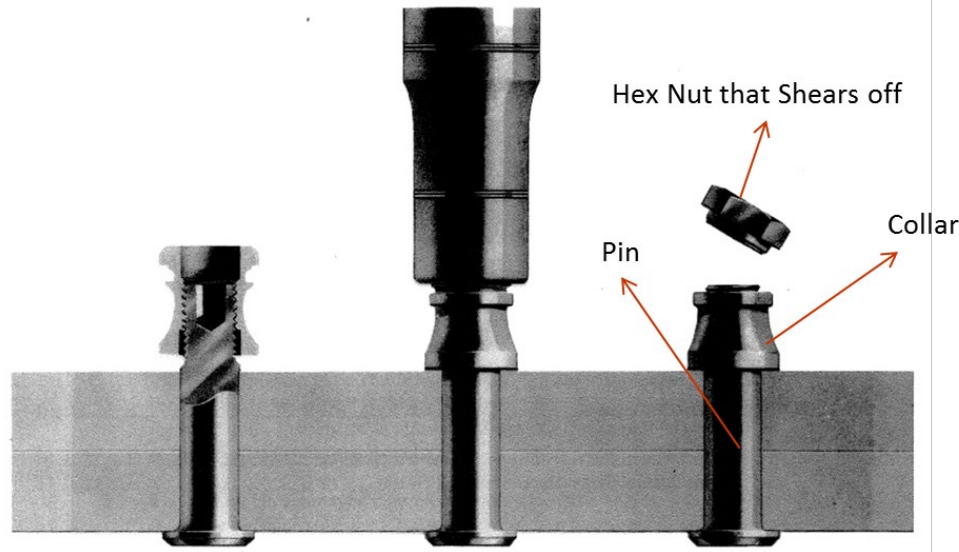


Figure 8. HI-LOK fastener system [39, 40]

2.1.2 Test Article

Chakherlou, Vand, and Oskouei [39] measured the clamping force of a bolted connection by placing an SG-mounted steel bushing between the plate and nut. This was possible because of the large size of the bolt. The nominal diameter of the pin used in this study is 0.1625 inch, and because

of its small size, the preload could not be directly measured at the fastener shank using a SG or another instrument. Therefore, a different test setup was designed to evaluate the clamping force. The test article assembly consisted of two aluminum plates of same thickness as the lap joint, HL18 pin, HL 70 nut, and a LWO-2 load cell [40]. The load cell was placed in between two plates, and the pin and nut were used to clamp the plates and the load cell together. The specimen assembly is shown in figure 9.

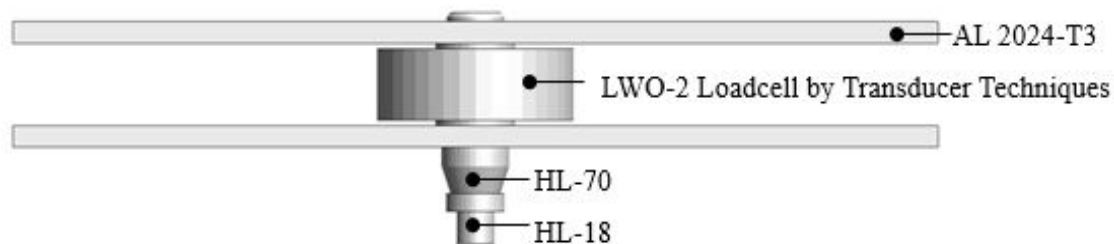


Figure 9. Test specimen for preload measurement

2.1.3 Test Setup and Procedure

To perform the test, the specimen assembly described previously was set up as shown in figure 10. The equipment used for the experiment was a vise, a TMO-2 signal conditioner, voltmeter, and a Tohnichi digital torque wrench [41]. The vise was used to clamp the specimen assembly. The load cell was connected to a signal conditioner, and the voltage output from the signal conditioner was read by a voltmeter. The digital torque wrench was used to torque the nut, and the maximum torque reading from the wrench—the torque at which the hex portion of the nut sheared off—was recorded.

Before setting up the test, the specimen dimensions were documented. The specimen assembly was then clamped using a vise. The load cell was connected to a signal conditioner, which was connected to a voltmeter for voltage output. The voltage output corresponds to a clamping load. The nut was then tightened using a torque wrench until the hex portion of the nut sheared off as described in section 2.1.1. The torque at which the nut sheared off and the corresponding voltage from the voltmeter were recorded. The clamping force was then determined by reading the voltage versus load plot, which was generated as described below.

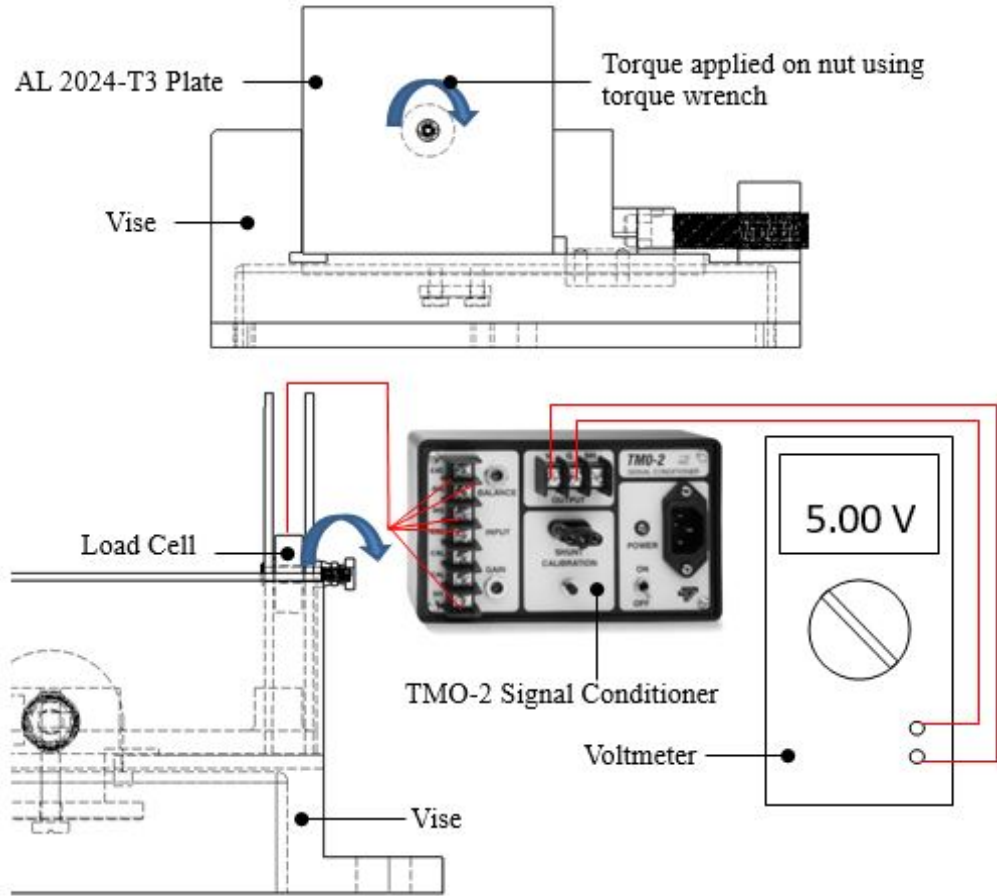


Figure 10. Test setup for preload measurement using load cell

2.1.3.1 Load Cell Verification and Signal Conditioner Calibration

Prior to using the load cell, a compressive load was applied on the load cell using a 5 kip MTS [42] test machine to verify the load-cell readings and to set the gain on the signal conditioner. The load cell was connected to the signal conditioner and a voltmeter, and the maximum limit load of the load cell (2400 lbf) was applied using the MTS machine [42]. The gain on the signal conditioner was adjusted until the voltmeter read 10 V. After setting the gain, a load versus voltage plot, shown in figure 11, was generated by performing several loading cycles on the load cell. This plot was used to generate equation 3, to convert the voltage recorded from the load cell to load value, as shown in the test setup in section 2.1.3.

$$V = 0.000927F_{\text{applied}} + 0.168241 \quad (3)$$

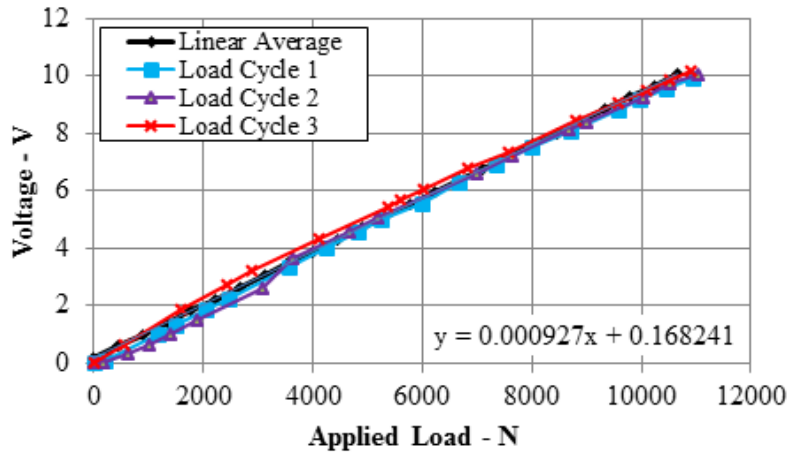


Figure 11. Applied load vs. voltage from load cell tested on MTS machine

2.1.4 Clamping Force Test Results

Fifteen samples were collected for each hole diameter configuration. A linear regression curve fit was created to fit the data points. Results for the clearance fit hole are shown in figure 12, and those for interference fit hole are shown in figure 13. Based on the results, clearance fit plates experienced higher overall clamping force compared to interference fit. During the test, it was noted that in the interference fit specimens, the coating (thin layer on the outside of the bolt) on the bolt was getting scraped on installation of the bolt to the plates, as shown in figure 14. In addition, interference fit will cause higher friction values between the hole surfaces and the bolt shank. As a result, lower clamping force is seen on interference fit specimens because some load is required to overcome the friction between the pin and the inner surface of the holes. No particular trend in torque versus clamping load is exhibited in the results for both clearance and interference fit. A linear fit of the interference data, shown in figure 13, resulted in equation 4. This equation will be used to evaluate the clamping force on the test specimens.

$$F_{clamp} = 1230.4T - 902.69 \quad (4)$$

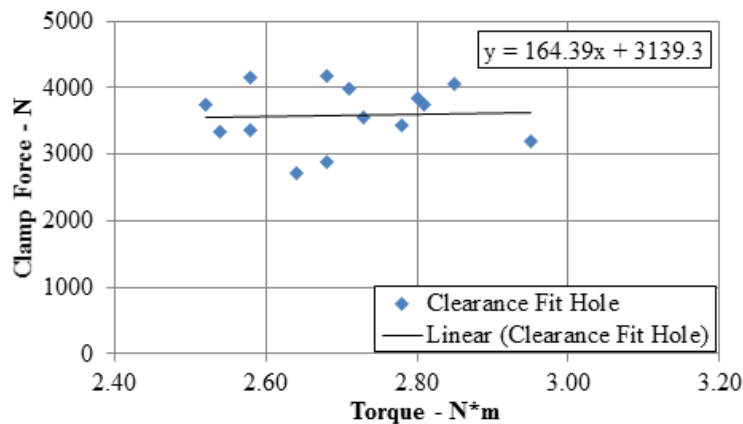


Figure 12. Clamping force vs. torque for clearance fit hole

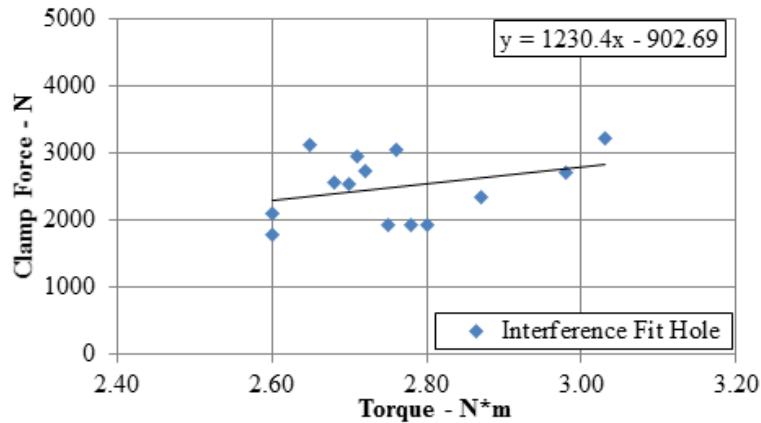


Figure 13. Clamping force vs. torque for interference fit hole

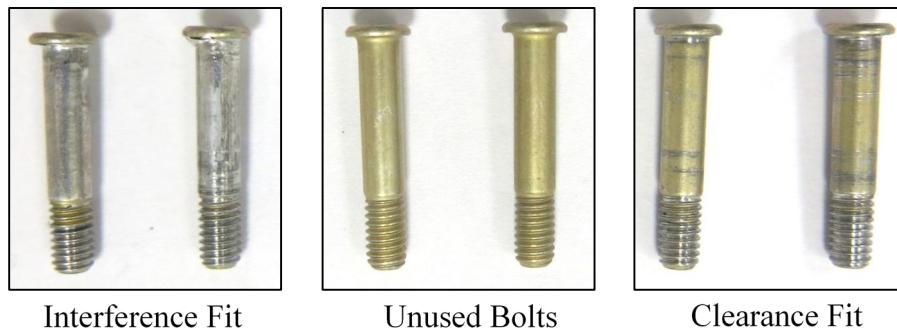


Figure 14. Bolt condition after preload test

2.2 MATERIAL CHARACTERIZATION TESTS

In the lap joint specimen used for this study, the HI-LOK bolt used was manufactured from steel, whereas the plates were manufactured from aluminum. This indicates that on loading, the aluminum plates are likely to undergo plastic deformations and failure. To accurately capture this behavior in the FE models, it was critical to obtain detailed material properties behavior. Therefore, coupons were extracted from the plates and standard tensile tests were performed.

2.2.1 Test Specimen Geometry

The specimens tested for material characterization were dog-bone shaped with an extended tab [43] manufactured from aluminum 2024-T3 with a nominal thickness of 0.09 inch, which is the same material and thickness of the plate used for the LT tests. Nominal dimensions of the specimen, tested for material characterization, are shown in figure 15.

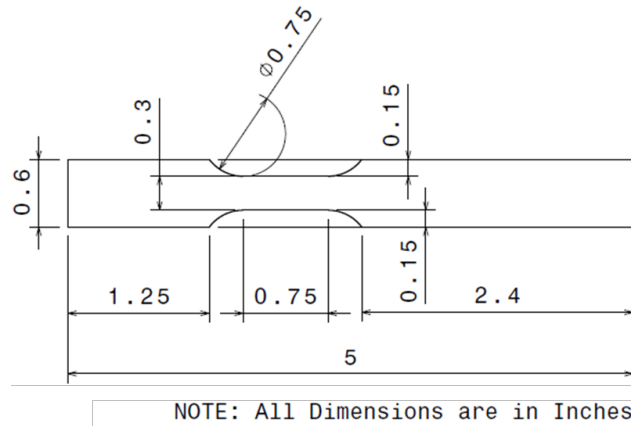


Figure 15. Geometry of specimen used for material characterization

2.2.2 Test Setup and Procedure

A servo-hydraulic universal test machine was used for the tensile test. The test system was a 22-kip MTS system with fixed grips. A CEA-06-250UN-350/P2 Vishay SG [44] was mounted on the center of the gauge section of five specimens. Because of the limitation of maximum strain reading by the SG, a laser extensometer was also used to capture the deformations until failure. The complete test setup with the laser extensometer is shown in figure 16. An initial preload of 20 lbf was introduced in the specimen. The test was conducted at a quasi-static rate of 0.05 inch/min. Five coupons were tested to ensure repeatability of test data.

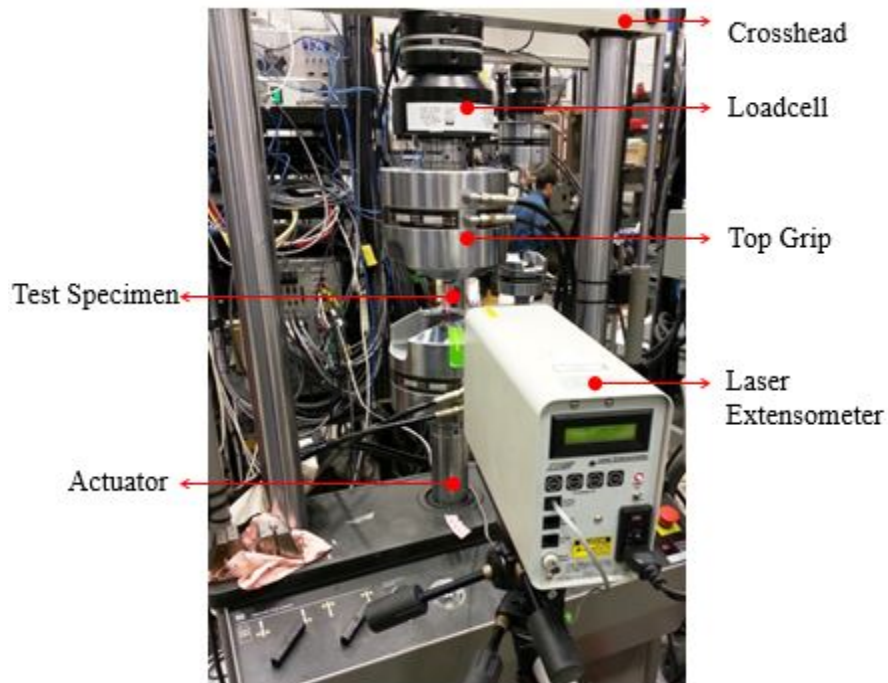


Figure 16. Material characterization test setup

2.2.3 Test Results

Test data for all five specimens were compared. As expected, SG data generated—post-yielding—were limited, as observed from stress-strain curves in figure 17. The stress-strain data with strain extracted from extensometer are shown in figure 18. These data were required to model the elasto-plastic behavior of the specimen for analysis.

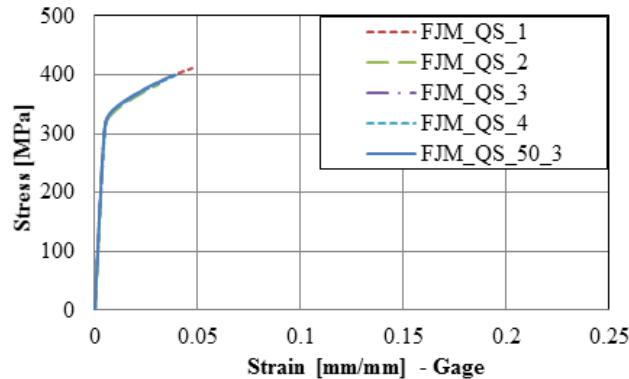


Figure 17. Stress vs. strain (from SG) for aluminum 2024-T3 clad at 0.05 inch/min

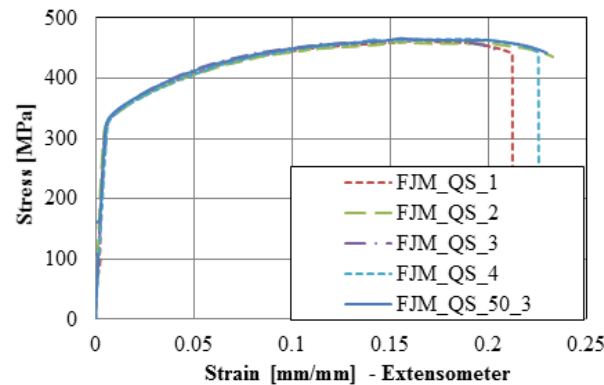


Figure 18. Stress vs. strain (from extensometer) for aluminum 2024-T3 clad at 0.05 inch/min

2.3 LT TESTS

Single-shear bolted lap joint tests were conducted to understand this joint's LT characteristics. A one-half dog bone setup was used as explained in section 1.1.1. Tensile load was introduced in the main part, and load was transferred to the transfer part and the bypass region of the main part until failure of the specimen.

2.3.1 Test Article

A detailed description of the test article is provided in section 1.1.1. To avoid bending of the specimen, an anti-buckling fixture (ABF) with a PTFE body was used (see figure 19).

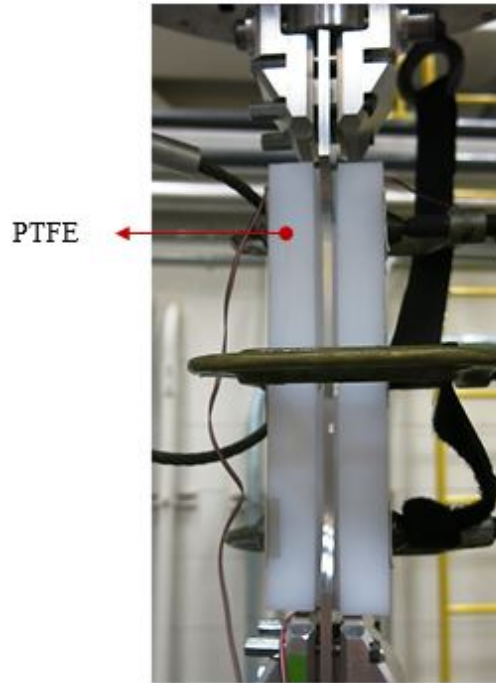


Figure 19. ABF for LT tests

2.3.2 Test Setup and Procedure

A high-speed servo hydraulic universal testing MTS machine [42] was used to conduct all the tests. Figure 20 shows the setup used for this test. Specifications of the high-speed MTS machine are detailed in section 2.3.2.1. A tensile load on the specimen was introduced by displacing the actuator. For testing at high speeds, it was important to ensure that the actuator had reached the desired speed at the onset of loading. To achieve this, a slack-inducer (SL) system designed and fabricated at Wichita State University (WSU)/National Institute for Aviation Research (NIAR) was used. Details of the system are shown in section 2.3.2.2. Three tests were performed for each stroke rate. The stroke rates were $8.3\text{E-}4$ in./s, 1 in./s, 20 in./s, 50 in./s, and 100 in./s. The stroke rate $8.3\text{E-}4$ in./s has been referred to as “quasi-static or QS” in this entire document.

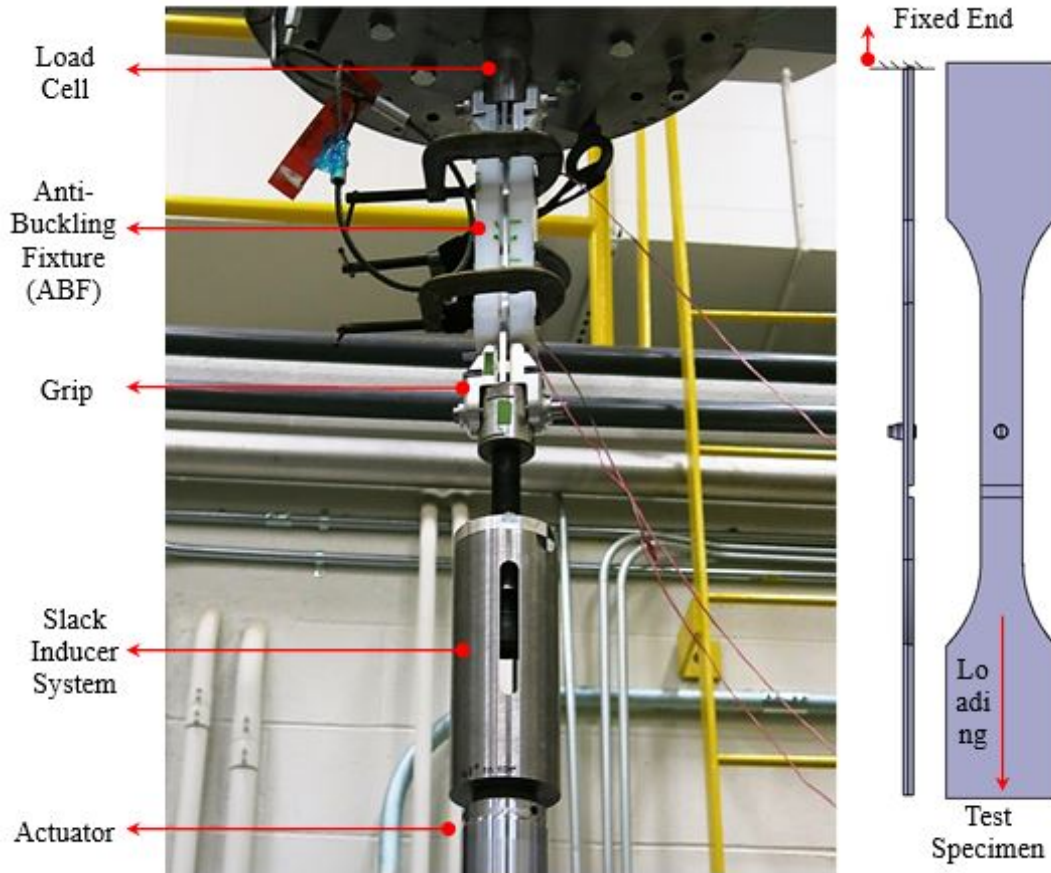


Figure 20. LT test setup

Prior to testing, each test article was prepared by following a specific procedure. First, three SGs were mounted on the aluminum specimen. Two gauges were mounted on the main part, one on the loading region and one on the by-pass region. The third SG was mounted on the transfer part. Details of the SG used and a schematic of the gauge placement are shown in section 2.3.2.3.

The HI-LOK fastener was installed next, and the torque at the hex shear-off was recorded. To install the HI-LOK fastener, the specimen was constrained on a fixture and the fastener was installed following the guidelines for HI-LOK installation [37]. Because the configuration of the LT test specimens involved an interference fit hole, equation 4—extracted by a linear fit of data in figure 13—was used to evaluate the clamping force. The torque and clamping force data for each specimen are presented in table 1. These data were used for setting up the DJMs.

The ABF was then mounted on the specimen, and the gauges were connected to the data-acquisition system. Finally, the specimen assembly was mounted on the MTS test machine, and the SL was adjusted based on the stroke rate. Displacement of the actuator, load recorded by the load cell, and strains from the three gauges were recorded by the data-acquisition system. The acquisition rate was 10 Hz, 130 kHz, 1.5 MHz, 5MHz, and 10 MHz, going from QS to 100 in./s stroke rate.

Table 1. Test matrix for LT tests and estimated clamping force

Test Stroke Rate (in/s)	Specimen #	Torque at Hex Breakoff (N·m)	Clamping force (N)
QS	FJM-QS-1	2.32	1951.8
	FJM-QS-2	2.79	2530.1
	FJM-QS-3	2.62	2321
	Average	2.6	2296
1	FJM-1-1	2.49	2161.0
	FJM-1-2	2.81	2554.7
	FJM-1-3	2.9	2665.5
	Average	2.73	2460.4
20	FJM-20-1	2.43	2087.2
	FJM-20-2	2.37	2013.4
	FJM-20-3	2.48	2148.7
	Average	2.43	2083.1
50	FJM-50-1	2.63	2333.3
	FJM-50-2	2.8	2542.4
	FJM-50-3	2.76	2493.2
	Average	2.73	2456.3
100	FJM-100-1	2.5	2173.3
	FJM-100-2	2.61	2308.7
	FJM-100-3	2.5	2173.3
	Average	2.54	2218.4

2.3.2.1 High-Speed Servo Hydraulic MTS Machine

The tension testing was conducted at NIAR using a high stroke rate MTS servo hydraulic testing machine, shown in figure 21. The testing machine is capable of maximum speeds up to 500 in./s. The testing machine can apply sustained loads up to 5000 lbf at maximum speed and up to 9000 lbf sustained when the speed is reduced to quasi-static range.



Figure 21. High-rate servo hydraulic MTS testing machine at NIAR

2.3.2.2 WSU/NIAR SL System [43]

The SL system was required for conducting tests at high stroke rates. To reach a desired stroke rate, a finite period of acceleration and a finite displacement are required. The amount of displacement is proportional to the stroke rate required. By using the SL system, the user can define a certain distance (or slack) to allow the actuator to reach the desired stroke rate prior to loading the specimen. The SL mechanism was designed and fabricated at WSU/NIAR and is shown in figure 22.



Figure 22. SL mechanism fabricated at WSU/NIAR

2.3.2.3 SG Installation

Three SGs were placed on each specimen. Two gauges were placed on the main part, on both sides of the bolt, and one gauge was placed on the transfer part. All the gauges were placed 1 inch away from the center of the hole. A schematic showing the SG positions is shown in figure 23. Vishay CEA-06-250UN-350/P2 SGs with a gauge factor of 2.105 and resistance of 350 Ohms were used for these tests.

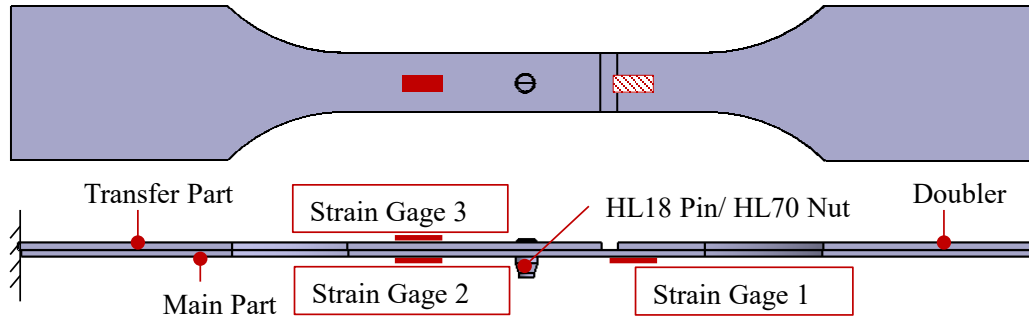


Figure 23. SG locations on LT specimen

2.3.3 LT Test Results

The %LT for all the tests conducted was calculated using equation 5, where SG 1 are strains from SG 1 and SG 2 are strains from SG 2. The SG locations are shown in figure 23. The strain data from each SG were compared against the remote stress, which was evaluated using forces from the load cell and cross sectional area of the main part. Figure 24 shows a comparison plot of strain data from all the tests conducted at different stroke rates. The data presented are plotted until failure was reached.

$$\% \text{Load Transfer} = \left(1 - \frac{\text{SG2}}{\text{SG1}} \right) \times 100\% \quad (5)$$

Based on the test results shown in figure 24, it can be concluded that the material exhibited elasto-plastic behavior in the loading region of the main part before failure. From the material characterization tests, the yield strain can be estimated to be 0.0047inch/inch, and the results from SG 1 show that the strains are well above the calculated material yield strain value. As a result, using equation 5, an increase in LT is expected beyond that point.

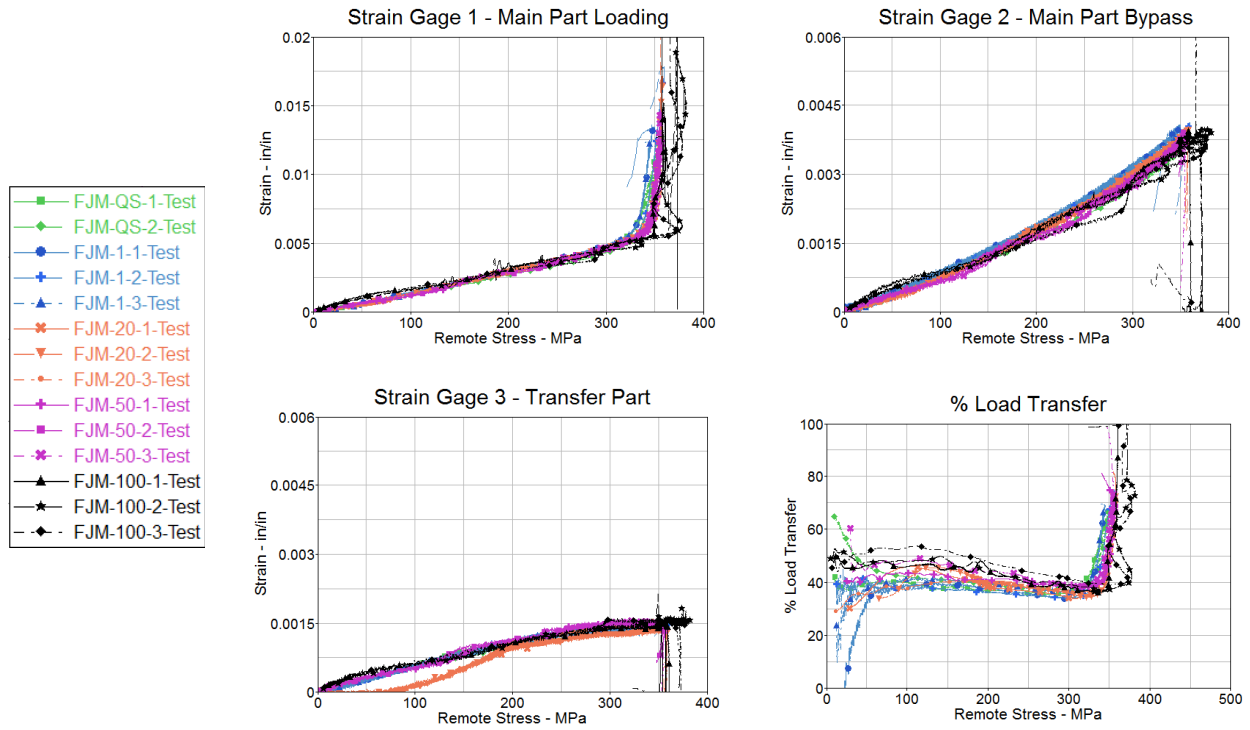


Figure 24. LT test results comparison for different stroke rates

A comparison of LT for all the tests is also shown in figure 24. For quasi-static and 1 inch/s stroke rates, the LT remains at an average value of 40%, which is consistent with the LT of a similar configuration reported in [14]. For stroke rates of 20 in./s and 50 in./s, a slight increase in the LT was observed. At 100 in./s, a significant increase of the average LT (50% vs. 40%) was observed up until remote stresses of 160 MPa. After that, it gradually decreased to 40%. Failure observed was a tear-out of the plate material at the net section for all the stroke rates. Figure 25 shows one example for each stroke rate. Plastic deformations were observed at the boundary of the hole, due to bearing loads. Necking and thinning were also observed on the main part at approximately the mid-plane of the hole or the net section. Necking and thinning of the material at the failure location were observed, and the associated failure plane was approximately 45 degrees, as expected.

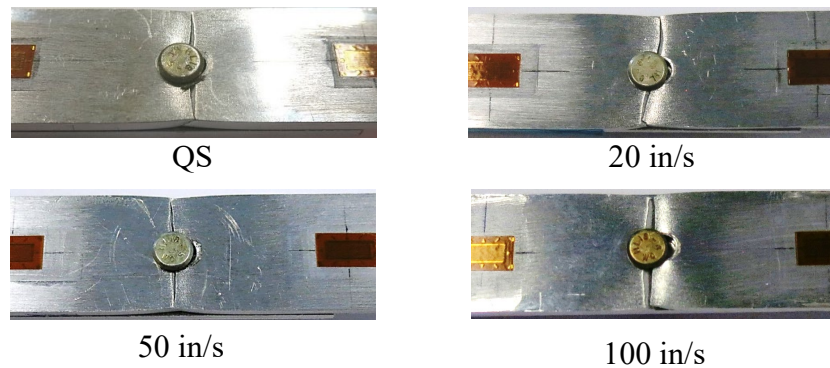


Figure 25. Failure on specimen for the LT test for QS stroke rate

3. FINITE ELEMENT MODELING

To evaluate the different simplified joint modeling approaches, first an DJM of the test article (see figure 1) was created and validated against test data. Then the validated FE model was used as a basis to compare different SJM techniques. The FE modeling practices used for this study are summarized in this chapter.

3.1 MESH DISCRETIZATION

To accurately capture the behavior of the subject test specimen, the ABF

used in the test was also modeled. For all the FE models generated, a 1-inch-long annular region (patch area) of elements around the fastener hole of the main and transfer parts was introduced into the separate subject components for extracting information such as energy and stresses, only in the vicinity of the hole. Table 2 summarizes the quality criteria used for the mesh. This was used for all the FE models for consistency and accuracy [26, 45].

Table 2. Mesh quality criteria

Parameter	Allowable	Parameter	Allowable
Jacobian	>0.7	Skew	<60
Warpage	<5.0	Min Angle	>45
Aspect Ratio	<10	Max Angle	<135

3.1.1 DJM

The DJM is shown in figure 26 and consists of the specimen assembly (main and transfer parts), the bolt, and the nut. The computational cost of simulation was disregarded for this model and, therefore, fine discretization, with a minimum element length of 0.206 mm, was applied to critical areas of the specimen geometry. These include the patch area around the hole on the main and transfer parts, as shown in figure 27, and the bolt and nut, as shown in figure 28. This mesh is considered “fine” because the minimum element length is usually limited to 3 mm to control time step in large models [45]. The threads of the bolt were not modeled for this study, and the nodes of the nut threads were shared with those of the bolt. The doubler and the ABF were meshed with larger elements, as shown in figure 29, because these are not parts of interest. As shown in figure 27, elements within the patch area around the fastener hole on the main part and transfer part were put into separate components to ease post-processing.

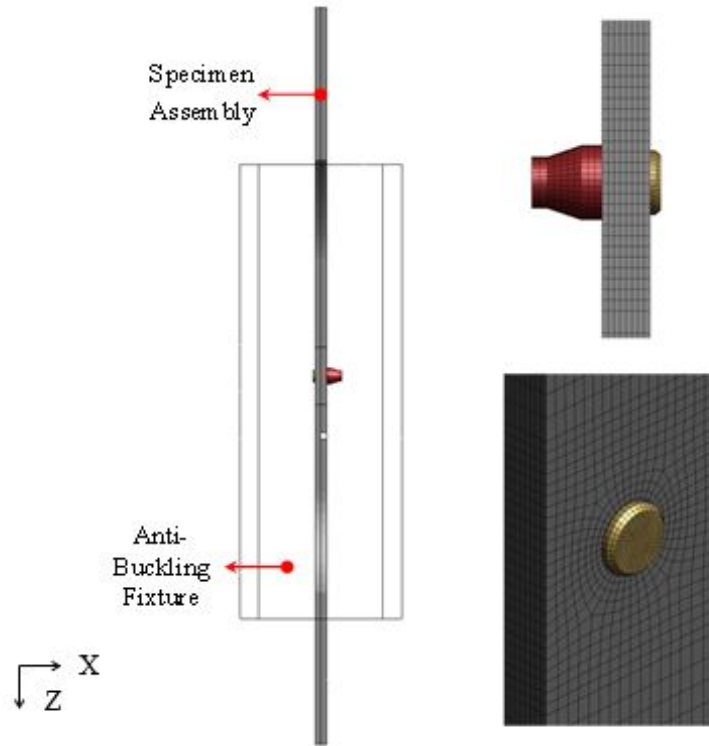


Figure 26. DJM setup

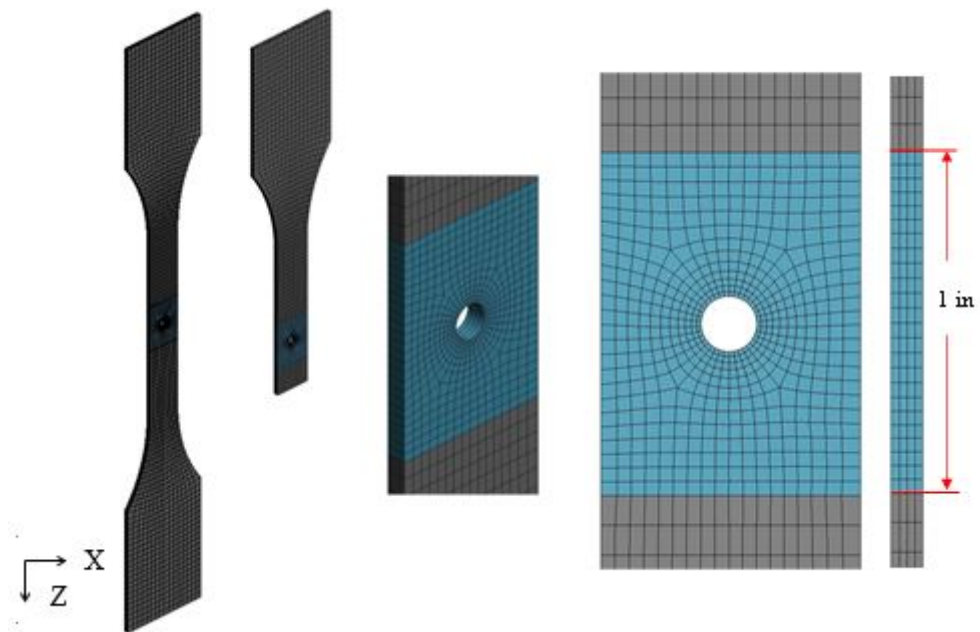


Figure 27. FE discretization of main part and transfer part of LT specimen

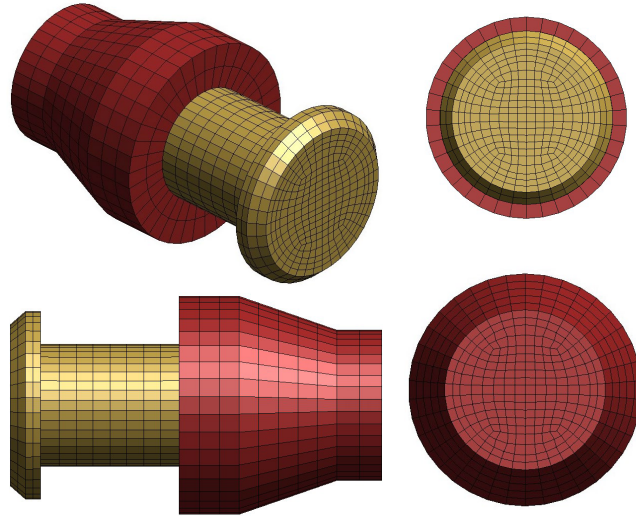


Figure 28. FE discretization of HI-LOK bolt and nut

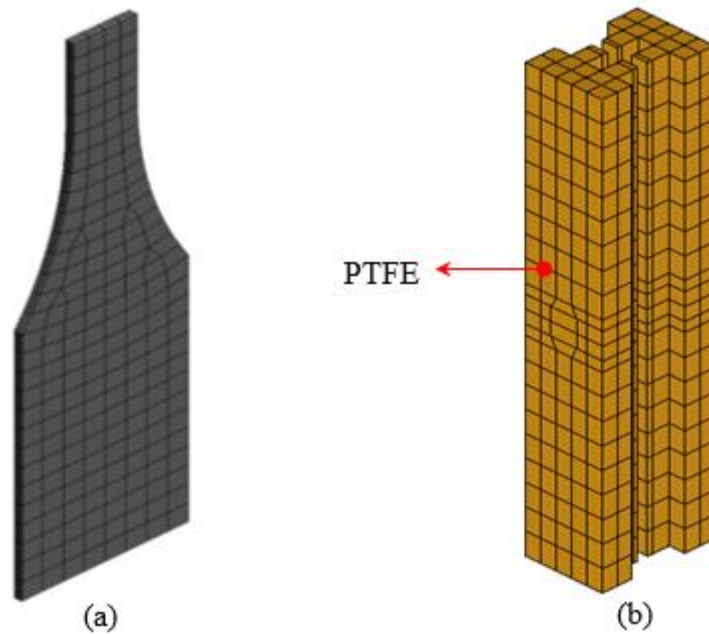


Figure 29. FE discretization of (a) doubler and (b) ABF

3.1.2 SJMs

The goal of this study was to evaluate SJMs for large-scale structural crashworthiness applications. By SJM, it is meant that the critical parts, as defined in the DJM, are not modeled in comparable detail. To accomplish this, the following SJMs were evaluated: 1) rigid body element (RBE) joint model with no hole (Configuration 1) and 2) mesh-independent spotweld beam model (Configuration 2). A variation of each of these methods was created for comparison. The variations were: 3) mesh-independent spotweld beam model connected to an elastic patch (EP) representing

a fastener hole model (Configuration 3) and 4) RBE joint model with no hole (Configuration 4). Configurations 3 and 4 were devised within NIAR to consider their applicability to large structures.

3.1.2.1 RBE SJM With Hole

In this technique, the bolt is idealized with a beam element, and the ends of the beam are connected to the boundary of the fastener hole using RBEs, as shown in figure 30. The plates clamped by the bolt are modeled with 2D shell elements, which are commonly used for discretizing parts in large FE models because of their computational efficiency.

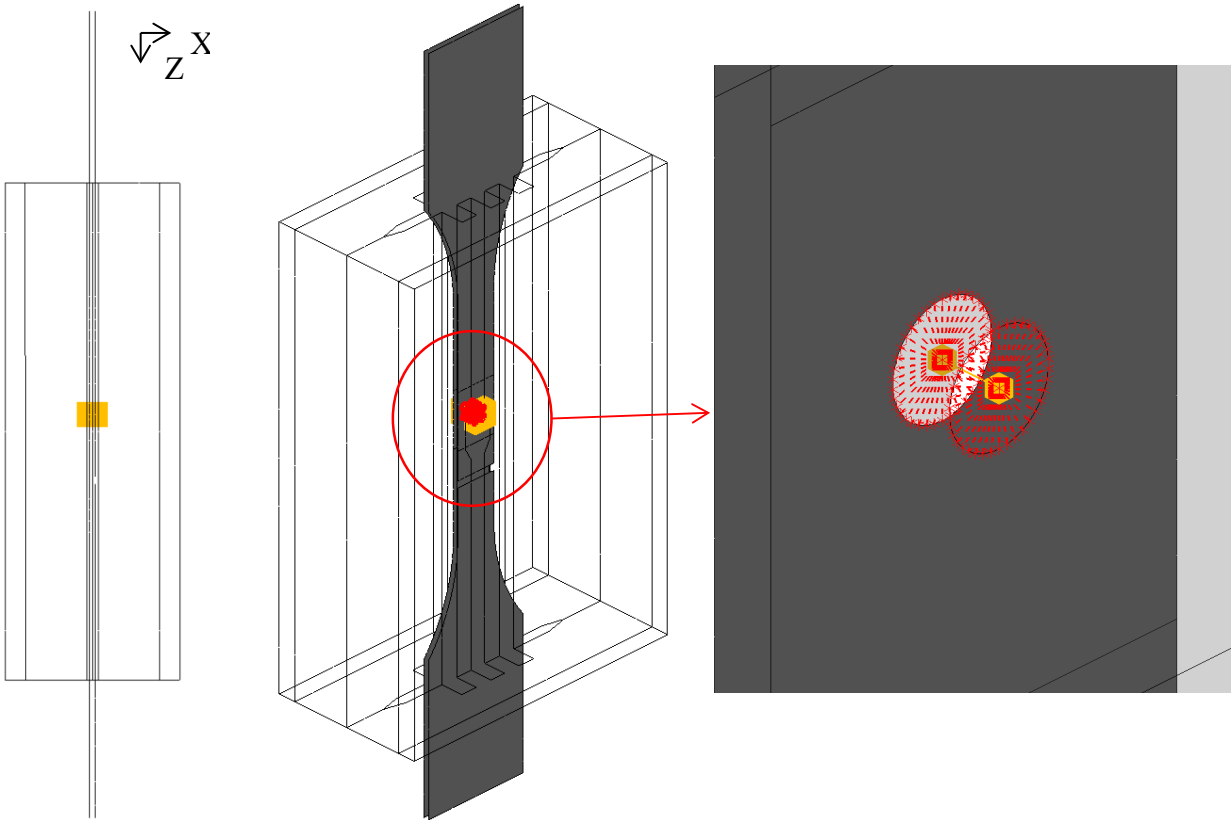


Figure 30. Model setup of RBE SJM

Because the RBE SJM uses RBEs, the boundary of the hole is essentially rigid. Possible variations for this joint model exist because of possible different mesh sizes. Three different RBE SJMs were generated, as shown in figure 31. Configuration 1 was a fine-mesh model with minimum element length of 0.331 mm. In this configuration, the number of elements on the edge of the hole was the same as the number of elements on the DJM. In Configuration 1A, a coarser mesh with minimum element length of 3 mm was used for the specimen. Four nodes were placed on the boundary of the hole, and a square hole was formed. In Configuration 1B, 6 nodes were maintained around the edge of the hole, and the minimum element length was 2 mm. Note that the main part and the transfer part both had the same setup.

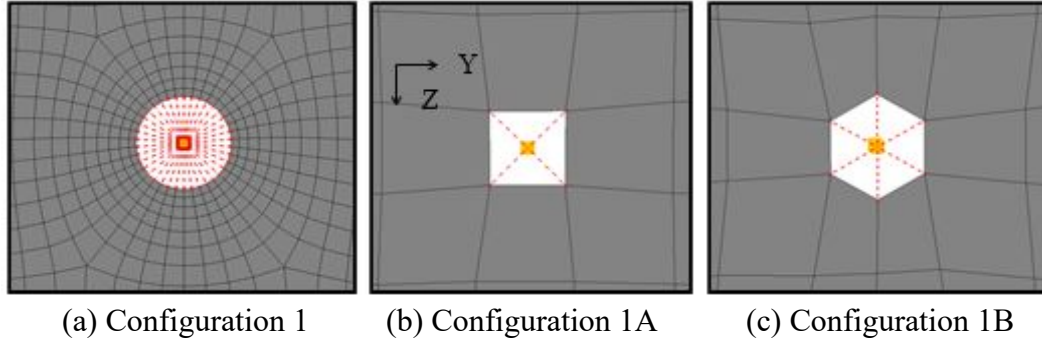


Figure 31. Variations of RBE SJMs

3.1.2.2 Mesh-Independent Spotweld Beam SJM

In this method the bolt shank is idealized using a beam element. The head and nut of the bolt are not modeled. The beam is connected to the parts using the tied contact formulation within LS-DYNA known as *CONTACT_SPOTWELD [46]. The setup of this FE model is shown in figure 32. The tied contact mechanism, *CONTACT_SPOTWELD, is explained in detail in section 3.4.1. When large models are meshed, it is a laborious process to align elements of adjoining parts to ensure that the beam is placed at an ideal location with respect to the contact surface. Therefore, for this study, several possible variations of the beam location with respect to the element were explored, as shown in figure 33.

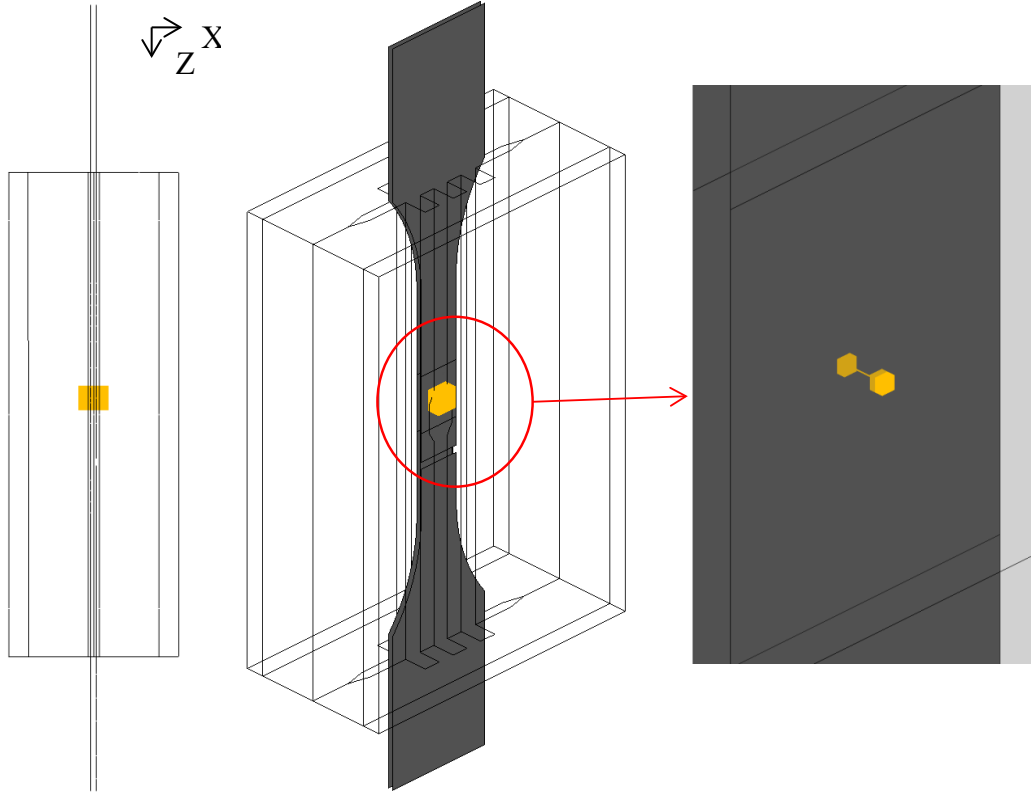


Figure 32. FE model setup of mesh-independent spotweld beam SJM

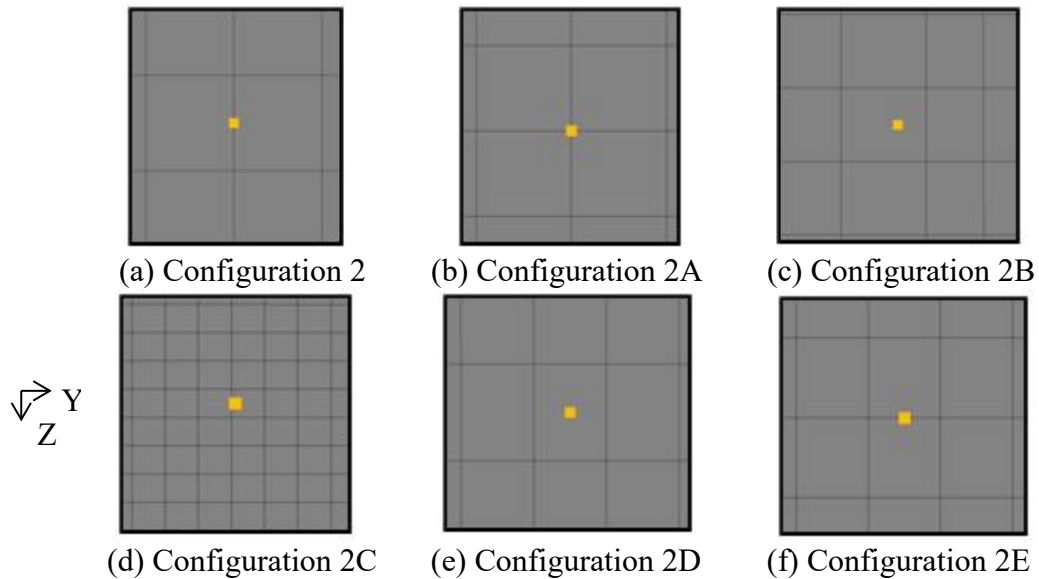


Figure 33. Variations of mesh-independent spotweld beam SJM—same mesh on main part and transfer part

As seen in figure 33, Configuration 2 was a fine-mesh model with the beam placed at an arbitrary location with respect to the element. The fine-mesh model had a minimum element length of 0.3 mm. For the remaining configurations, the minimum element length was 3 mm. Note that for

variations shown in figure 33, the main part and the transfer part both have the same mesh setup. Variations shown in figure 33 rarely occur in large models because parts are meshed independently. Taking this into consideration, five additional configurations were studied in which the main part and the transfer part do not have the same mesh (see figure 34).

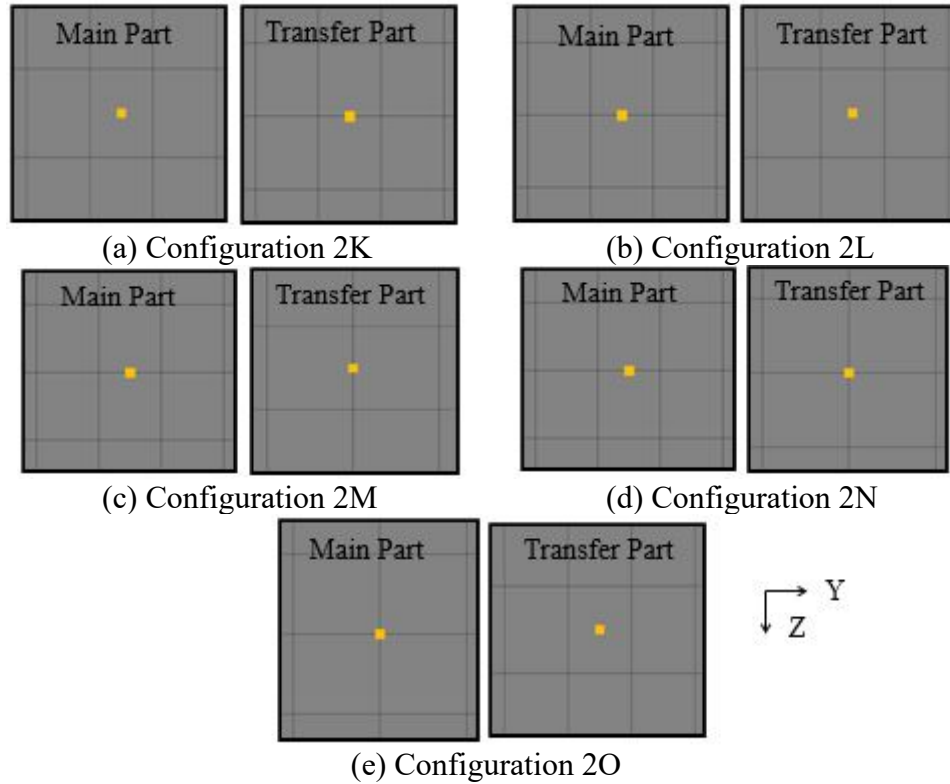


Figure 34. Variations of mesh-independent spotweld beam SJM—different mesh on main part and transfer part

3.1.2.3 Mesh-Independent Spotweld Beam SJM With EP

This method is an extension to Configuration 2. The difference in this method is that the elements to which the bolt connects are modeled using an elastic material model to simulate the presence of a fastener hole. This is accomplished by controlling the Young's modulus of the elastic elements in which stress concentrations develop in the surrounding elements, which are representative of the scenario experienced when a fastener hole is present. In this model, the group of elements with elastic material properties is referred to as an EP. Figure 35 shows the setup for this SJM technique, in which the red elements represent the EP. The EP is modeled as steel, which is the same material for the bolt head and nut. A stiff material will facilitate LT and will not store large amounts of energy.

Some variations of this model were generated, as shown in figure 36. Configuration 3 was a fine-mesh model with the same mesh as the DJM, except that the hole is filled. In Configurations 3A and 3B, a coarse mesh with a minimum element length of 3 mm was used. In Configuration 3A, the EP was maintained only on the main part, which is likely to fail, whereas in Configuration 3B, both the main part and the LT had an EP.

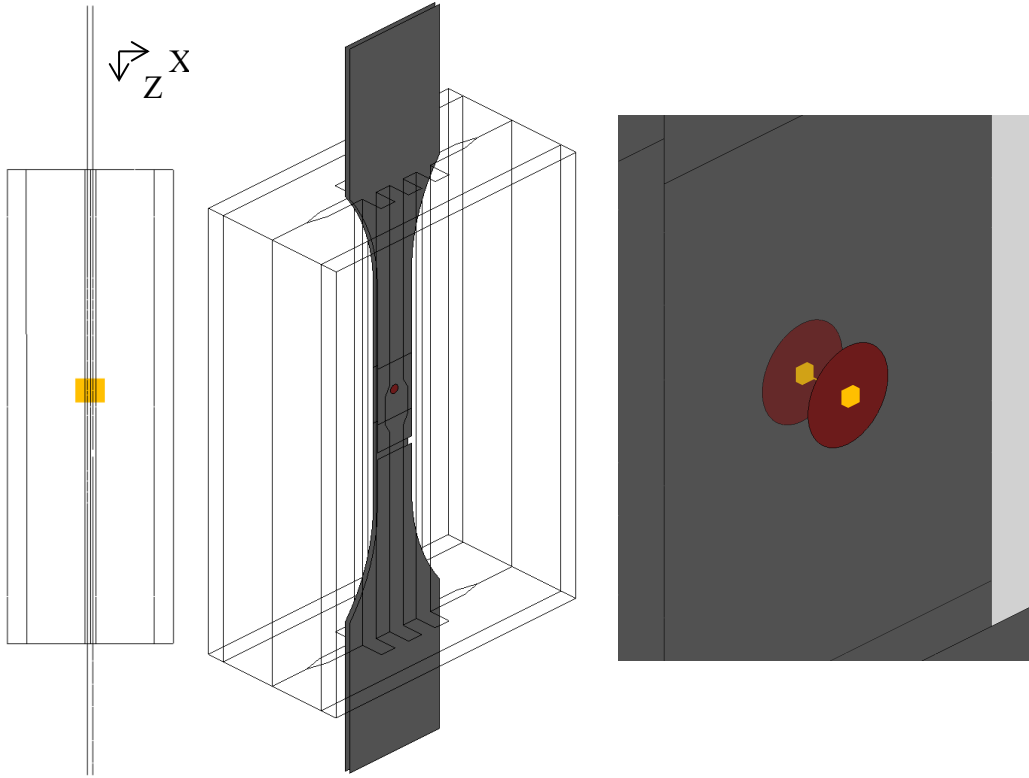


Figure 35. FE model setup of mesh-independent spotweld beam model with EP

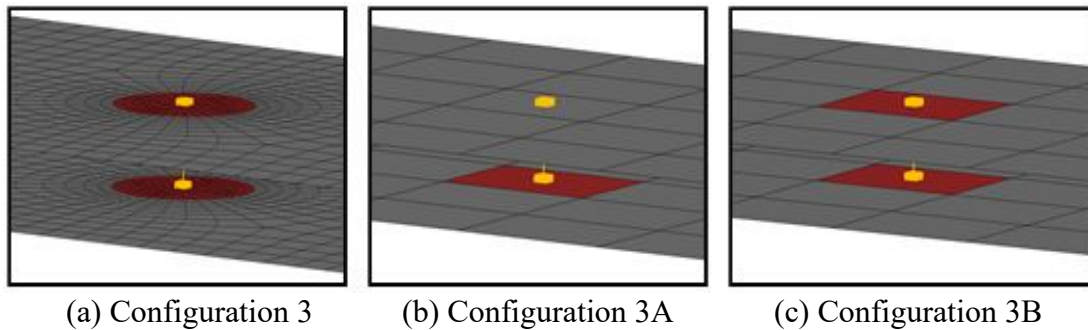


Figure 36. Variations of mesh-independent spotweld beam SJM with EP model

3.1.2.4 RBE SJM With No Hole

This simplified technique is an extension to the RBE SJM technique. As shown in figure 37, this technique uses the same setup as the RBE SJM, except the hole on the main part and the transfer part is not modeled. The nodes of the nodal rigid body are connected to the main part and transfer part using the tied contact option. This method allows the nodal rigid bodies to be connected to the parts at any location desired. Note that the beam that represents the bolt shank is not connected to any of the parts. The beam is connected only to the nodal rigid body.

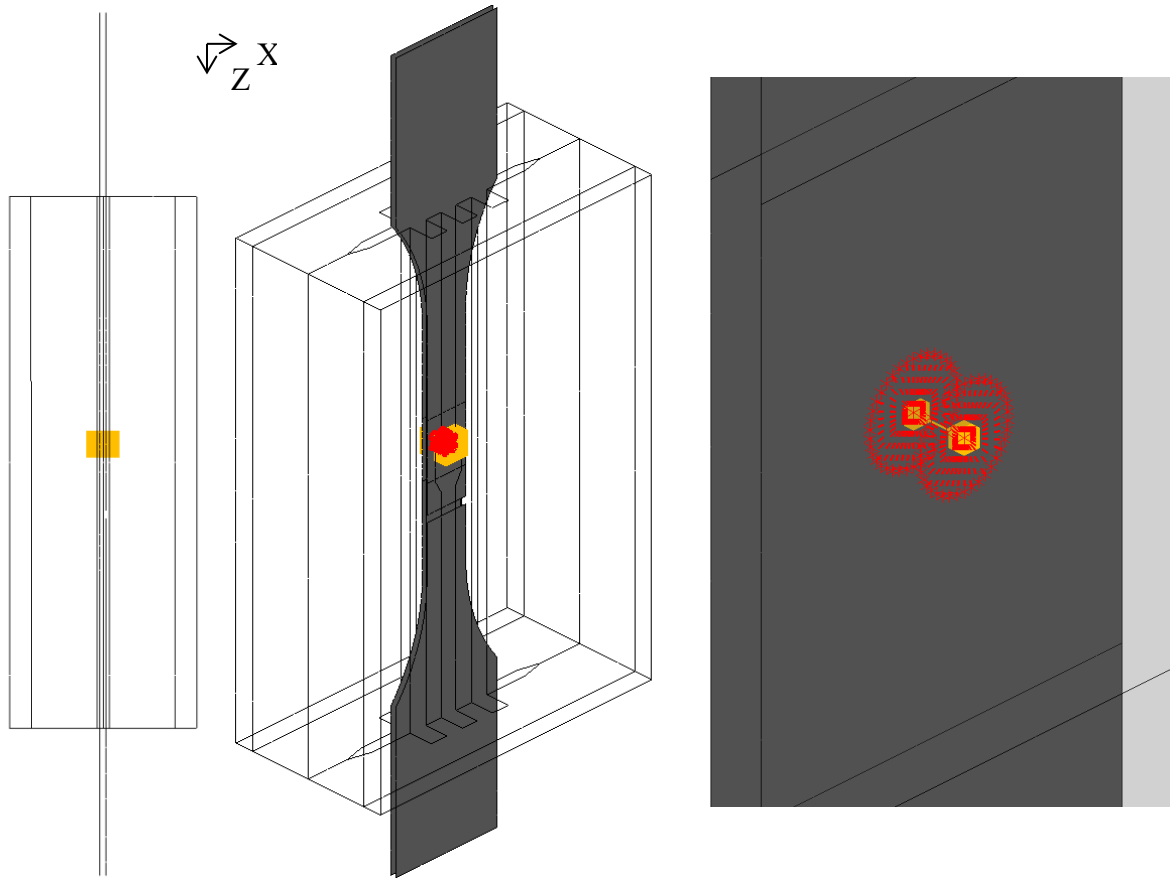


Figure 37. FE model setup of RBE SJM with no hole

The number of nodes in a nodal rigid body and the nodes' locations can be controlled. This results in several variations in this SJM method. The variations studied are shown in figure 38. Configuration 4 was a fine-mesh model with a minimum element length of 0.3 mm and approximately 38 nodes to represent the nodal rigid body. These were the same number of nodes around the hole of the DJM. From Configuration 4A to 4D, four nodes were used to represent the nodal rigid body, and the nodes were rotated by 15 degrees for each configuration. In Configuration 4E, the nodal rigid body consisted of eight nodes. While maintaining the same nodal rigid body, the mesh was changed in Configurations 4F to 4H. A coarser mesh with a minimum element length of 3 mm was used for the main and transfer part in Configurations 4A to 4H. Note that the size of the nodal rigid bodies represented the diameter of the fastener hole.

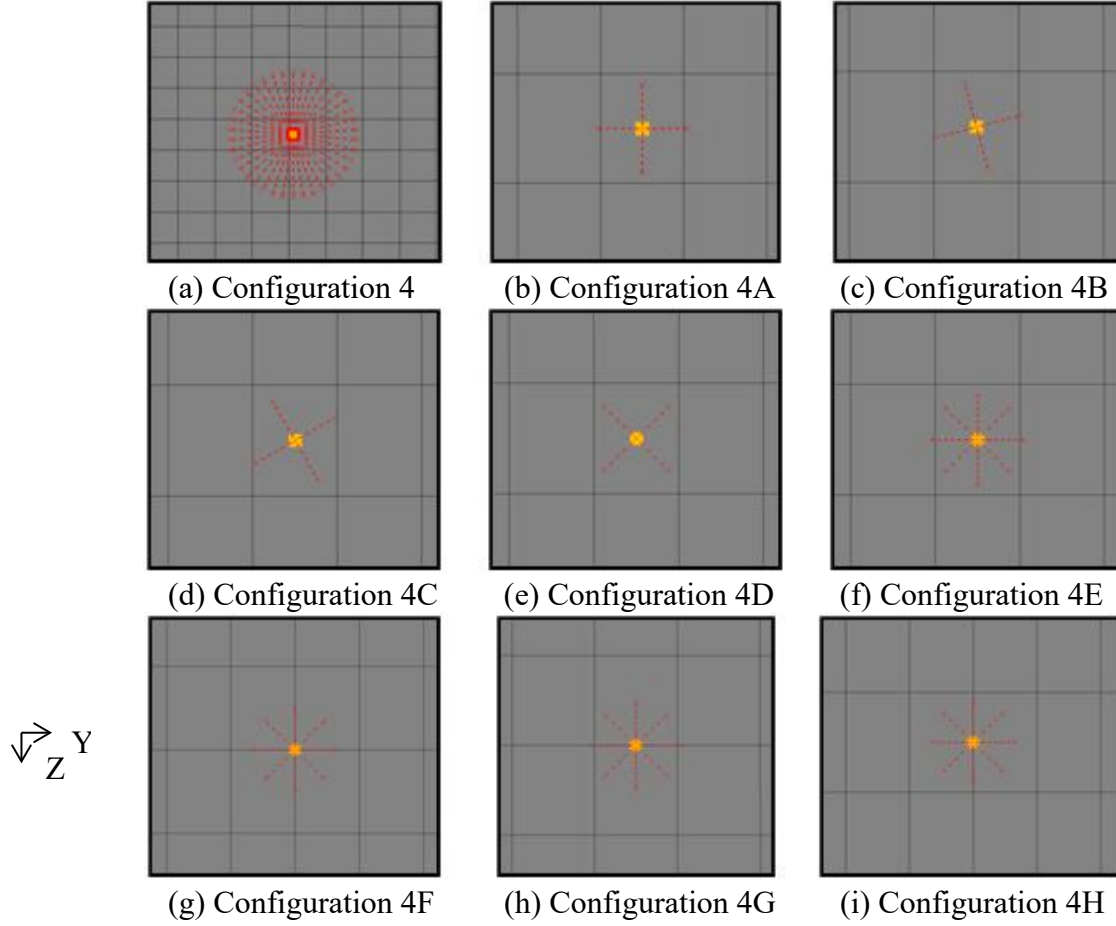


Figure 38. Variations of RBE SJM with no hole

3.2 ELEMENT DEFINITIONS

The size of the coupons in this study enables users to have a very fine discretization for accurate results. However, because the end goal is studying joints for crashworthiness of large structures, all SJMs were meshed with element sizes of ≥ 3 mm. A smaller mesh size was incorporated in some SJMs for comparison purposes. The DJM was discretized with very small size elements of < 1 mm because a very accurate detailed model was required to compare to the test and to use as a baseline.

The DJM was discretized using 3D solid hexahedron and tetrahedron elements. The ABF was also discretized using 3D solid elements. The constant stress solid element formulation in LS-DYNA was used for all the models.

For the SJMs, the aluminum dog bone coupons were meshed with 2D quad and tria shell elements. The Belytschko-Lin-Tsay 2D shell element in LS-DYNA was used because of its efficiency and extensive use in large structural crashworthiness simulations [45]. The bolt shank was idealized using the spotweld beam element available in LS-DYNA. This element allowed for efficient application of bolt preload. This beam element formulation has been used to model bolts for many studies involving large structural models [12, 47].

3.3 BOUNDARY CONDITIONS AND CONSTRAINTS

A fixed boundary condition was applied to the upper tabs of the specimen in the FE model to represent the LT tests. Similarly, the displacement boundary was applied to the nodes of the lower area of the specimen tabs. The test equipment—the grips, SL system, and the MTS machine—were not modeled. As a result, the effect of test machine compliance was not captured by the FE models. Boundary conditions applied to the FE models are shown in figure 39. Note that all the boundary conditions were applied in a global coordinate system.

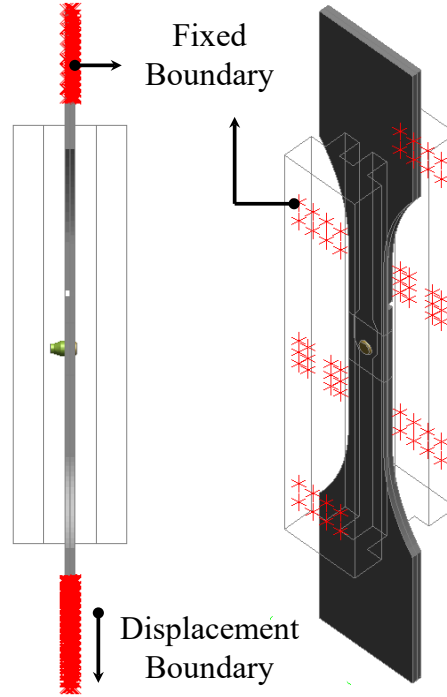


Figure 39. FE model boundary conditions for LT specimen

3.4 CONTACT MODELING

LS-DYNA provides several methods for contact modeling with automatic or manual options. With automatic options, nodes are checked for contact in both + and - directions of the normal vector; whereas, in manual options, the check is only performed in the + direction of the normal [48]. There are several options that can be modified within the contact cards. The default options were used for this study except for the friction parameters.

Friction parameters are also defined in the contact card. A static and dynamic coefficient of 0.1 was used for this study. A parametric study was conducted to study the friction parameters. The parameters available to define friction in the contacts selections are *FS*, the static coefficient of friction; *FD*, the dynamic coefficient of friction; *DC*, the decay constant; and *VC*, the coefficient of viscous friction [46]. The coefficient of friction (μ_c) is evaluated using *FS*, *FD*, *DC*, and the relative velocity of surfaces in contact (V_{rel}) as shown in equation 6 [46]:

$$\mu_c = FD + (FS - FD)e^{-DC|V_{rel}|} \quad (6)$$

For this study, the values of FS , FD , or DC were not quantified by any experiments and, therefore, remained unknown. Therefore, for all the simulations, FS was set equal to FD , and DC was set to zero. A study with different values of FS or FD was conducted to understand the effect of friction, and a value of 0.1 was used for FS and FD .

For both the DJM and SJMs, the `*AUTOMATIC_SINGLE_SURFACE` [46] and the `*AUTOMATIC_SURFACE_TO_SURFACE` [46] LS-DYNA options were used for modeling contact between the specimen and the ABF.

A tied contact, `*CONTACT_SPOTWELD`, was also used to connect the beam element to the shell elements in the simplified techniques described in sections 3.1.2.2 and 3.1.2.3. `*CONTACT_TIED_NODES_TO_SURFACE_OFFSET` was used for connecting nodes of the nodal rigid body to the shell elements for the simplified technique described in section 3.1.2.4

3.4.1 LS-DYNA Contact Option: `*CONTACT_SPOTWELD`

It is crucial to understand the tied contact, `*CONTACT_SPOTWELD`, because it is the primary entity forming the joint on some of the simplified joint methods. The description of this contact shown below is summarized from [49] and [50].

This contact is a constraint-based contact, which means no sliding is allowed between adjacent components. It enables coupling of both translational and rotational degrees of freedom. The components in contact are defined as slave, which are the nodes of the beam, and master, which are the segments of the shell elements. The components of this contact are shown in figure 40.

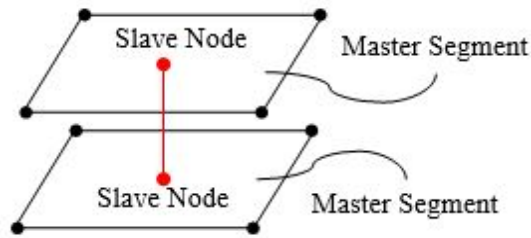


Figure 40. Components of `*CONTACT_SPOTWELD` [49]

On initialization, the contact point is established by search for the closest master segment to the slave node. When the contact point is established, constraints are developed based on shape functions, as shown in figure 41.

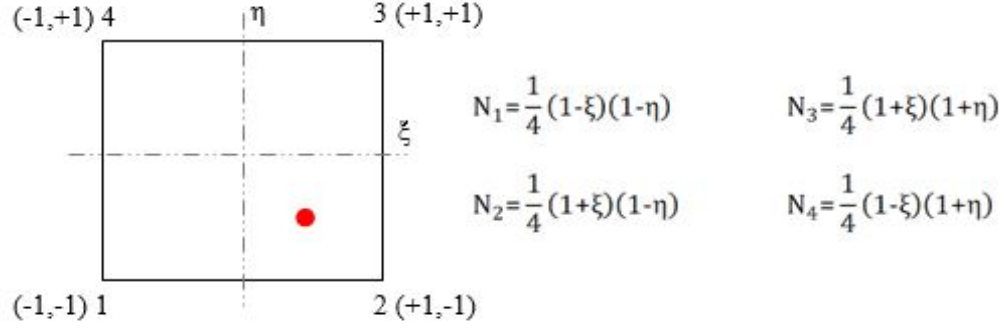


Figure 41. Shape functions for *CONTACT_SPOTWELD [49]

Therefore, the incremental master segment nodal force Δf_m^i and mass Δm_m^i are calculated using the shape functions, as shown by equations 7 and 8, respectively [50]. The forces on the slave node f_s are computed as the weighted average of the master segment nodes, as shown in equation 9. For instance, if the contact point is at the center of the element shown in figure 41, all four nodes will get 25% of the slave nodal force and mass.

$$\Delta f_m^i = \sum_{i=1}^4 N_i(\xi, \eta) * f_s \quad (7)$$

$$\Delta m_m^i = \sum_{i=1}^4 N_i(\xi, \eta) * m_s \quad (8)$$

$$f_s = \sum_{i=1}^4 N(\xi, \eta) * f_i^j \quad (9)$$

As a result, this contact is highly affected by the location of the contact point on the master segment. It is noted in the LS-DYNA keyword manual that element failure forces change with respect to the contact point location, and scaling factors and options for failure force are also available in the manual [46].

3.4.2 LS-DYNA Contact Option: *CONTACT_TIED_NODES_TO_SURFACE_OFFSET

This contact is similar to *CONTACT_SPOTWELD except that it couples only translational degrees of freedom. The offset option was used because it is required for contact between rigid body and deformable bodies.

3.5 PRELOAD APPLICATION

3.5.1 Preload in Solid Bolt Model

Six different preload application methods can be used for a solid bolt model as presented by Nakalswamy [51]. The LS-DYNA programming option *INITIAL_STRESS_SECTION was used in this study. A pseudo-simulation, called the dynamic relaxation phase, was used for preload application. When convergence was achieved, the model with the final preloaded state was used as the initial input point for the transient simulation [46].

This preload application method requires the input of initial stress. The stress was evaluated using the clamping force of 2300 N and the cross-sectional area of the bolt of diameter 4.1275 mm. As a result, the equivalent stress required for preload was evaluated to be approximately 172 MPa. The result of preload application is shown in figure 42.

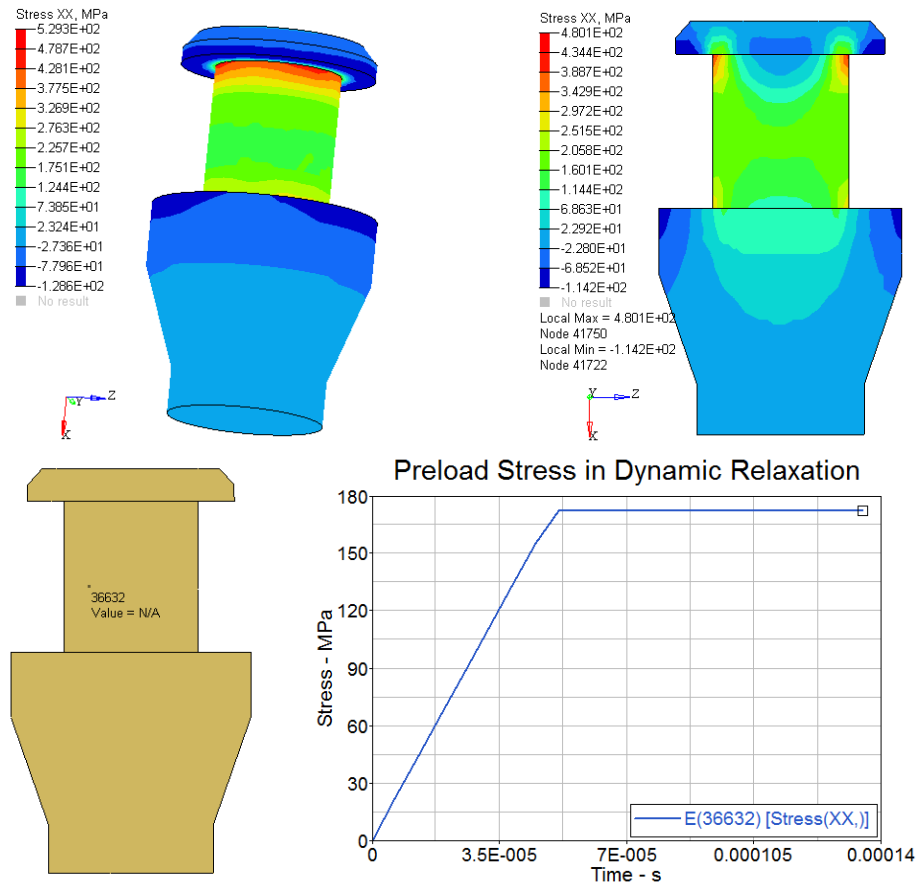


Figure 42. Preload on solid bolt model

3.5.2 Preload in Beam Bolt Model

For the SJMs, a beam element was used for modeling the bolt. To introduce a preload to the beams, the LS-DYNA programming option *INITIAL_AXIAL_FORCE_BEAM was used. Similar to the preload application in the solid bolt model, the dynamic relaxation phase was used to achieve the

desired force. When convergence occurred, the actual tensile load was applied. Figure 43 shows that the desired preload of approximately 2300 N was attained by this method.

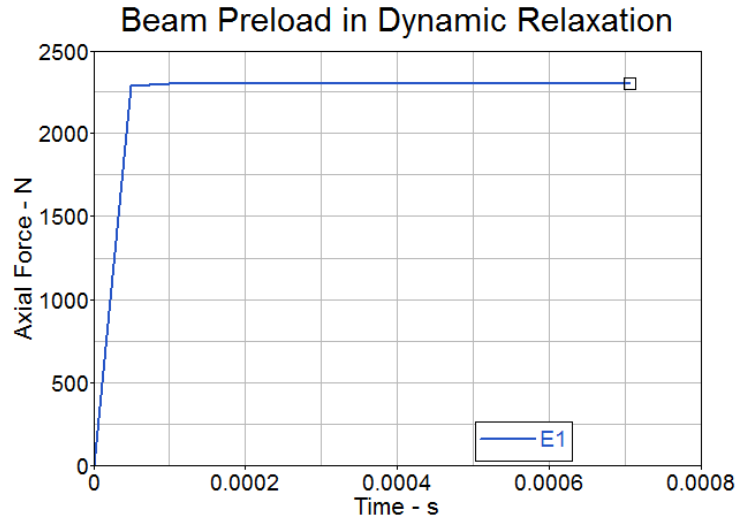


Figure 43. Preload on beam bolt model

3.6 MATERIAL MODELING

Clad aluminum 2024-T3 was the material used to manufacture the main part, the transfer part, and the doubler. The bolt consisted of a steel pin and aluminum nut, and the ABF was made of PTFE material. Note that because the bolt consisted of a steel pin, which is much stiffer than the aluminum parts it joins, failure was expected to occur on the aluminum parts. Therefore, an elasto-plastic material definition complete with the stress-strain profile was necessary for the main and transfer parts to study plasticity effects and model failure. For the other parts, because failure or plastic strains were not expected, an elastic material model was sufficient for capturing the material stiffness. To ensure FE models accurately represented the tests, material characterization tests were conducted as documented in section 2.2 to extract the material properties for aluminum 2024-T3. Generic properties were used for other materials [51]. The mechanical properties, with the respective LS-DYNA material cards used for different parts of the specimen assembly, are listed in table 3.

Table 3. Mechanical properties of materials used in FE model

Part	LS-DYNA Material Card	Density tonne/mm ³	Youngs Modulus (MPa)	Poisson's Ratio	Yield Strength (MPa)	Failure Strain	Reference
Main Part	*MAT_024	2.768e-9	69806	0.33	330.38	0.199	Sec 2.2
Transfer Part							
Doubler							
Bolt Pin (solid)	*MAT_001	2.768e-8	199948	0.27	-	-	MMPDS [52]
Bolt Pin (beam)	*MAT_100	2.768e-8	199948	0.27	-	-	MMPDS [52]
Bolt Nut (solid)	*MAT_001	2.768e-9	72395	0.33	-	-	MMPDS [52]
ABF AL	*MAT_001	2.768e-9	72395	0.33	-	-	MMPDS [52]
ABF PTFE	*MAT_001	2.16e-9	7239.5	0.33*	-	-	Teflon [53]

**Assumed*

The elasto-plastic material properties were defined using the LS-DYNA material card *MAT_024 [54]. This material card is a piecewise linear plasticity elasto-plastic material model with an arbitrary stress versus strain curve in which arbitrary strain-rate dependency can be defined [54]. Failure in the material model was defined based on plastic strains. A study performed at NIAR [43] has shown that this material model provides good performance and correlation to test data.

With the mechanical properties listed in table 3, the stress strain profile extracted from the material testing shown in section 2.2 was used to define the behavior of the material after yielding occurs. This material card requires the stress versus strain curve to be input in the form of effective stress versus effective plastic strain. Equations shown in [43] were used to convert the test data. Figure 44 shows the effective stress versus effective plastic strain curve.

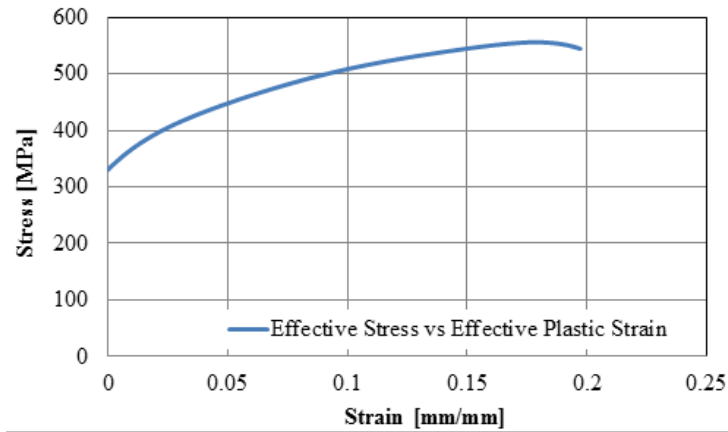


Figure 44. Effective stress vs. effective plastic strain for aluminum 2024-T3 at quasi-static rate

3.6.1 Material Strain-Rate Dependency

A part of this study involves exploring the effect of high strain rates on the LT characteristics of both the DJM and the SJMs. To perform this study via FEM, strain-rate sensitive material data are required. The LS-DYNA *MAT_024 material model allows the user to define a table with different stress versus strain curves, one per strain rate [54].

In a round-robin exercise performed by NIAR [55], bare aluminum 2024-T3 was tested at different strain rates. The data from bare aluminum were used to scale the clad aluminum 2024-T3 test data, documented in section 2.2 to obtain a representative stress versus strain curve for a strain rate of 187.5/s. As specified in the standard ASTM B209-10 [56], the difference between clad aluminum and bare aluminum is that the clad aluminum consists of a very thin layer (approx. 0.2% thickness) of pure aluminum on the surfaces. The strain-rate-dependent material data used for this study are shown in figure 45.

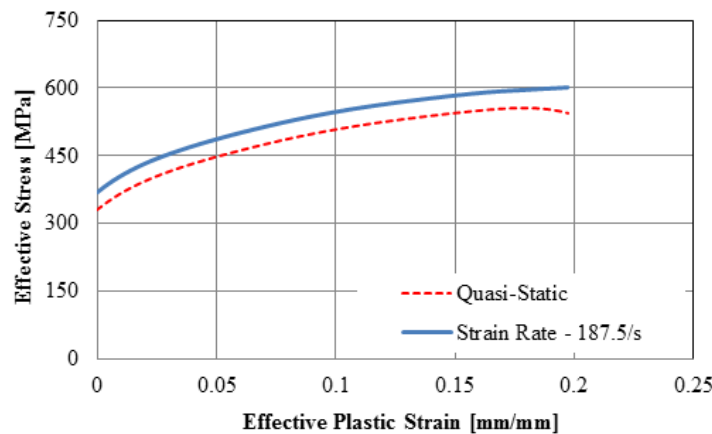


Figure 45. Clad aluminum 2024-T3 material data for quasi-static and strain rate 187.5/s

4. FEM RESULTS

FEM results are split into two sections according to the stroke rates: quasi-static and high speed. For both rates, the DJM was compared against the test data. For quasi-static, all four simplified joint methods were compared against the DJM. For high speed, only one of the simplified joint techniques was compared to the DJM.

4.1 CALCULATIONS

For presenting the FE simulation results, some of the parameters were calculated as explained in subsequent sections.

4.1.1 LT for Simulations

The LT calculation for the simulations differs from the test. In the test, SGs were used only on the top surface, and therefore the effect of secondary bending on LT was not captured. Secondary bending is explained in section 1.2.4.4. Therefore, to account for secondary bending, the LT for all the simulations was evaluated using cross sectional forces. This was required especially for shell elements in which the strain level for the top surface was difficult to extract. The cross sections (CSs) were located at the same locations as the SGs, as shown in figure 46. Equation 10 is used to evaluate the LT. CS 1 is CS 1 and CS 2 is CS 2. CS 1 is the CS plane that measures the load on the transfer part, as shown in figure 46. CS 2 is the CS plane that measures the load on the main part, as shown in figure 46. CS 3 is the CS plane that measures the load on the bypass part.

$$\% \text{ Load Transfer} = \left(\frac{Z \text{ Force on CS 1}}{Z \text{ Force on CS 2}} \right) \times 100\% \quad (10)$$

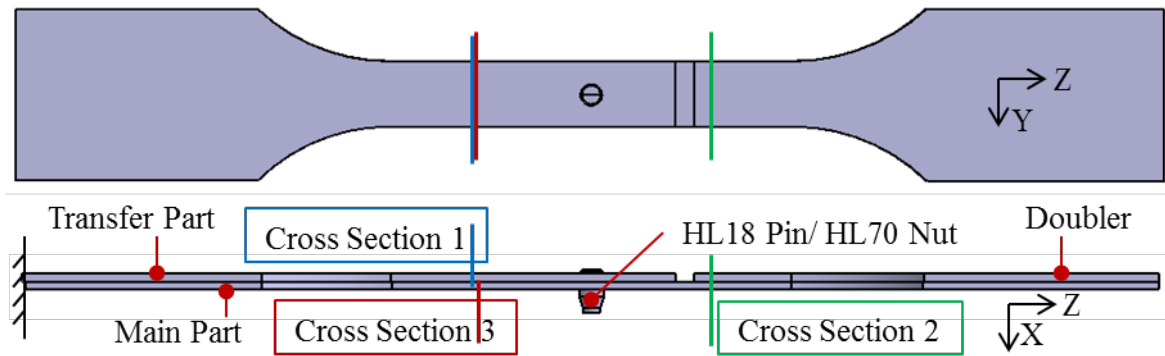


Figure 46. CS plane locations on LT specimen for simulations

4.1.2 LT by Bolt and by Friction

The LT by bolt and by friction was also evaluated. To accomplish this, a CS plane (CS 4) was placed through the center of the bolt shank for both the DJM and the SJMs, as shown in figure 47. The LT by bolt was then evaluated using equation 11. The remainder of the load was transferred by friction.

$$\% \text{ Load Transfer by Bolt} = \left(\frac{Z \text{ Force on CS 4}}{Z \text{ Force on CS 1}} \right) \times 100\% \quad (11)$$

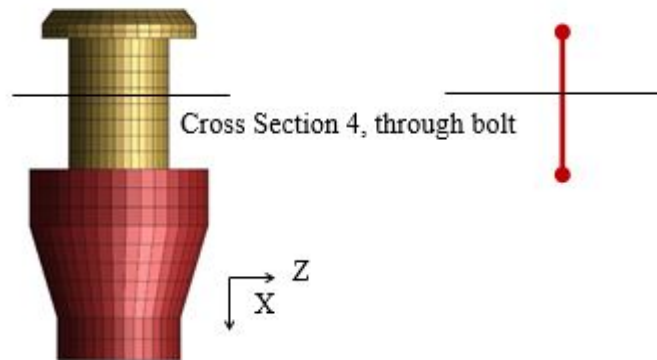


Figure 47. CS plane location on bolt for simulations

4.2 QUASI-STATIC

For quasi-static rates, the DJM was compared to the test results. The SJMs were then compared to the results from the DJM.

4.2.1 DJM

There were two main reasons for creating an DJM for this study: first to evaluate the FE modeling methods and second to extract data that cannot be collected from the test (such as energies, stress distribution, CS forces and stress concentrations). The additional data were used to evaluate the SJM techniques.

4.2.1.1 LT Comparison

Figure 48 shows the comparison of simulation results to test data. Results from simulation were obtained in the same manner as from the test (i.e., the average strains were used for evaluating the LT using equation 5). Strains were averaged from elements over the area and location of the SGs shown in figure 24.

The comparison presented in figure 48 shows that the strains at the three SG locations and the LT from the DJM correlate well to the test data. Discrepancies in LT results are observed between experiment and analysis at very low remote stresses. Remote stress is defined as the state of stress away from the joint. In this study, it is the stress at SG 1 location. These differences could be attributed to factors like friction because most of the load is transferred by friction before the bolt engages. Furthermore, the test specimens have small imperfections from manufacturing and specimen handling that were not accounted for in the simulation. These numerical analyses also required simplifying assumptions because of FE software limitations and time/cost constraints. For example, the test machine was not modeled.

An overall good level of correlation was observed between experimental and FE analysis results. Comparison of the simulation results to the test data validates the FE modeling methods; therefore, the DJM can be used to compare and evaluate the SJM techniques.

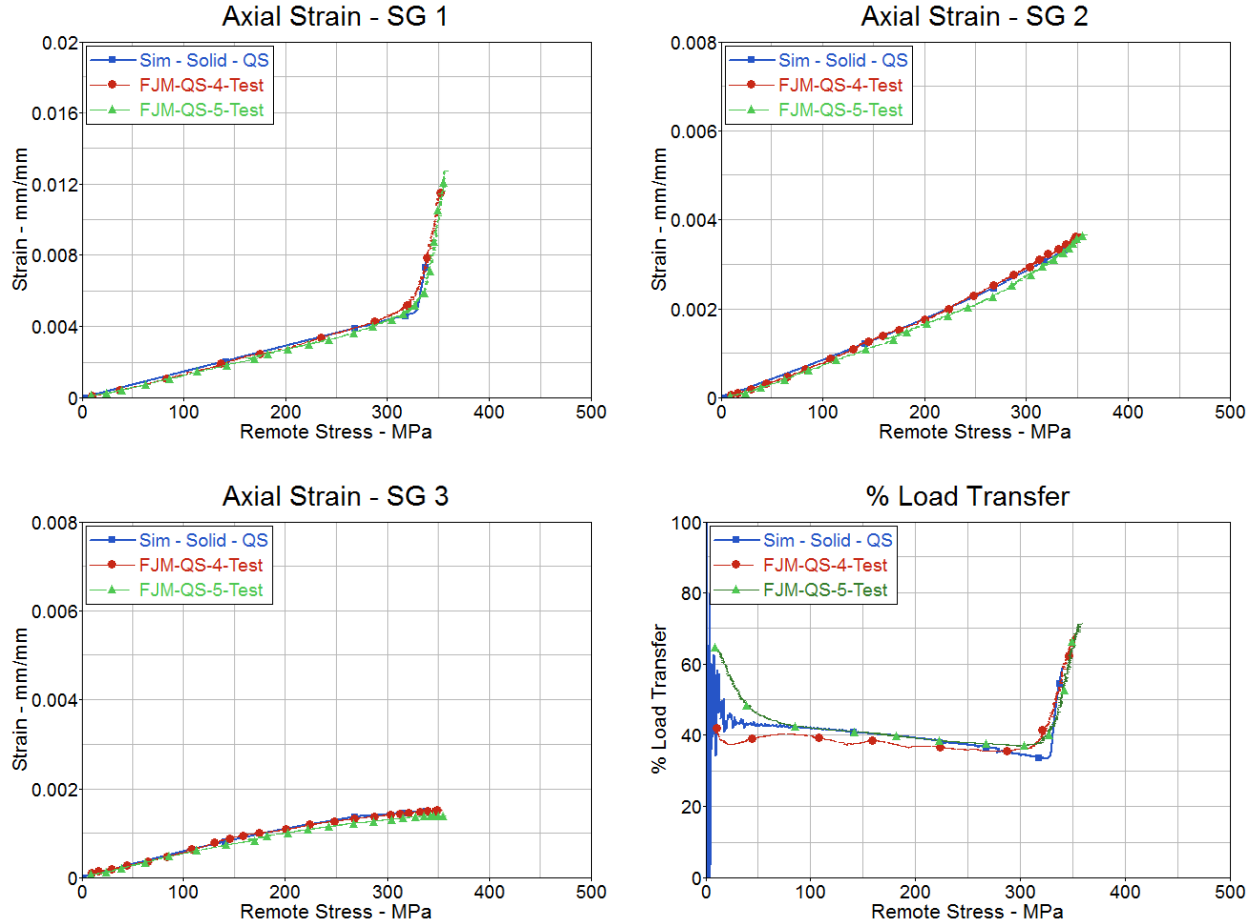


Figure 48. Comparison of DJM results to experiment results

4.2.1.2 Stress Distribution

Figure 49 shows the stresses developed on the plates from the application of bolt preload. High compressive stresses, in the magnitude of 30 to 160 MPa, occur in a localized area beneath the head and the nut. As a result, friction forces are higher in that region.

The state of stress at the initiation of failure on the main part is shown in figure 50. As expected, stress concentrations are observed at the region around the hole, and failure initiates along the center line of the hole perpendicular to the direction of loading.

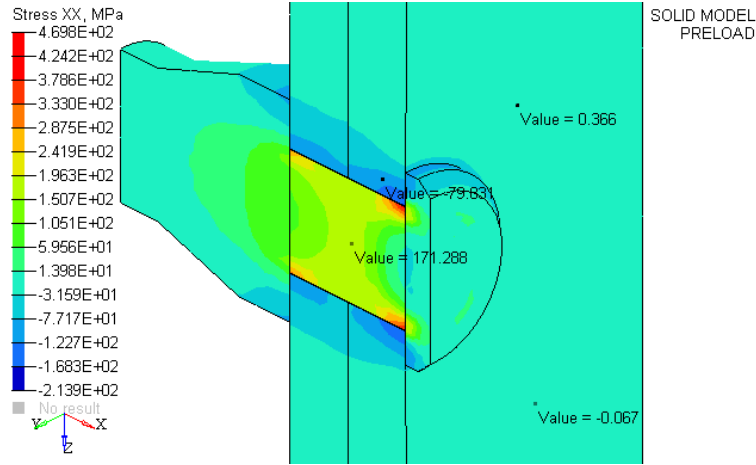


Figure 49. Clamping stresses due to preload application on DJM

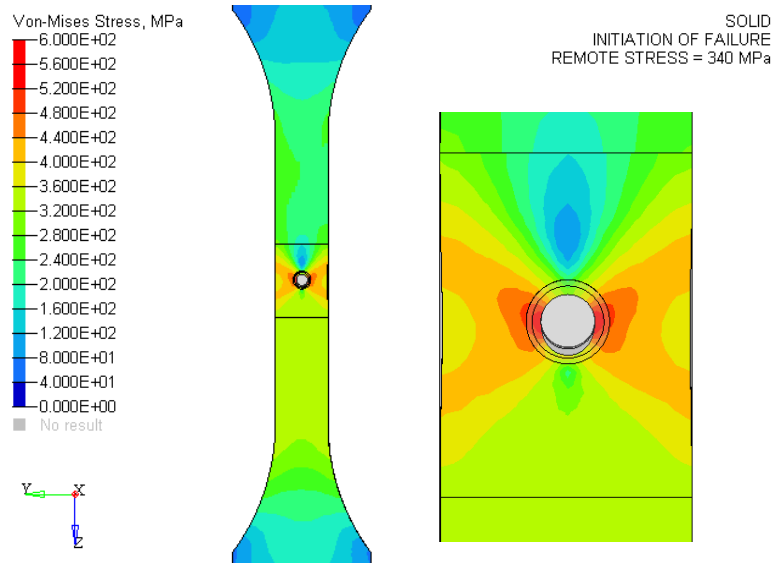


Figure 50. Von Mises stress on main part on DJM

4.2.1.3 Bolt Loads

Figure 51 shows the load on the transfer part, the shear force on bolt, and the LT by the bolt. The LT can be divided into bearing force and friction force on the plates. The bearing load translates into shear force in the bolt, whereas the friction force is dictated by the clamp load of the bolt. As loading begins, load is transferred only through friction until the bolt comes in contact with the hole surface. At this point, the bearing loads take effect, and end fixity of the bolt head and nut occur due to fastener rotation, which results in fastener bending and higher shear force on the fastener. As a result, the LT shifts dependency from friction to bearing load and creates shear force in the bolt. Therefore, as shown in figure 51, at the beginning of the simulation, the majority of the load is transferred by friction; however, toward the end of the simulation, approximately 20% is transferred through friction.

Figure 52 shows the axial force on the bolt of the DJM. The decrease of axial load can be attributed to the following mechanisms occurring in the joint system. On continued application of load, the specimen length increases, and the thickness at the gauge section (in this case, the area around the hole) decreases because of Poisson's ratio effect. As a result, the preload applied to the bolt, which is a tensile load, relaxes—decreasing the axial load. However, continued application of axial load to the specimen results in bearing loads acting on the plate holes. The bearing loads result in compressive forces on the surface of the hole, which causes the localized thickness to bulge up, adding to the axial load. In addition to these mechanisms, because of the end fixity condition of the fastener, the bolt shank experiences bending that also adds to the change in axial loads.

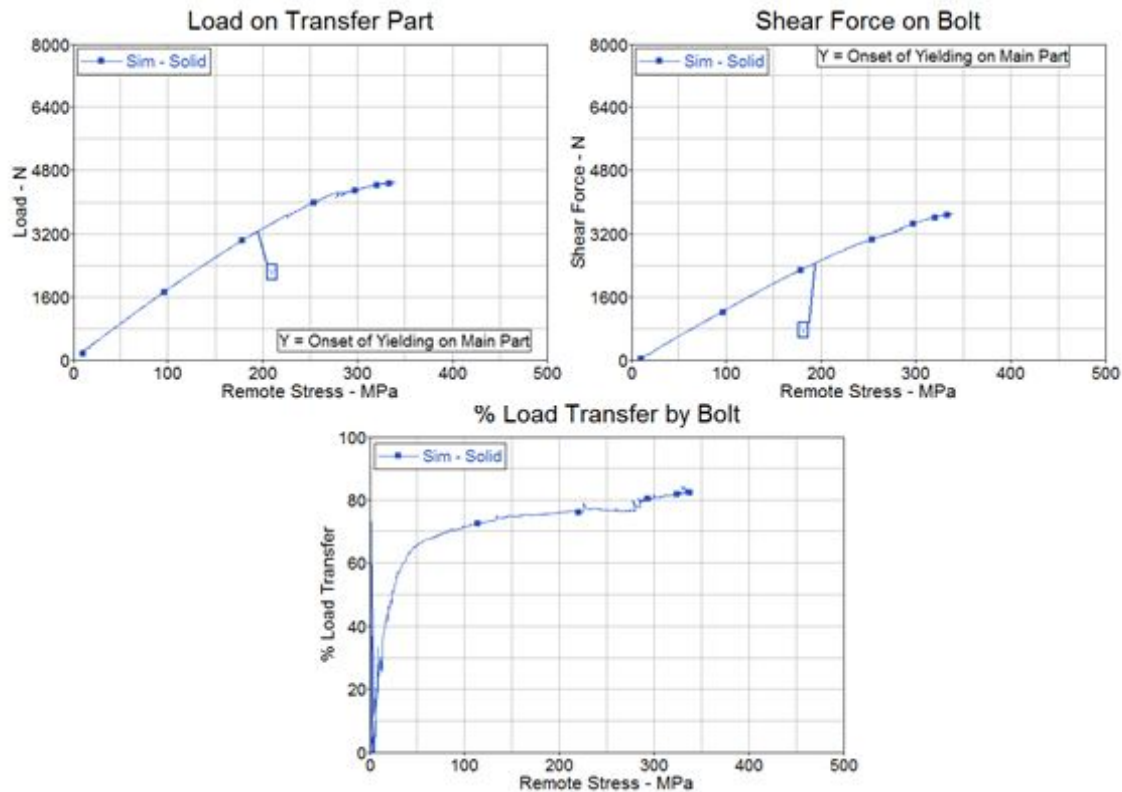


Figure 51. LT by the bolt using the DJM

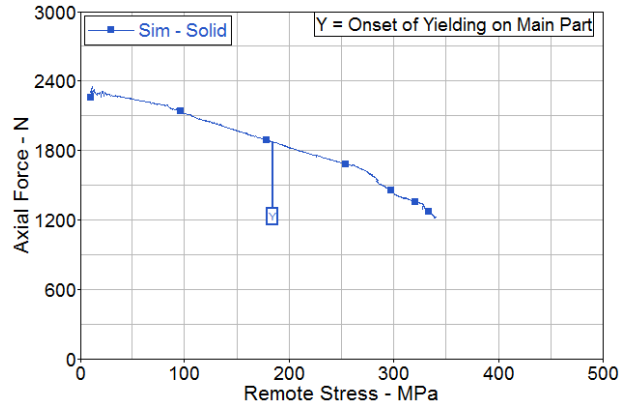


Figure 52. Axial force on bolt using the DJM

4.2.1.4 Energy

The energy levels seen on the DJM simulation are shown in figures 53–54. The majority of the total energy transforms into internal energy and some into interface energy. The eroded internal energy, which is the energy stored in the deleted elements, is included within the internal energy plot shown in figure 53.

Figure 54 shows the distribution of internal energy within the model at the end of the simulation. The total internal energy in the model at failure is approximately 19 J. For the DJM, up to 16 J (approximately 88%) of this internal energy is stored in the main part patch area (see figure 29). Approximately 10% of the total internal energy is stored in the remaining main part, and approximately 1% each in the transfer part and the fixture (joint total approximately 89 %). The energy stored in the bolt is as low as approximately 0.1%.

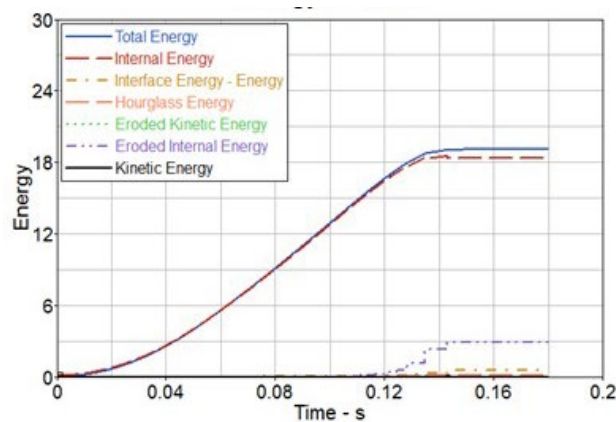


Figure 53. Energy levels using DJM for QS loading

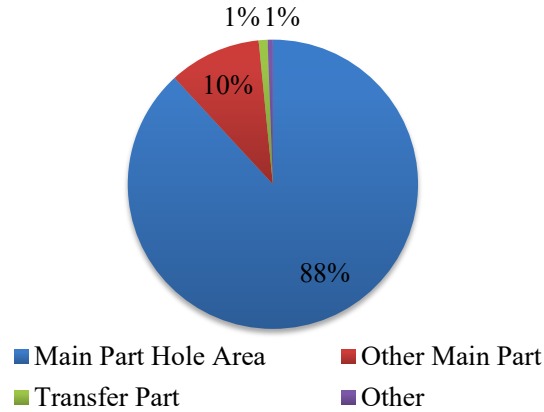


Figure 54. Internal energy distribution using DJM at QS loading

4.2.2 SJMs

For SJMs, shell elements were unable to capture the secondary bending effects described in section 4.1.1. Therefore, the LT was evaluated using equation 10, which uses the CS forces instead of strains.

4.2.2.1 RBE SJM With Hole

Three different variations—one a fine-mesh and two coarse-mesh models—of the RBE SJM with hole (Configuration 1) were compared to the DJM. The RBE SJMs are described in detail in section 3.1.2.1.

4.2.2.1.1 LT Comparison

The comparison of LT between the DJM and the RBE SJM is shown in figure 55. The three variations of Configuration 1 have very similar LT. Because of the joining method, the nodes on the boundary of the hole are rigid and do not undergo any deformations (only rigid body motion). Therefore, the LT for this method was found not to be sensitive to the mesh size.

Note from figure 55 that failure on the RBE SJMs occurred at a higher remote stress compared to the DJM. Because of the rigid hole and use of RBE, stress concentrations occurred at different locations in the models. The stress concentrations are dependent on the orientation of the RBE elements (generally occurring at the first rigid node on the load introduction side). In the DJM, the net section area was smaller because of the fastener hole. In the RBE SJM, the hole is rigidly linked to the bolt node, and therefore behaves as a continuum. As a result, RBE SJMs required larger remote stress to fail.

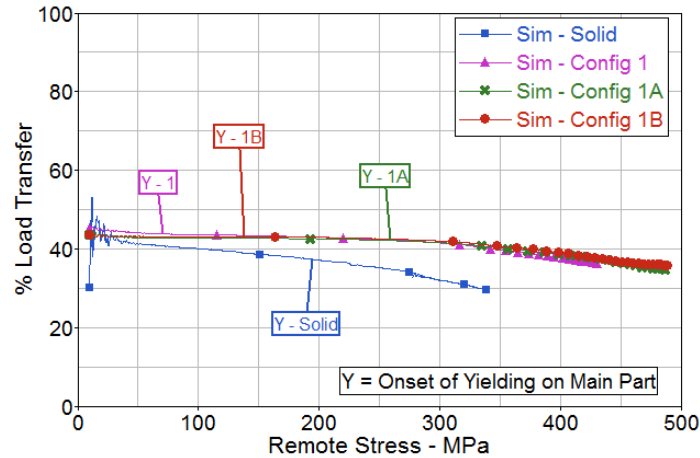


Figure 55. LT comparison of RBE SJMs with hole vs. DJM

4.2.2.1.2 Stress Distribution

The preload measured in the test was applied to all the FE models. For different bolt modeling techniques, the stresses that developed due to preload were quite different. The stresses due to preload on the main part and transfer part of the DJM are shown in figure 49. Because the bolt head and nut are not modeled for the simplified techniques, the localized compressive stresses due to preload—seen on the DJM—are not present (see figure 56). However, the bolt itself is preloaded, which may improve the performance (loads) of the beam itself.

Figure 50 shows the stress contour—at the initiation of failure—on the main part of the DJM, and figure 57 shows the comparison of the state of stress on the main part of the simplified RBE SJMs. These provide an indication of stress concentration locations. It is found that when the mesh is changed on the RBE SJM, the location of the first rigid node on the load introduction side also changes, and therefore the stress distribution in the vicinity of the bolt is different for each case. As a result, the remote stress at which any element reaches yield is also different for each configuration, as shown in figure 58.

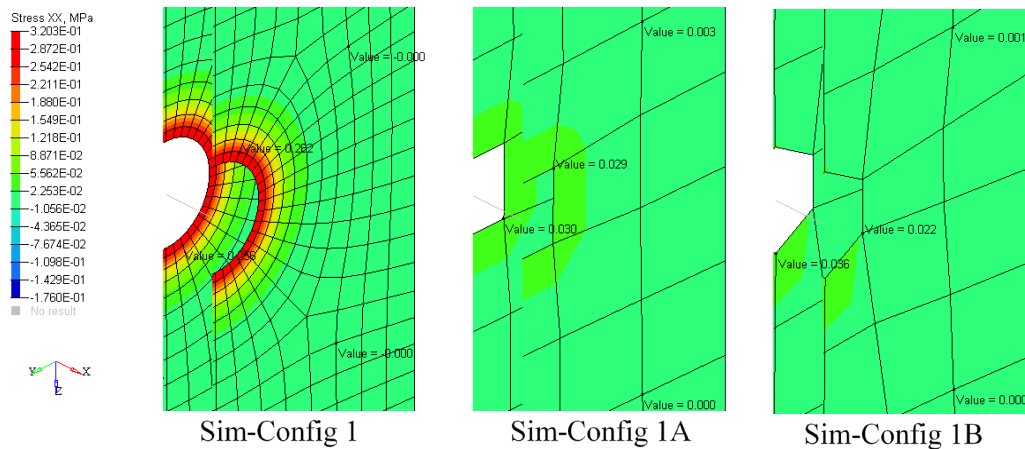


Figure 56. Stresses due to preload on RBE SJM with hole

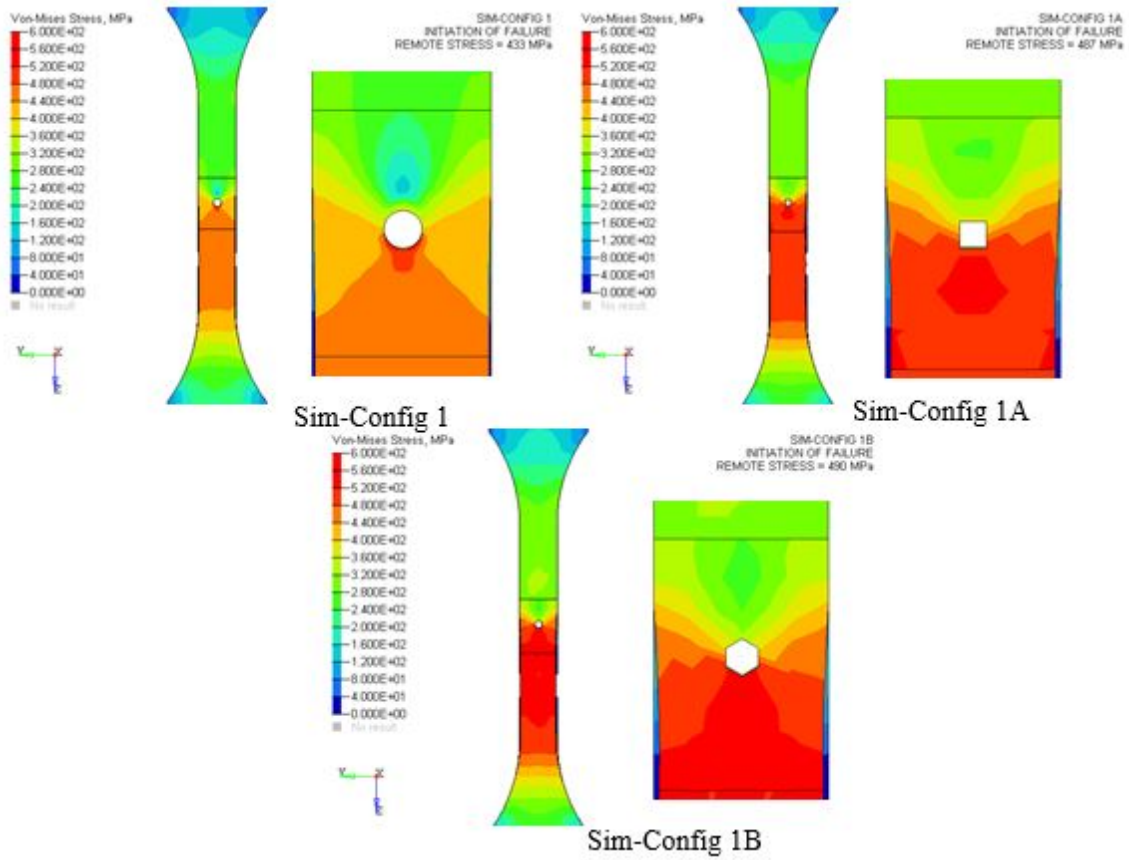


Figure 57. Von Mises stress comparison on main part in RBE SJMs with hole

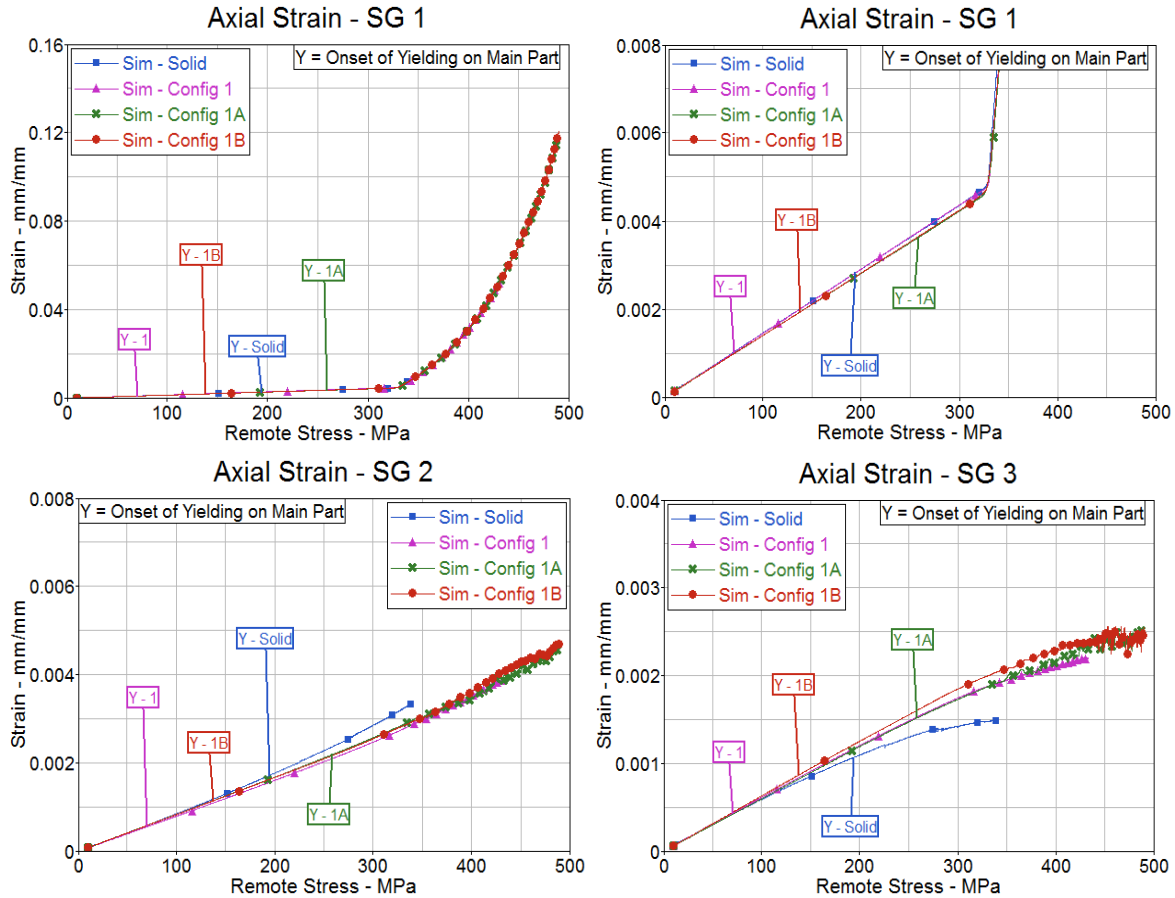


Figure 58. Axial strain vs. remote stress for DJM and RBE SJMs with hole

Strains, at the SG locations shown in figure 23, are compared in figure 58. The top-right plot on figure 58 is a zoom-in of the SG 1 plot on the top left. These strains provide an indication of the state of loading at locations farther away from the fastener hole. For all the simplified RBE SJMs, strains at the SG 1 location correlate well to the DJM. This indicates that the use of shell elements in SJMs was sufficient to capture the stress-strain distribution away from the joint. However, strains at SG 2 and SG 3 are similar to the DJM only at low remote stresses (less than 150 MPa). Deviations in strains between the DJM and simplified RBE SJMs are seen after this point. This can be attributed to the differences in LT for the different models. As shown in figure 55, LT was higher for SJMs, which resulted in higher strains on the transfer part, as seen on figure 58.

4.2.2.1.3 Bolt Loads

The following is an explanation to understand the LT by the bolt versus the LT by friction. For the simplified RBE SJMs, the boundary of the hole was rigid and connected to the bolt, and, therefore, a majority of the load passing through that region gets transferred to the bolt. In addition, as shown in figure 56, the compressive stresses due to bolt preload were negligible on the SJMs, resulting in lower LT through friction. The effect of this can be seen on figure 59, in which the LT by friction lasts for very low remote stresses on the SJMs compared to the DJM. For the DJM, the LT by the

bolt is approximately 75% on average, compared to 96% in the RBE SJMs. The remaining loads are transferred by friction.

Figure 60 shows the comparison of axial loads on the bolt. As expected, the initial axial load for all the models is approximately 2300 N, which is the preload applied to each model. Configurations 1 and 1B show good correlation to the DJM, especially at low remote stresses. The RBE SJMs also exhibit a drop in axial load at the DJM. The orientation of the RBE to the direction of loading is different on Configurations 1A and 1B, and that seems to affect the axial loads.

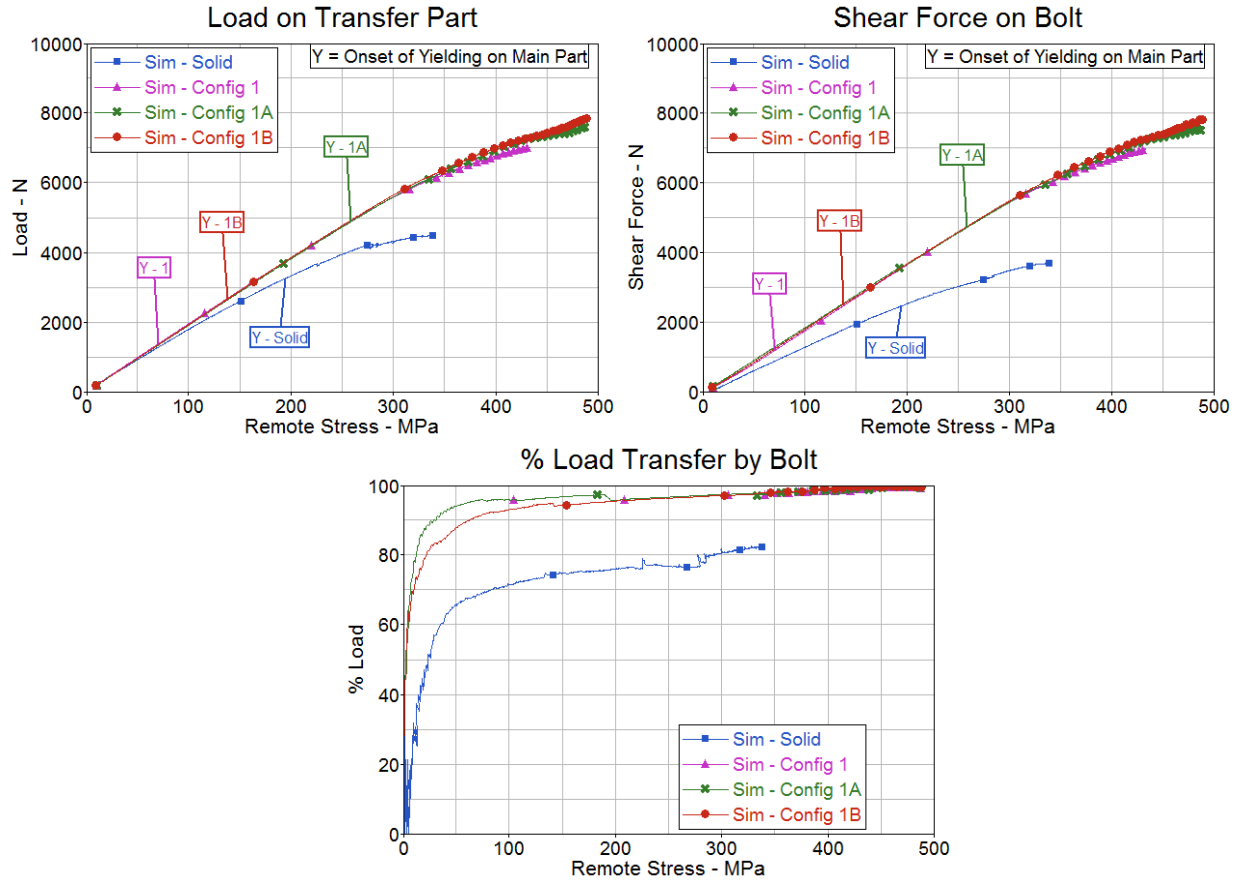


Figure 59. Comparison of LT and shear force on bolt—DJM vs. the RBE SJMs with hole

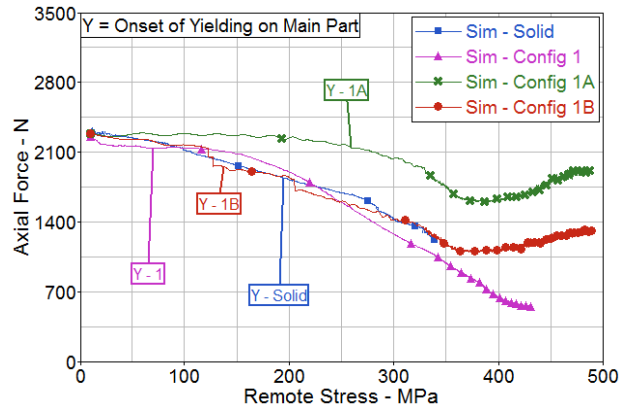


Figure 60. Comparison of axial force on bolt—DJM vs. RBE SJMs with hole

4.2.2.1.4 Energy

Configuration 1B most closely matched the DJM results and, therefore, was chosen as a representative for comparing the energies at failure; it is shown in figures 61–62. As described in section 3.1, the elements in the patch area for both the main and the transfer part were placed in a separate subject component and analyzed. In comparison, the total energy in the DJM at failure is approximately 19 J, whereas the simplified technique shows a total energy of approximately 170 J. RBE simplified SJMs reach failure at much higher remote stress, resulting in higher levels of total energy in the system.

For the DJM, approximately 10% of the total internal energy is stored in the main part away from the patch area and 69% for the simplified model. For the DJM, 88% of the total internal energy is stored in the main part patch area, whereas 28% is stored for the SJM. This can be attributed to the shift in stress concentrations toward the load introduction side, created by the simplified joint. Another indication is the large plastic strains, a contributing factor to the internal energy, that were present at the SG 1 location (see figure 58).

Figure 63 shows the strain energy density for the patch area on both the main and the transfer part. At low remote stresses, the strain energy density on the DJM is higher than the RBE SJMs. High clamp-load stresses present in the DJM explain the high initial strain energy density. The energy density remains high for the DJM at higher remote stresses. Stress concentrations, and therefore plastic deformations, are located within the main part patch areas on the DJM because of the presence of the fastener hole, resulting in higher strain energy.

The energy in the bolt shank, shown in figure 64, is higher in the RBE SJMs compared to the DJM. This result is expected because the shear force on the bolt shank of the SJMs is much higher than the DJM, as shown in figure 59.

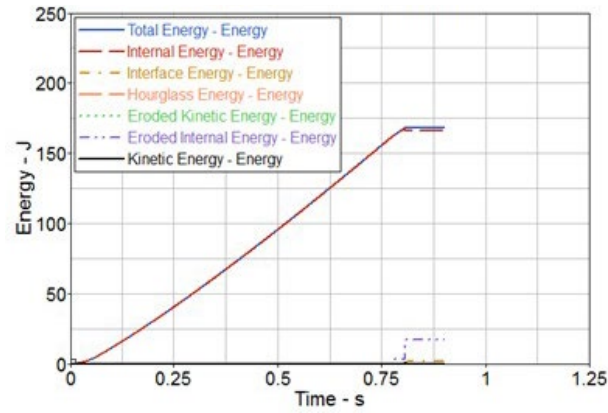


Figure 61. Energy levels in RBE SJM with hole Configuration 1B at QS loading

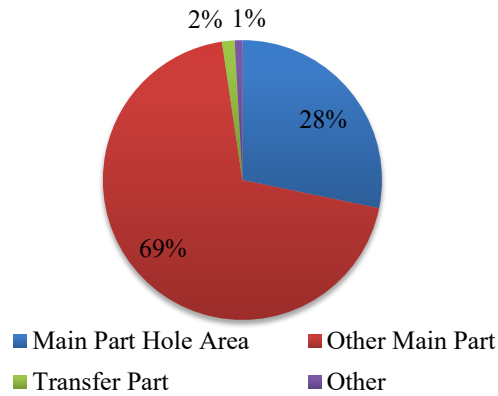


Figure 62. Internal energy distribution in RBE SJM with hole Configuration 1B at QS loading

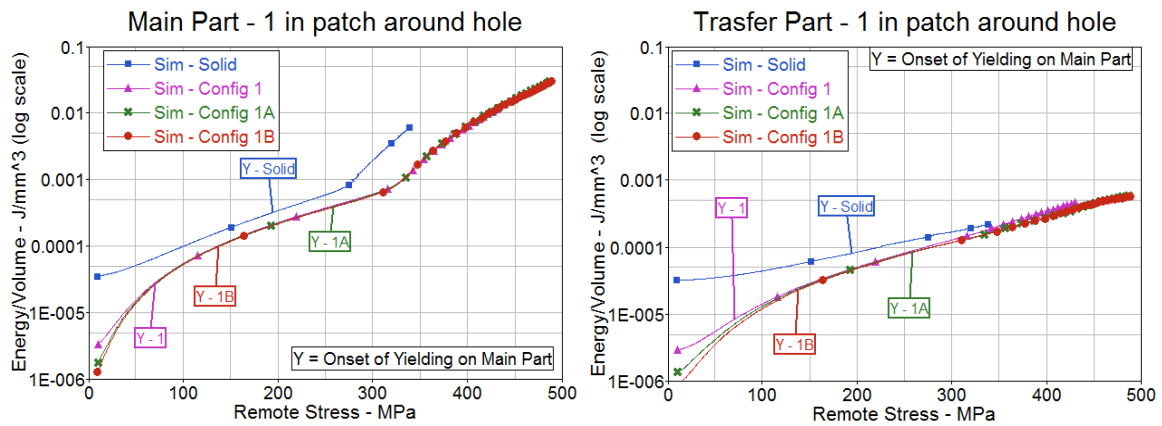


Figure 63. Comparison of strain energy per volume in main and transfer patch area for DJM vs. RBE SJMs with hole

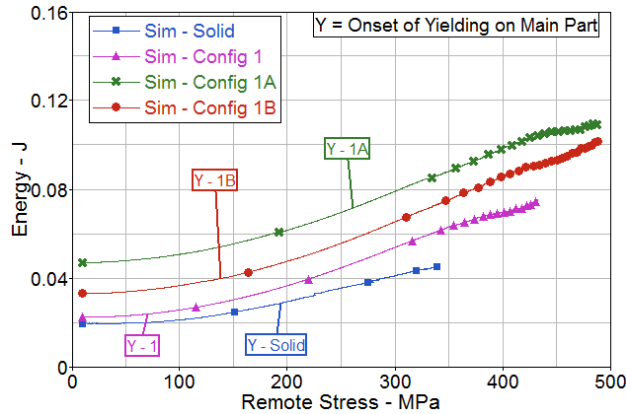


Figure 64. Comparison of strain energy in bolt shank for DJM vs. RBE SJMs with hole

4.2.2.2 Mesh-Independent Spotweld Beam Model

Many different configurations exist for this type of simplified connection, but a select 11 configurations were compared in this study. Six of the configurations (2, 2A, 2B, 2C, 2D, 2E) are such that the location of the beam node (representing the bolt), with respect to the element, is the same on both the main part and transfer part. On the remaining five configurations (2K, 2L, 2M, 2N, 2O), the locations vary. The different configurations are detailed in section 3.1.2.2.

4.2.2.2.1 LT Comparison

The LT of the different configurations of the mesh-independent spotweld beam SJM is compared to the DJM model in figures 65–66. Based on the comparison, considerable scatter is observed in the LT results. Less scatter is observed in the models where the beam contact point is different on the main part and transfer part, as seen on figure 66.

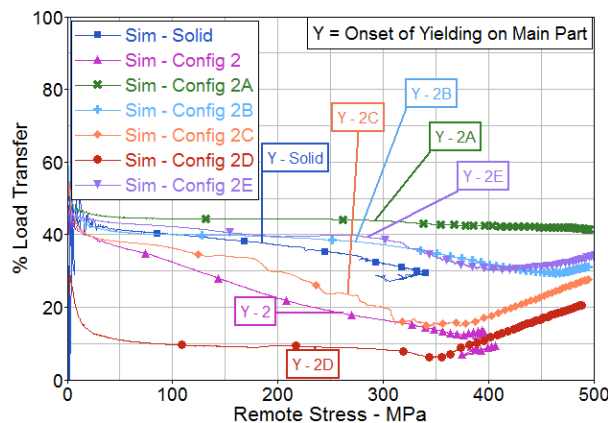


Figure 65. LT Comparison of DJM and mesh-independent spotweld beam SJMs with same mesh on main part and transfer part

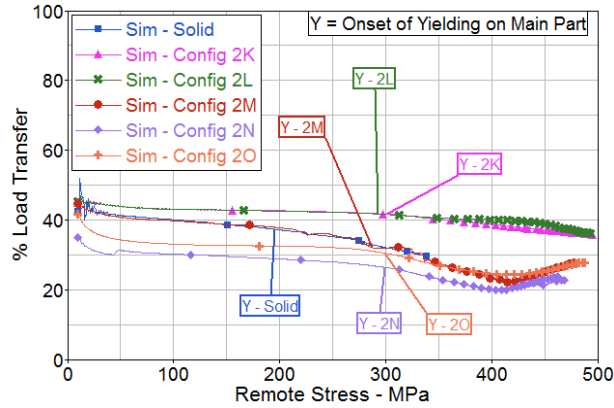


Figure 66. LT Comparison of DJM and mesh-independent spotweld beam SJMs with different mesh on main part and transfer part

An attempt was made to understand the underlying factor affecting the LT. From the explanation on how LS-DYNA programming selection “*CONTACT_SPOTWELD” works (see section 3.4.1), it is understood that the constraints depend on the contact point location. It is speculated that the change in constraints affects the bending stiffness of the contact region, which in turn affects the LT. It can be said that the higher the bending stiffness, the higher the load transferred. To prove this point, four configurations—2B, 2L, 2M, and 2N—are compared. These configurations are chosen because they all have the same contact point on the main part and different contact points on the transfer part, as shown in figure 67. Therefore, the bending stiffness of the transfer part was analyzed for these models and correlated to the LT.



Figure 67. Contact points on main part vs. transfer part for analysis of mesh-independent spotweld beam SJMs

To understand how the bending stiffness changes, the nodes and elements affected by the contact point have been highlighted in figure 68. Analyzing figure 68, it is possible to comprehend that Configuration 2L has the highest bending stiffness on the transfer part followed by Configuration 2B, Configuration 2M, and Configuration 2N with the least. This is also reflected in the comparison of LT of these four configurations shown in figure 69.

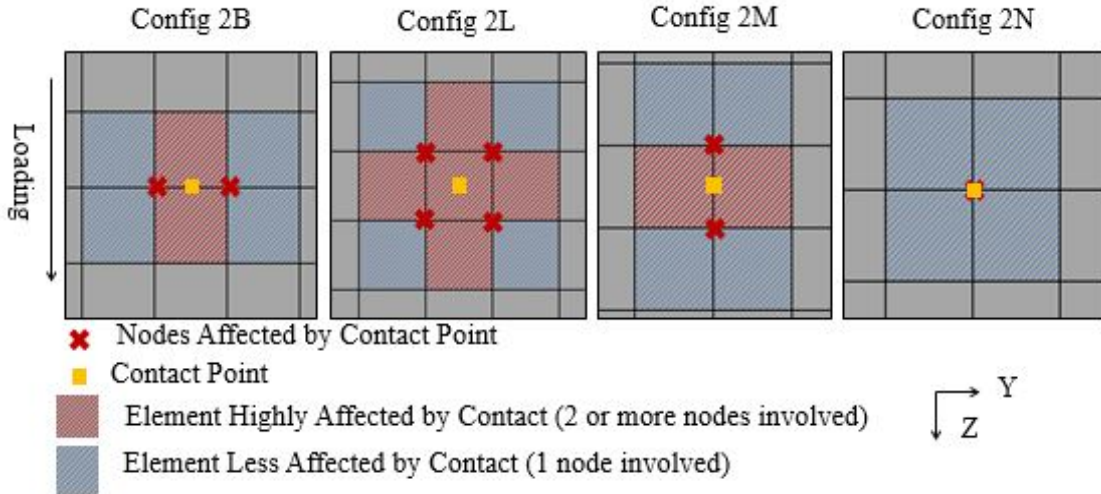


Figure 68. Nodes and elements affected by contact point on transfer part of mesh-independent spotweld beam SJMs

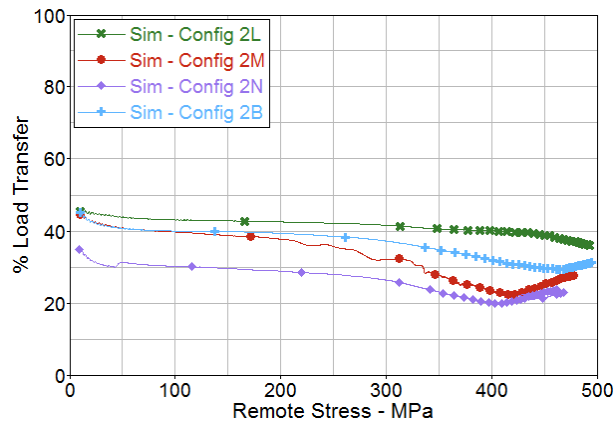


Figure 69. LT comparison of mesh-independent spotweld beam SJMs

To further support this argument, the bending stiffness for each of the models is analyzed by plotting the out-of-plane displacement of the contact region, as shown in figure 70. The configuration with the highest bending stiffness is expected to have the lowest out-of-plane deformations. As expected, figure 70 shows that Configuration 2L has the lowest out-of-plane displacements, followed by Configuration 2B, Configuration 2M, and Configuration 2N. The net out-of-plane displacement on Configuration 2L is 0.206 mm, 0.278 mm on Configuration 2B, 0.294 on Configuration 2M, and 0.322mm on Configuration 2B. These displacement values were calculated using highest and lowest values in front and aft of the connection point, as shown in figure 70. Therefore, it can be concluded that LT in the mesh-independent spotweld beam SJM is affected by the bending stiffness of the localized area of the plates, which changes based on the contact point.

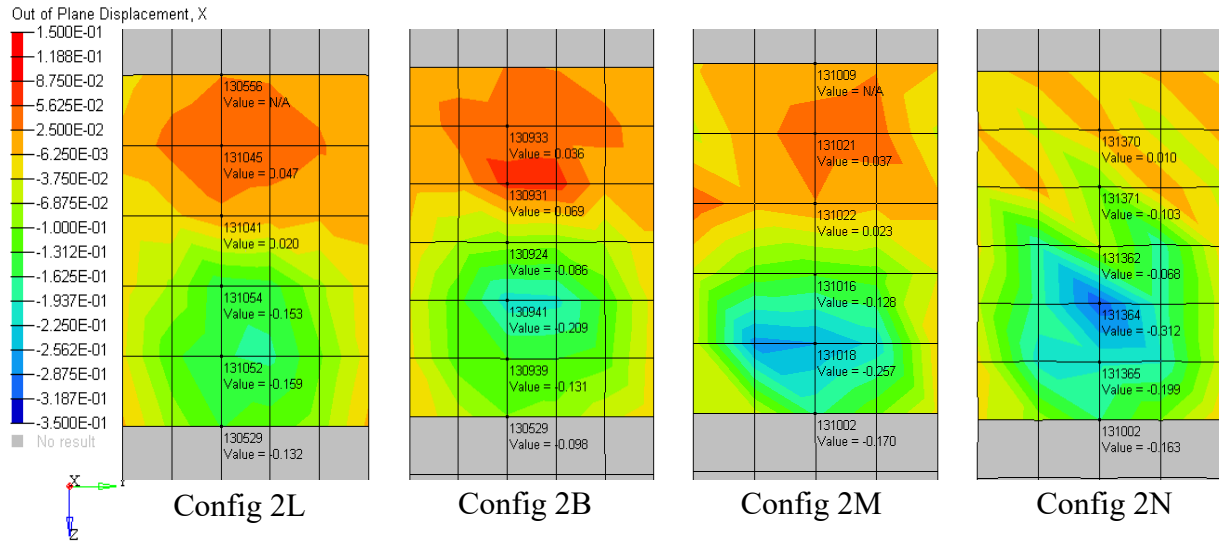


Figure 70. Out-of-plane displacements (mm) of mesh-independent spotweld beam SJMs on transfer part of Configuration 2B, 2L, 2M, and 2N

Analyzing figures 65 and 66, note that Configurations 2A, 2E, 2K, and 2L show higher LT compared to the DJM. Configuration 2B has good correlation to the DJM at low remote stresses, after which the LT remains high. Configuration 2M shows very good correlation to the DJM. To simplify further analysis of this method, Configurations 2, 2C, 2D, and 2N were dropped because of poor LT performance in comparison to the DJM. In the DJM, the net section area is smaller because of the fastener hole, whereas in this SJM the plates are a continuum and, therefore, the net section is larger. As a result, failure occurs at larger remote stress for all the configurations.

4.2.2.2.2 Stress Distribution

The stresses developed on the main part and the transfer part of the DJM due to preload are shown in figure 49. Because the bolt head and nut were not modeled in the simplified techniques, on the application of preload, the localized compressive stresses (seen in the DJM) are not present in such SJMs.

Therefore, the stress levels seen on the SJMs are very small, as shown in figures 71–72.

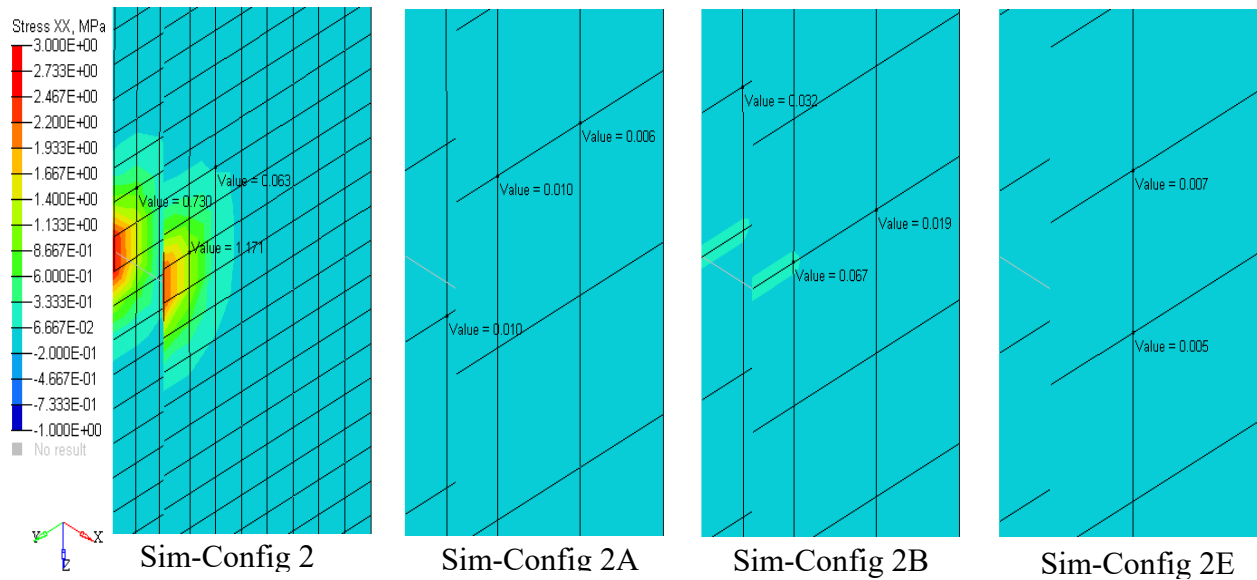


Figure 71. Stresses due to preload application in mesh-independent spotweld beam SJM with same mesh on main part and transfer part

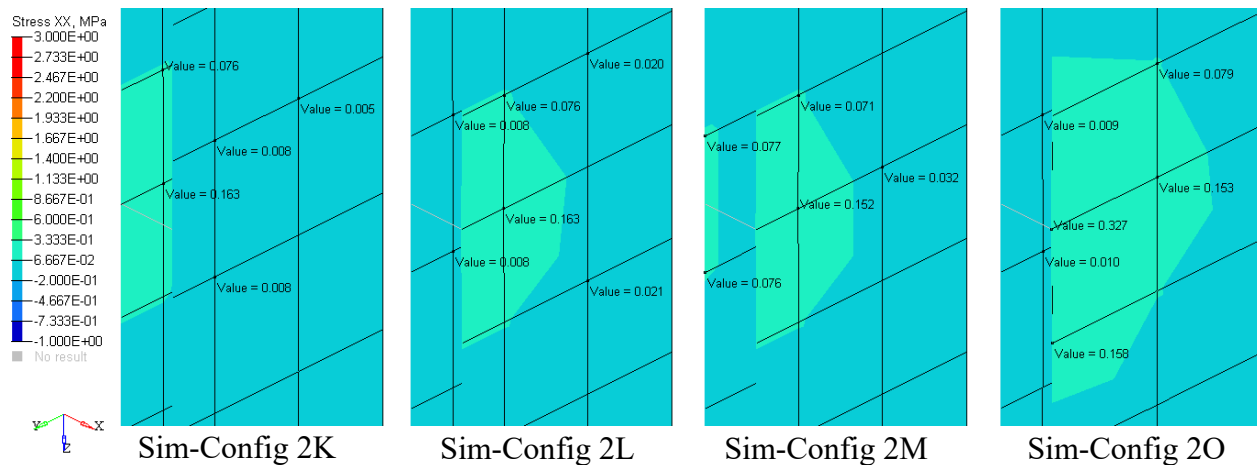


Figure 72. Stresses due to preload application in mesh-independent spotweld beam SJMs with different mesh on main part and transfer part

Figures 73–74 show the state of stress at the initiation of failure on the main part. The DJM can be found in figure 50. Only the fine-mesh model, Configuration 2, shows a similar state of stress when compared to the DJM. The rest of the configurations analyzed in this section do not compare well with the DJM. Although the fine-mesh configuration exhibits a better stress distribution, note that the minimum element size used for that model is 0.3 mm, which makes it impractical for use in large FE models. For this simplified technique, the stresses are highly concentrated on the load introduction side of the main part, which is where necking—and ultimately failure—occurs. Changing the contact point location does not drastically affect the stress concentrations in this simplified model, but the remote stress at which any element reaches yield is also different for each configuration, as shown in figures 75–76.

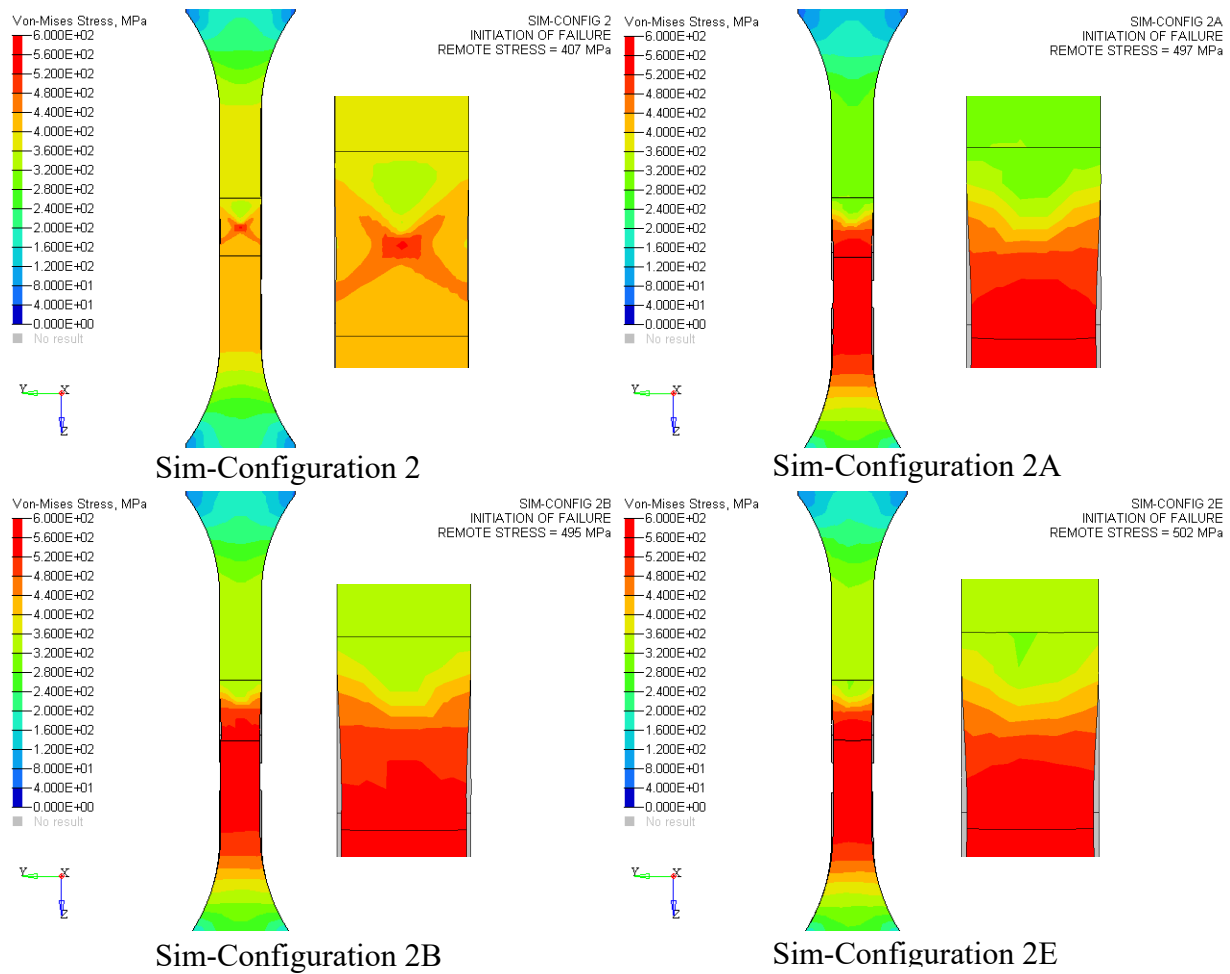


Figure 73. Von Mises stresses distribution in main part at failure initiation, for mesh-independent spotweld beam SJM configurations, with identical mesh on main and transfer part

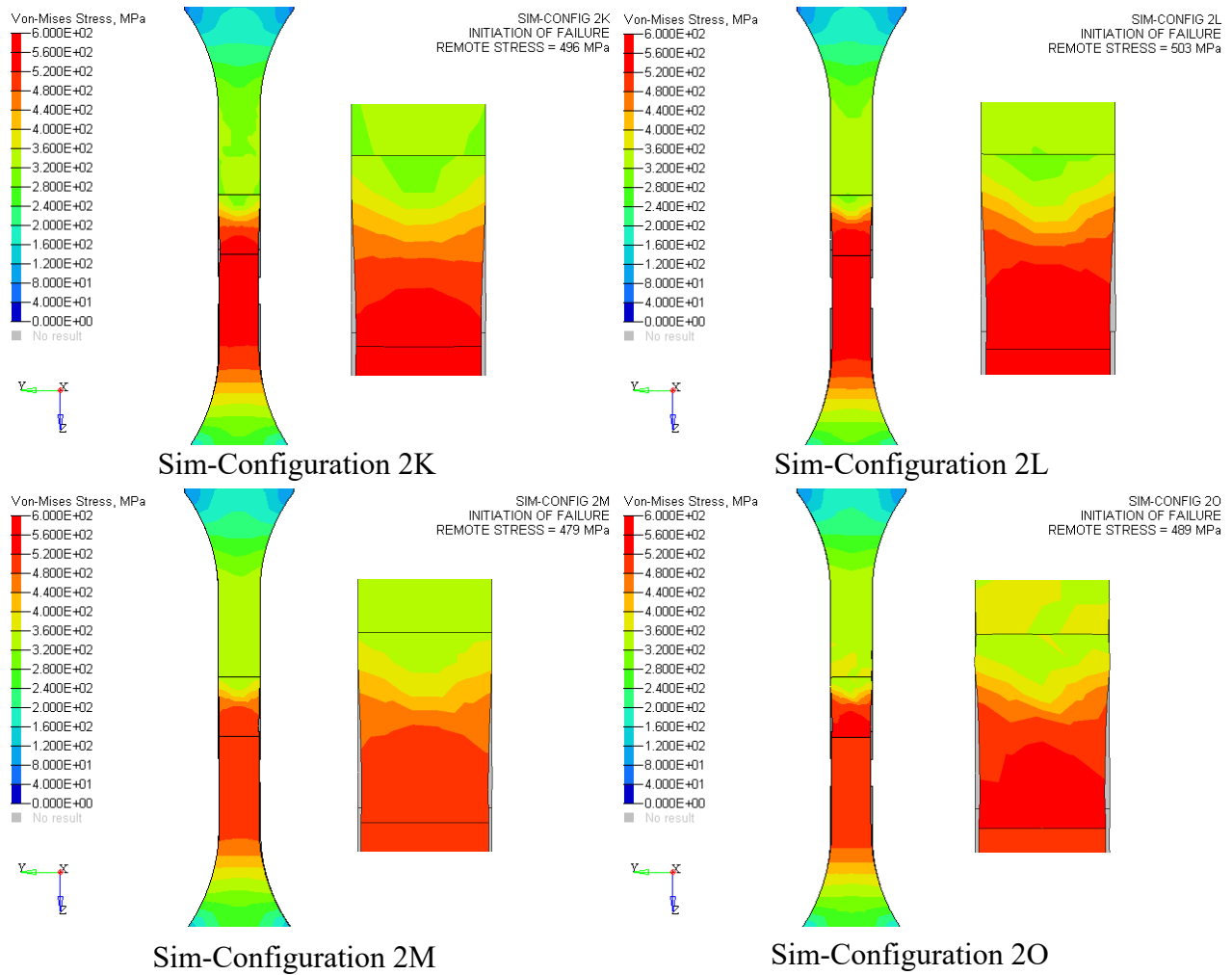


Figure 74. Von Mises stresses distribution in main part at failure initiation, for mesh-independent spotweld beam SJM configurations, with different mesh on main and transfer part

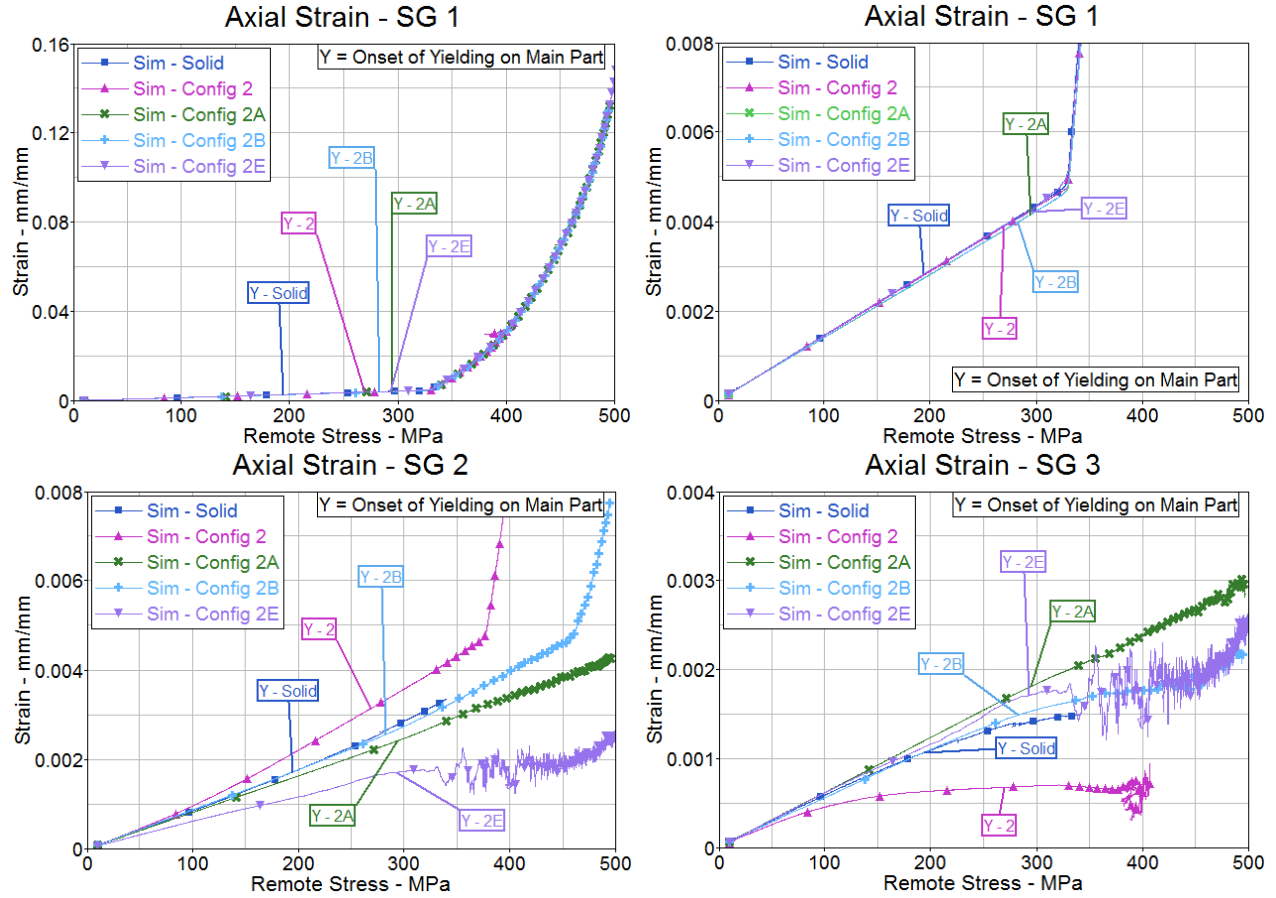


Figure 75. Axial strain introduced in the DJM and the mesh-independent spotweld SJMs for Configurations 2, 2A, 2B, and 2E

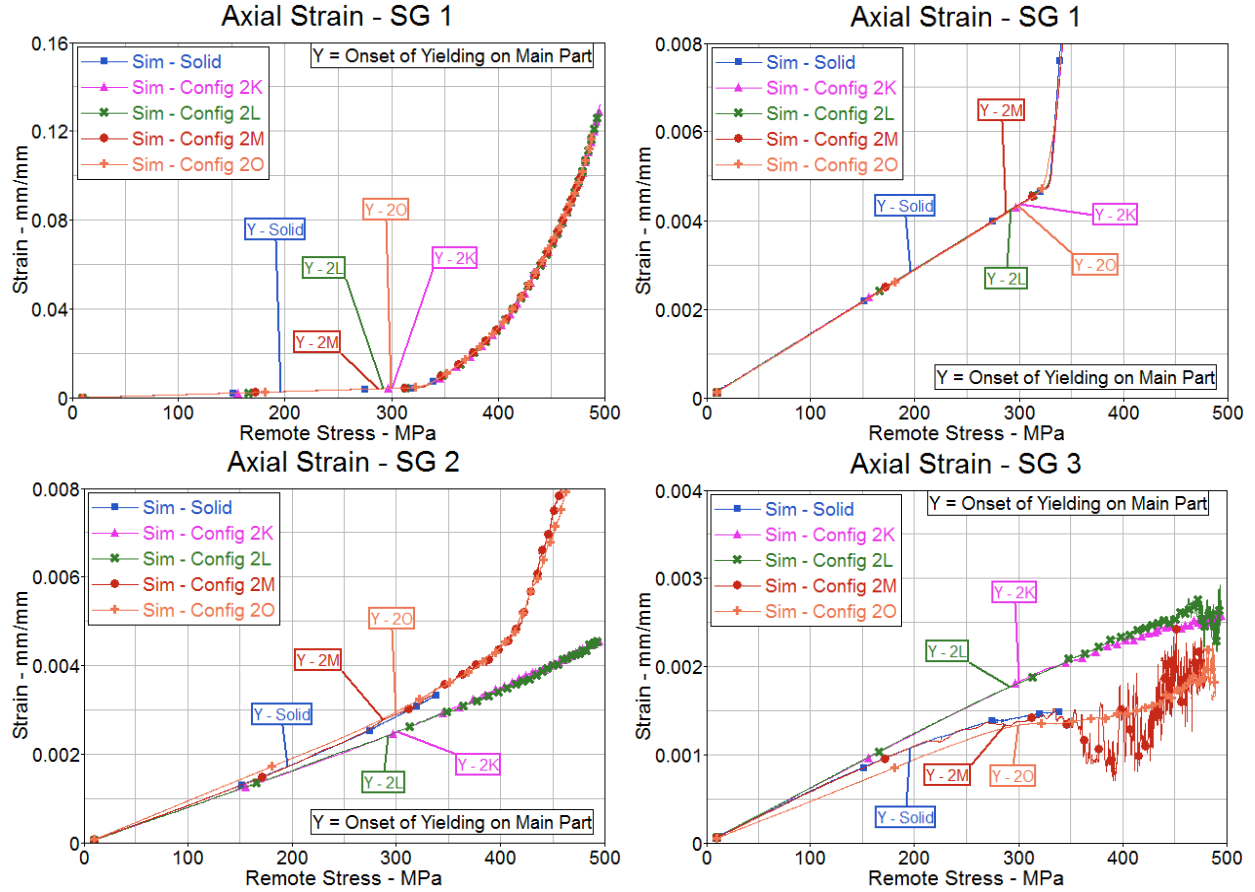


Figure 76. Axial strain introduced in mesh-independent spotweld SJMs for Configurations 2K, 2L, 2M, and 2O

Strains—at the SG locations shown in figure 23—are compared in figures 75–76. The top right plot on figures 75–76 is a zoom-in of the SG 1 plot on the top left. These strains provide an indication of the state of loading at locations farther away from the fastener hole. For all the models of this simplified technique, strains at SG 1 location are in good correlation to the DJM. This indicates that the use of shell elements in SJMs is sufficient to capture the stress-strain distribution. However, strains at SG 2 and SG 3 have large deviations between the DJM and the SJMs. This can be attributed to the differences in LT for the different models. Configuration 2M and 2B, which showed good correlation of LT to the DJM, also show very good correlation of strains to the DJM.

4.2.2.2.3 Bolt Loads

The shear force on the bolt and the load recorded on the LT part are compared to deduce the LT by the bolt, and that transferred by friction, as shown in figures 77–78. For the SJM configurations, the compressive stresses due to bolt preload are negligible, and therefore result in lower load transferred through friction. Figures 77–78 show that the LT by friction lasts for very low remote stresses on the SJMs compared to the DJM. For the DJM, the load transferred by the bolt is approximately 75% on average compared to 96% in the SJM configurations. The remaining load is transferred by friction.

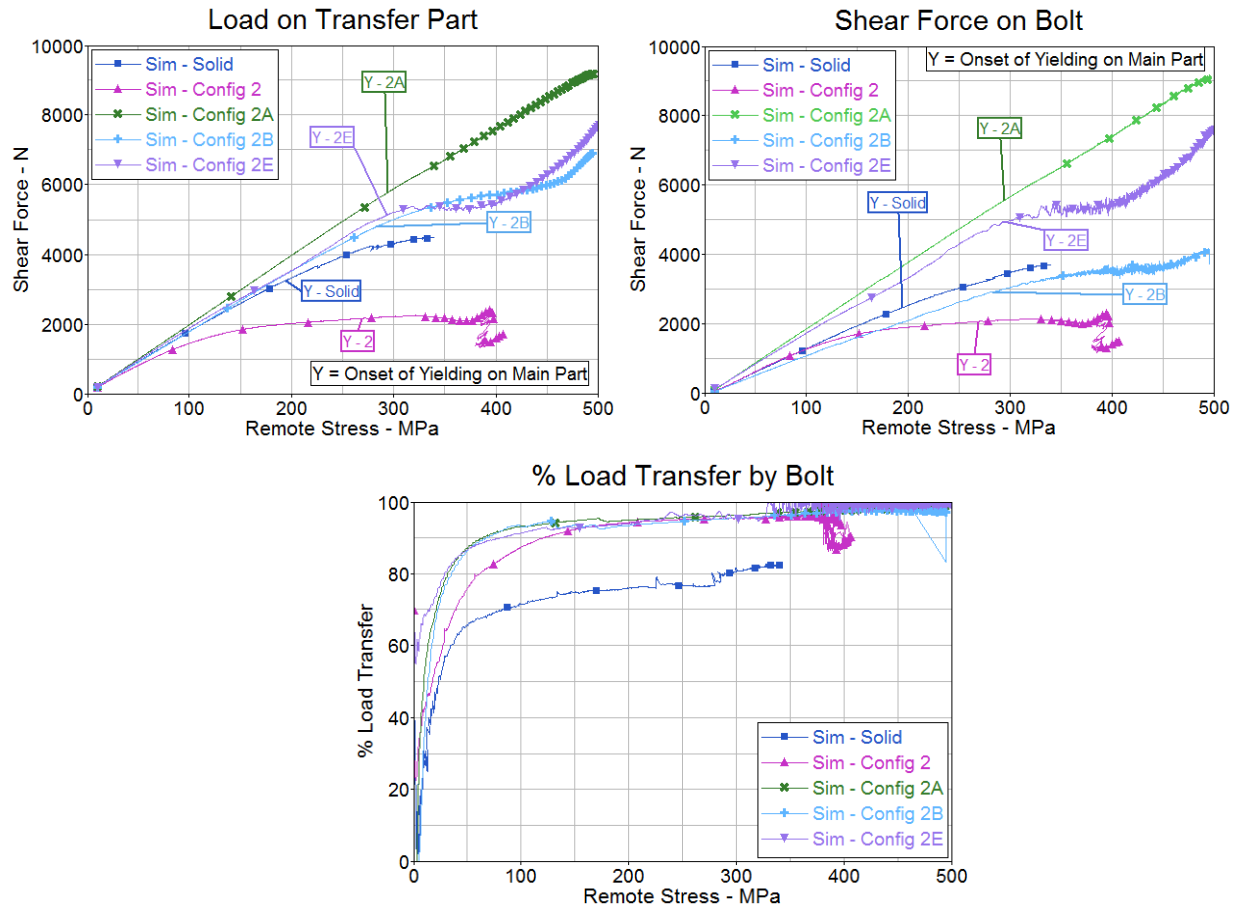


Figure 77. Comparison of LT by the bolt for the DJM and the mesh-independent spotweld beam SJMs—identical mesh on main and transfer part

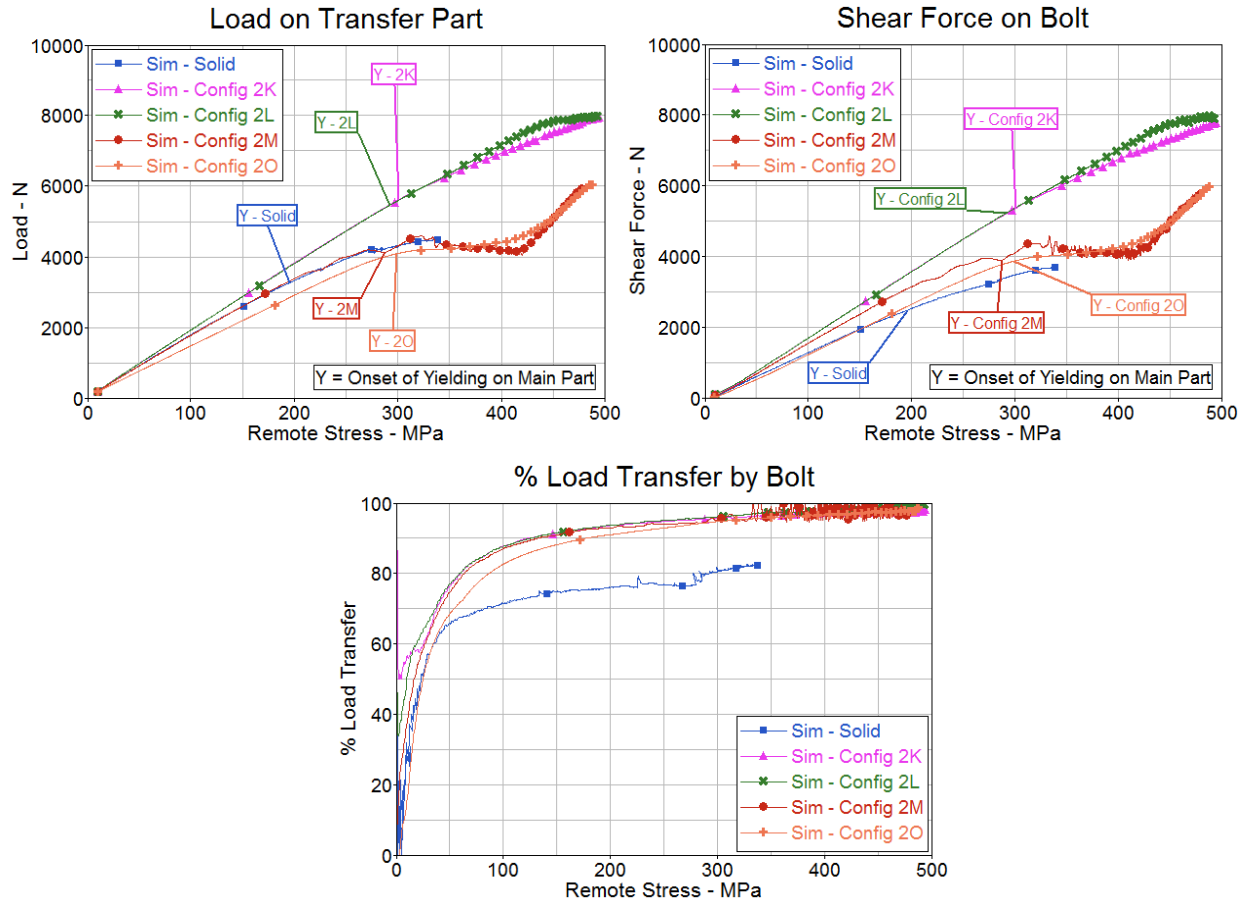


Figure 78. Comparison of LT by bolt for the DJM and the mesh-independent spotweld beam SJM—different mesh on main and transfer part

Figure 79 shows the comparison of axial loads on the bolt. As expected, the initial axial load for all the models is approximately 2300 N, which is the preload applied to all the models. For all the SJMs except Configuration 2 (fine-mesh), note that the axial load is sustained or drops very slightly, up to 300 MPa of remote stress, after which there is a drop and then an increase in the axial load. The levels of the drop and increase vary between the different simplified configurations. The localized bending stiffness varies for this simplified model, as discussed in section 4.2.2.2.1, therefore affecting the fastener rotation and the axial loads. The correlation of axial loads to the DJM of this simplified technique is poor. In the DJM, the bolt undergoes complex loading due to the end fixity of head and nut, bearing loads, and high friction on faying surfaces. None of these phenomena are present in the simplified model.

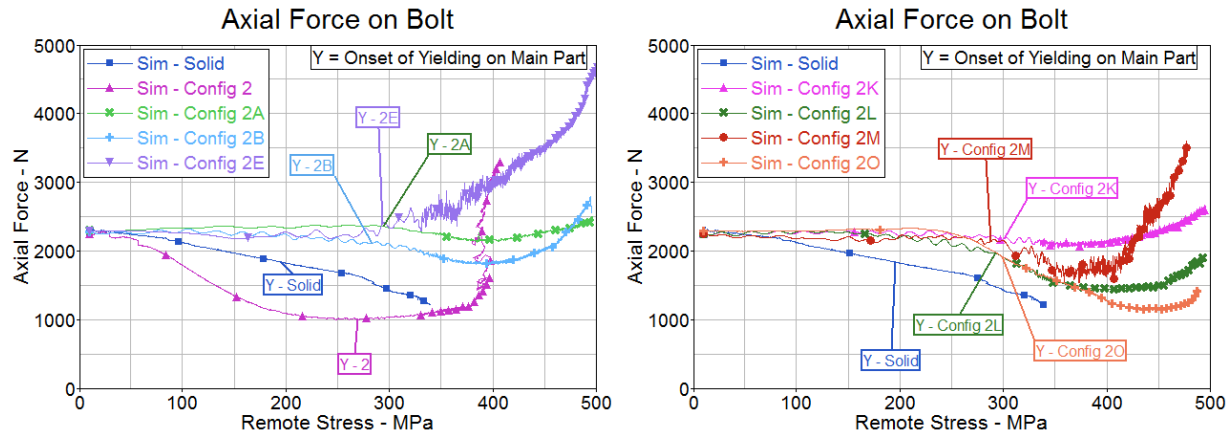


Figure 79. Axial load in the DJM and the mesh independent spotweld beam SJMs

4.2.2.2.4 Energy

Configuration 2B most closely matched the DJM results and, therefore, was chosen as a representative for comparing the energies at failure; it is shown in figures 80–81. Configuration 2B is used to represent the energy distribution for this SJM. In comparison to the energy distribution in the DJM (total energy approximately 19 J), this SJM shows a total energy of approximately 185 J. The energy levels are higher for the SJM because they reach failure at a much higher remote stress, therefore introducing more energy into the structure. In addition, the majority of the internal energy stored in the main part of the DJM is 10% versus 130 J or 68% for the simplified model. The main part patch area stores 16 J or 88% for the DJM and 30% for the simplified model. This can be attributed to the shift in stress concentrations, toward the load introduction side, created by the simplified joint. Note that the energy distribution for Configuration 2B may not apply to the fine-mesh model like Configuration 2, but because the focus of this study is modeling crashworthiness, larger mesh models are emphasized.

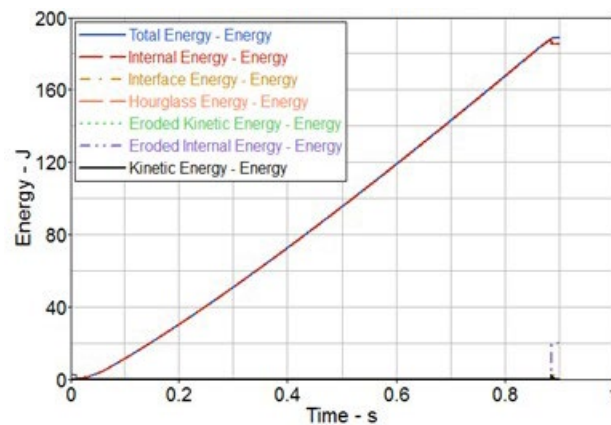


Figure 80. Energy level in spotweld beam SJM at QS loading for Configuration 2B

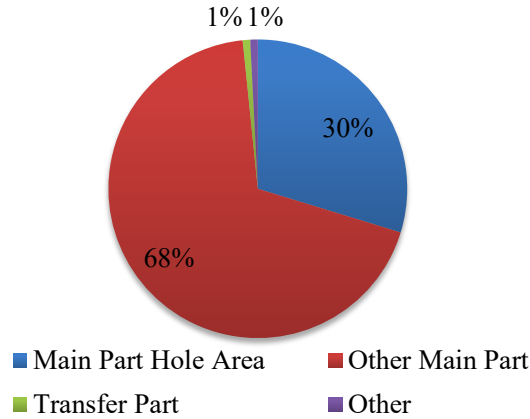


Figure 81. Internal energy distribution in spotweld beam SJM at QS loading for Configuration 2b

Figures 82–83 show that at low remote stress, the strain energy on the main part, and the transfer part of the DJM is much higher than the simplified configurations. This is due to the presence of high clamp-load stresses in the DJM. At higher remote stress, the energies of the simplified configurations are closer to that of the DJM, especially for the mixed configurations (Configurations 2K, 2L, 2M, and 2O).

The energy in the bolt shank, shown in figure 84, is higher in most simplified configurations compared to the DJM. This result is expected because the shear force on the bolt shank of the SJMs is much higher than the DJM, as shown in figures 77–78.

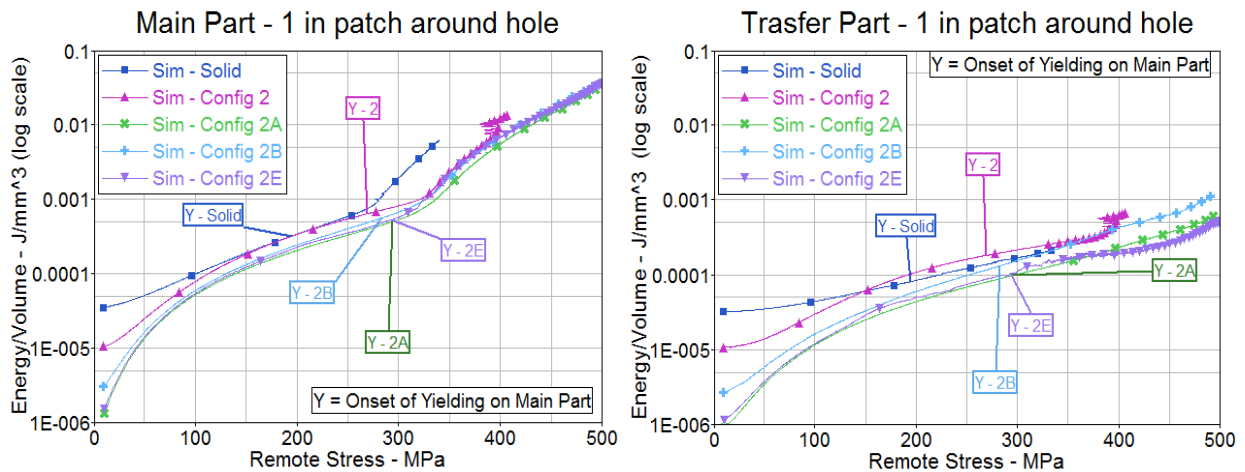


Figure 82. Strain energy per volume in a main part patch for spotweld beam SJMs Configurations 2, 2A, 2B, and 2E

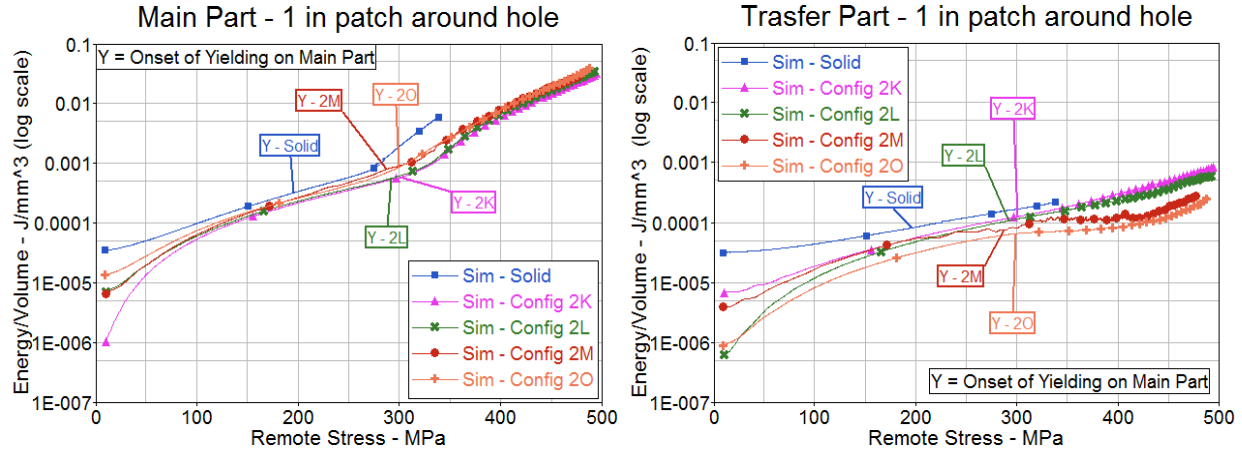


Figure 83. Strain energy per volume in the main and transfer patch area for the DJM and the spotweld beam SJMs Configurations 2K, 2L, 2M, and 2O

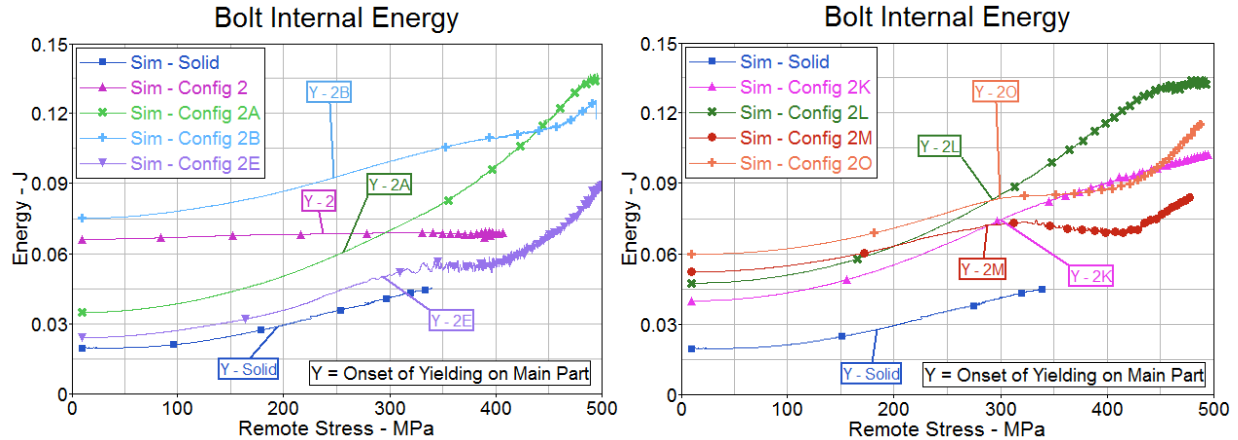


Figure 84. Comparison of bolt internal energy for the DJM and the mesh-independent spotweld SJMs

4.2.2.3 Mesh-Independent Spotweld Beam SJM With EP

For the mesh independent spotweld beam SJM with EP, three different variations are compared to the DJM. The primary entity of this LS-DYNA joint definition, “*CONTACT_SPOTWELD,” is the same as that used in Configuration 2. Detailed explanation of the setup of this SJM technique is provided in section 3.1.2.3.

4.2.2.3.1 LT Comparison

The comparison of LT is shown in figure 85. Because the joining mechanism is the same as Configuration 2, the LT also behaves in the same way, as described in section 4.2.2.2.1. The LT results of Configurations 3A and 3B are similar to Configuration 2A, which indicates that increasing the material stiffness of the joining element does not affect the LT. Similar to the results obtained in Configuration 2, the fine-mesh model of Configuration 3 also shows less LT than the DJM. However, the fine-mesh model, Configuration 3, does show some improvement in LT

compared to the fine-mesh model, Configuration 2. Therefore, LT is more sensitive to contact than the material characteristics in contact-based joining mechanisms.

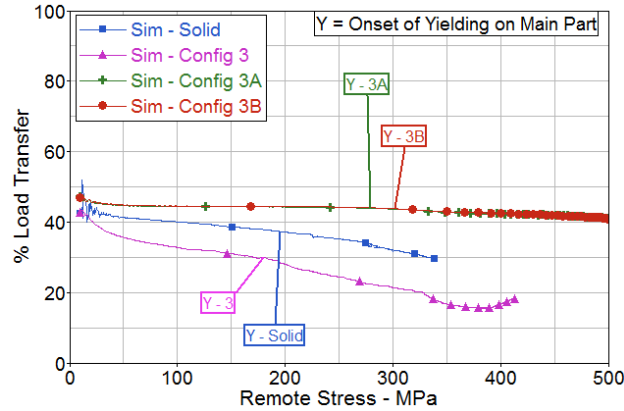


Figure 85. LT comparison of DJM and the mesh-independent spotweld beam SJMs with EP

4.2.2.3.2 Stress Distribution

The stress levels developed because of preload application are shown in figure 86. The localized effect of preload is not captured by this technique and, therefore, preload may not have an effect on the overall performance of the system.

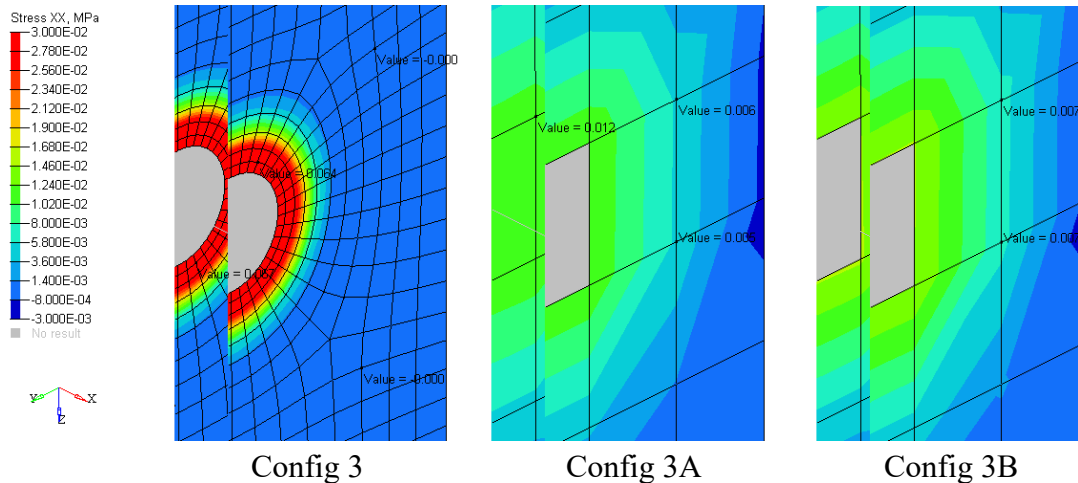


Figure 86. Stresses due to preload application of mesh-independent spotweld beam SJMs with EP

The state of stress at failure initiation on the main part is shown in figure 87. Overall, the configurations do not compare well with the DJM. Although the fine mesh, Configuration 3, exhibits a better stress distribution, it should be noted that the minimum element size used for that model is 0.3 mm, which makes it impractical for use in large FE models. For this simplified technique, the stresses are highly concentrated on the load introduction side of the main part, which

is where necking and ultimate failure occur. Note that because of the different configurations, the remote stress at which any element reaches yield is also different for each configuration, as indicated in the curves such as figure 88.

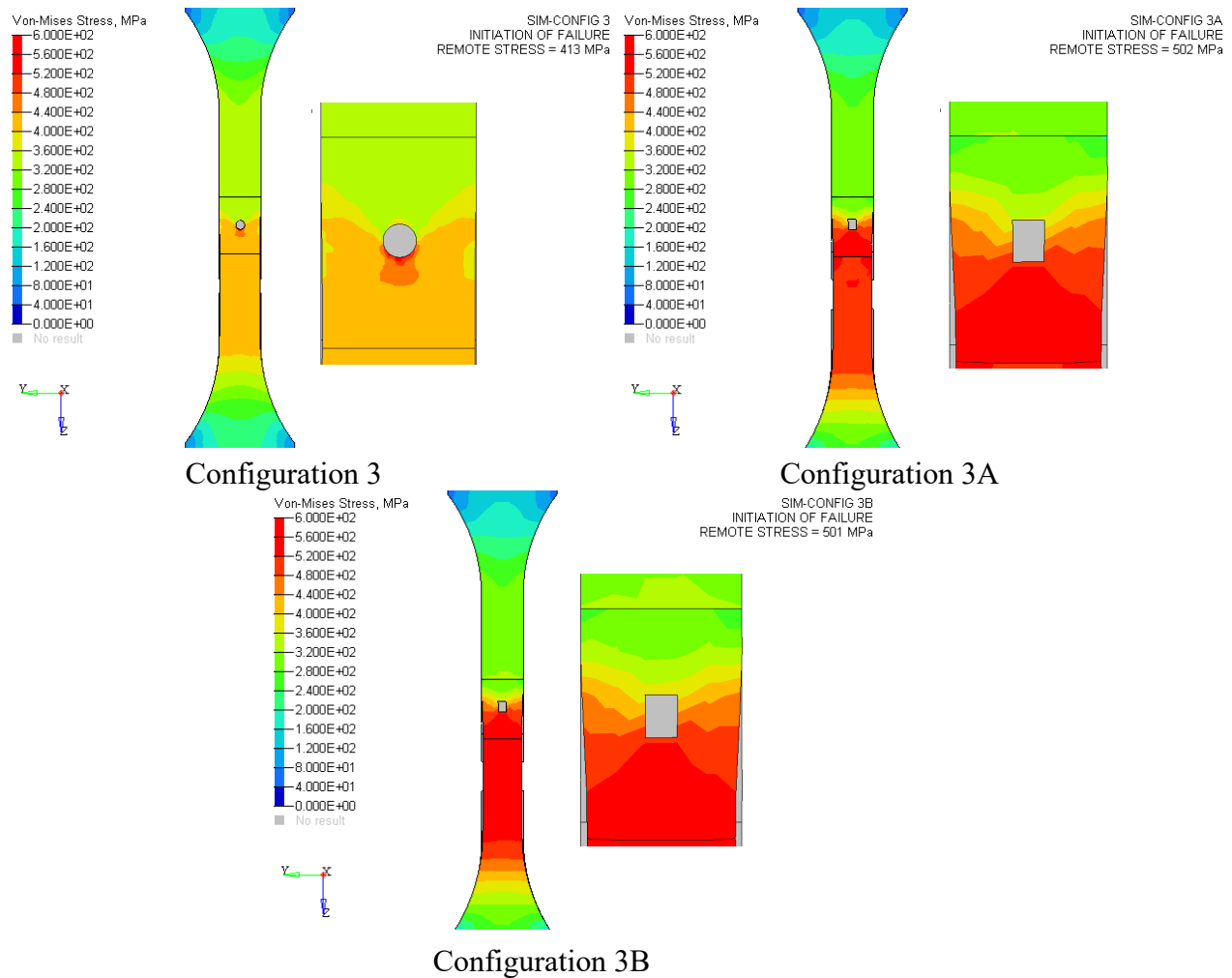


Figure 87. Von Mises stresses on main part at initiation of failure of mesh-independent spotweld beam SJMs with EP

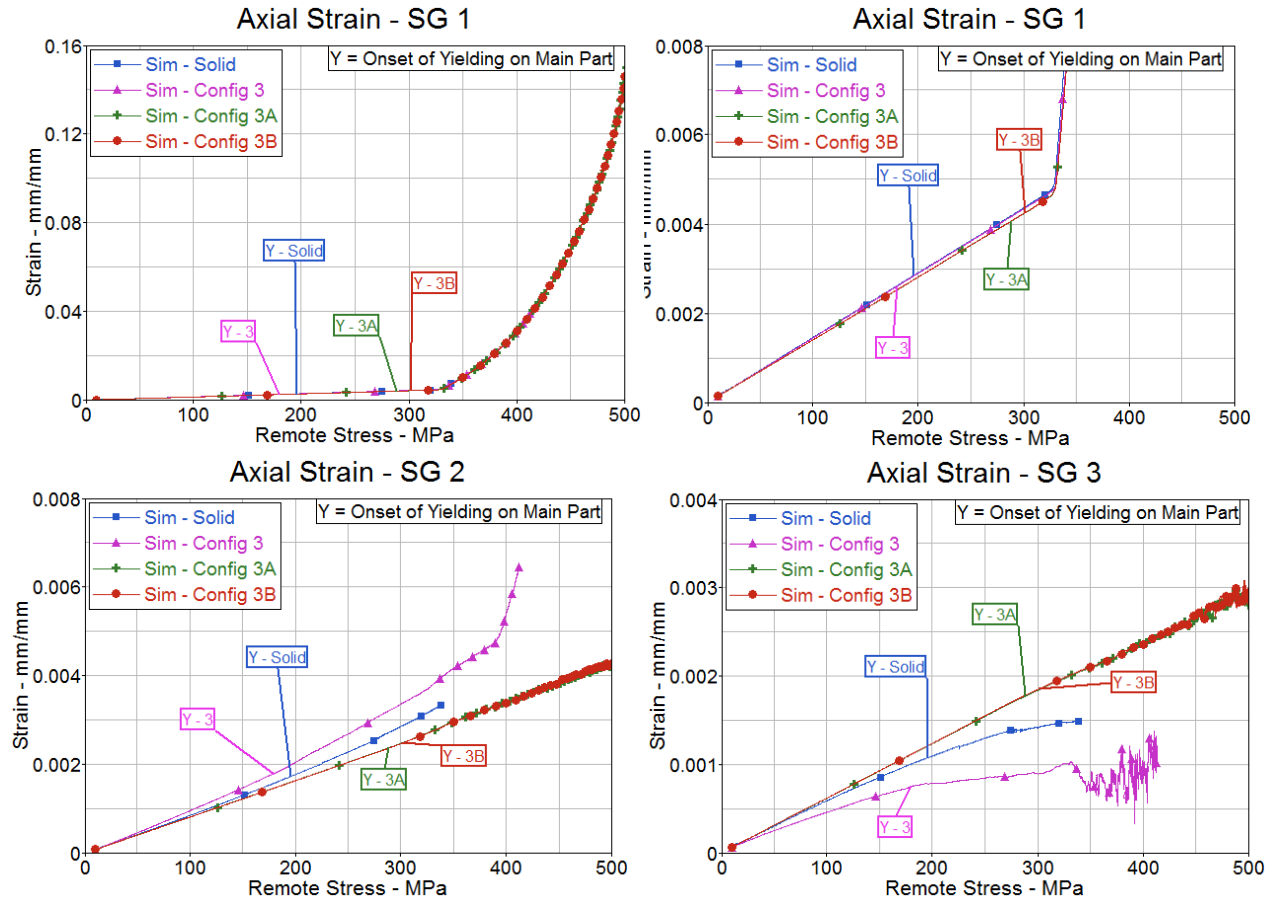


Figure 88. Axial strain introduced in mesh-independent spotweld SJM with EP

Strains at the SG locations shown in figure 23 are compared in figure 88. The top-right plot on figure 88 is a zoom-in of the SG 1 plot on top left. For this simplified technique, strains at the SG 1 location correlate well to the DJM. Strains at the SG 2 and SG 3 locations have deviations between the DJM and SJMs. This can be attributed to the differences in LT for the different models, as described in section 4.2.2.3.1.

4.2.2.3.3 Bolt Loads

The shear force on the bolt and the load recorded in the cross-section plane on the transfer part are compared to determine the LT by the bolt, and that transferred by friction, as shown in figure 89. For these SJMs the compressive stresses due to bolt preload are negligible, and therefore results in lower load transferred through friction, and higher through the bolt. The effect of this can be seen in figure 89, in which the LT by the bolt is lower in the DJM and higher in the SJMs. For the DJM, the LT by the bolt is approximately 75% on average compared to 96% for this SJM.

Figure 90 shows the comparison of axial loads on the bolt. As expected, the initial axial load for all the models is approximately 2300 N, which is the preload applied to each model. The axial loads of this simplified technique do not correlate well to the DJM. In the DJM, the bolt undergoes complex loading due to the end fixity of head and nut, bearing loads, and high friction on faying surfaces. None of these phenomena are present in the simplified model.

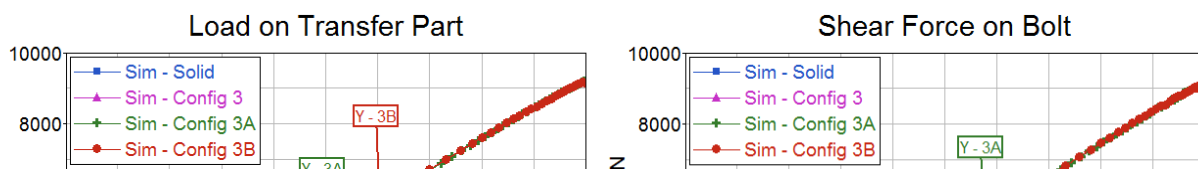


Figure 89. Comparison of LT by bolt for the DJM and the mesh-independent spotweld beam SJMs with EP

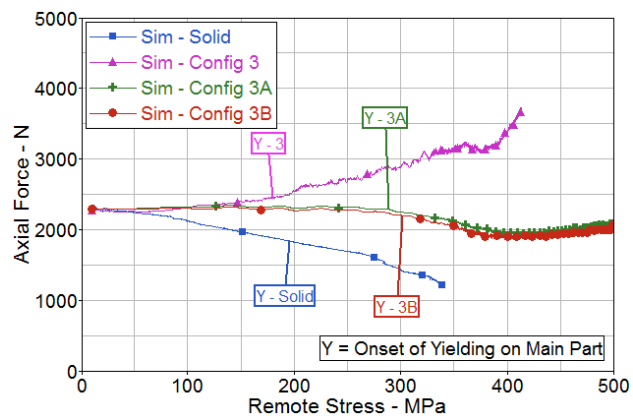


Figure 90. Comparison of axial force on bolt for the DJM vs. the mesh-independent spotweld beam SJMs with EP

4.2.2.3.4 Energy

Configuration 3B most closely matched the DJM results and, therefore, was chosen as a representative for comparing the energies at failure; it is shown in figures 91–92. In comparison to the energy distribution in the DJM (total energy = 19 J), this SJM shows a total energy of approximately 205 J. The energy levels are higher for the SJMs because they reach failure at much higher remote stress, therefore introducing more energy into the structure. In addition, for this SJM, the majority of the internal energy (approximately 151 J or 74%) is stored in the main part away from the patch area compared to 10% for the DJM. The main patch area stores 88% of the total internal energy for the DJM and 24% for the SJM. This can be attributed to the shift in stress concentrations, toward the load introduction side, created by the simplified joint. Note that the energy distribution shown for Configuration 3B may not apply to the fine-mesh model like Configuration 3. Because the focus of this study is large models, the fine-mesh models are not emphasized.

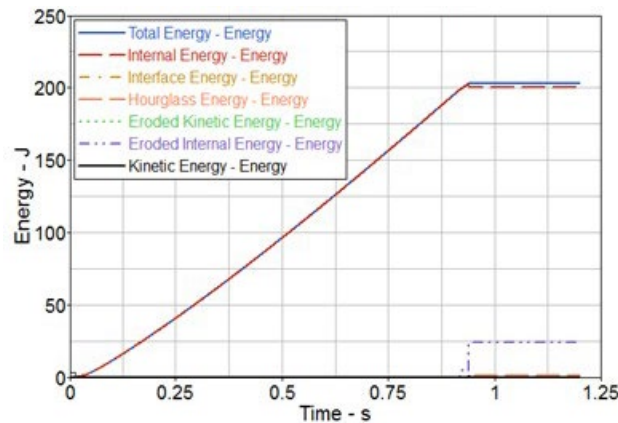


Figure 91. Energy level in spotweld beam SJM with EP at QS loading for Configuration 3B

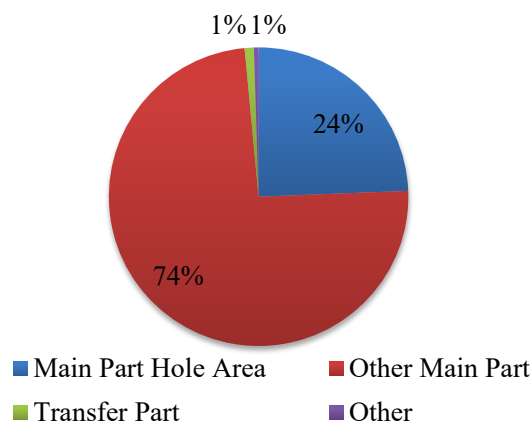


Figure 92. Internal energy distribution in spotweld beam SJM with EP at QS loading for Configuration 3B

Based on figure 93, at low remote stress, the strain energy density on the main part and the transfer part of the DJM is considerably higher than on the simplified configurations because of the presence of high clamp-load stresses in the DJM. At higher remote stresses, the energies of the simplified configurations approach the DJM. Because the plastic deformations occur further away from the patch area on the main part, the energy density on the DJM is always higher than the SJMs for the same remote stress.

The energy in the bolt shank, shown in figure 94, is higher in the simplified configurations compared to the DJM. This result is expected because the shear force on the bolt shank of the SJMs is higher than the DJM, as shown in figure 89.

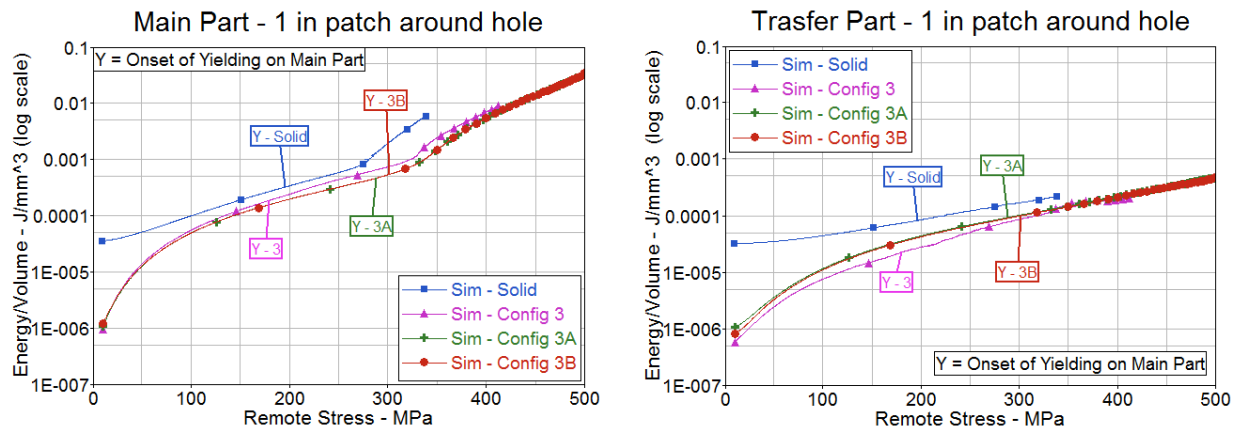


Figure 93. Strain energy per volume in the patch areas for the DJMs and the spotweld beam SJMs with EP

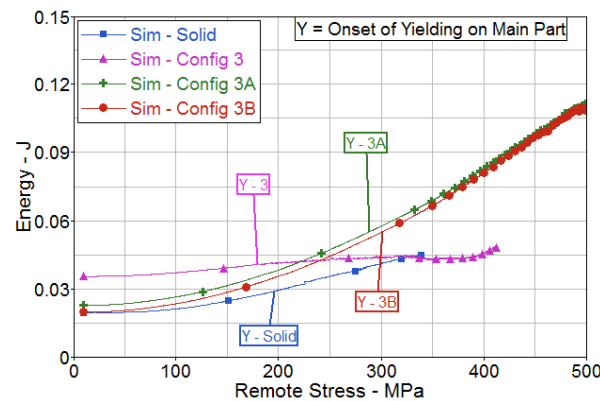


Figure 94. Comparison of bolt internal energy for the DJM vs. spotweld beam SJMs with EP

4.2.2.4 RBE SJM Without Hole

Many different configurations exist for the RBE SJM without a hole, but only nine are compared in this study. For each configuration, RBE elements are used in different quantities and orientations. Detailed explanation of the setup of this SJM technique is provided in section 3.1.2.4.

4.2.2.4.1 LT Comparison

Based on the comparison of LT shown in figure 95, all the configurations of this simplified technique except Configuration 4H show a similar trend in LT. The LT for this simplified technique drops at a fast rate at low remote stress and is then sustained throughout the loading compared to the DJM, in which the LT has a gentle drop throughout the loading. The LT behaves in the same way as described in section 4.2.2.2, except that a larger area within the plate is constrained to the bolt through the various RBE. As a result, the bending stiffness within the localized area of the joint is low, and therefore the LT is low.

Configurations 4A through 4D exhibit the lowest LT and are equal to each other. Note that Configurations 4A through 4D are similar, with only a change in the orientation of the RBE. This indicates that if the mesh is identical, the orientation of the RBE does not affect the LT. For Configurations 4E through 4H, the RBE has six nodes, but the location of the RBE nodes with respect to the mesh changes, as shown in figure 38. These configurations show a change in LT, which indicates that this method is mesh sensitive. Configurations 4B, 4C, and 4D are omitted in further analysis because they show poor performance of LT and are similar to Configuration 4A. In addition, Configurations 4F and 4H are also omitted from further analysis. This is because Configurations 4F and 4H show lower LT than Configurations 4E and 4G.

All the configurations of this simplified technique reach failure at higher remote stress than the DJM. In the DJM, the net section area is smaller because of the fastener hole, whereas in this simplified model, the plates are a continuum and, therefore, the net section is larger. As a result, failure occurs at larger remote stress for all the configurations.

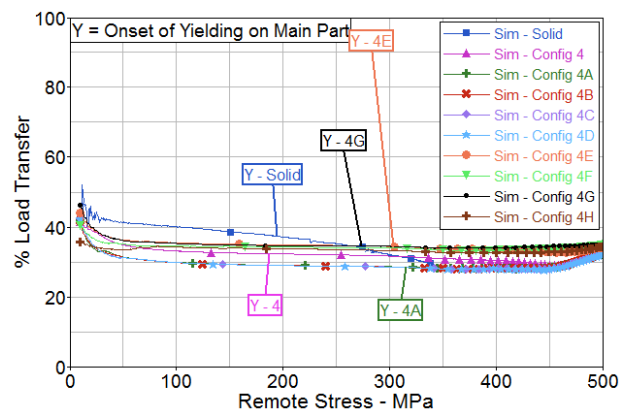


Figure 95. LT comparison of DJM vs. RBE SJMs without hole

4.2.2.4.2 Stress Distribution

Because the bolt head and nut are not modeled in the simplified techniques, on preload application the localized compressive stresses (seen in the DJM) are not present and, therefore, the localized stress levels seen on figure 96 are very small.

The state of stress at the failure initiation on the main part is shown in figure 97. The fine-mesh model, Configuration 4, shows slightly better comparison to the DJM, whereas the rest of the configurations do not compare well with the DJM. For this simplified technique, the stresses are highly concentrated on the load introduction side of the main part, which is where necking and ultimate failure occur. Changing the contact point location does not drastically affect the stress concentrations in the SJMs, but the remote stress at which any element reaches yield is different for each configuration, as indicated in the curves such as figure 98.

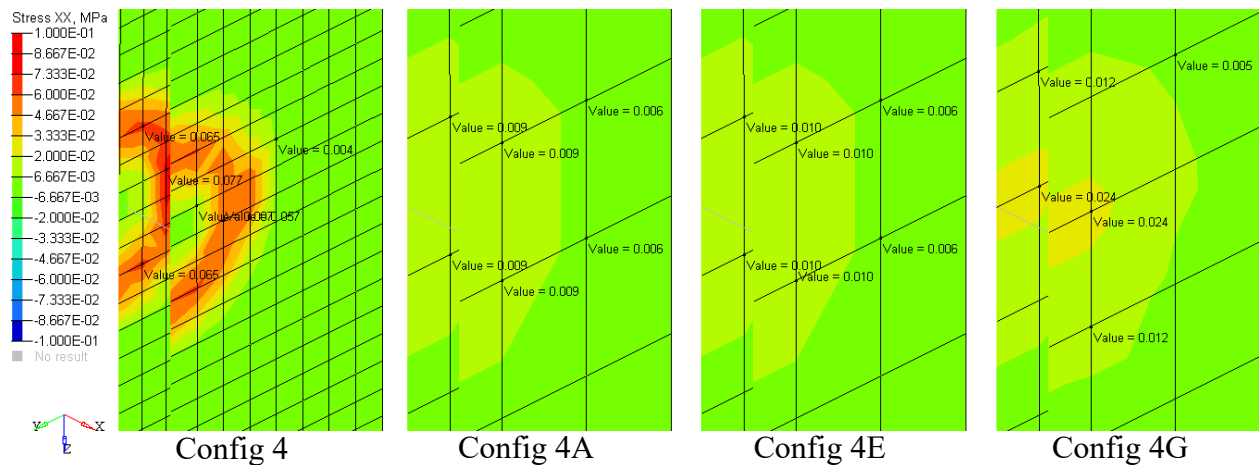


Figure 96. Stresses due to preload application of RBE SJMs without hole

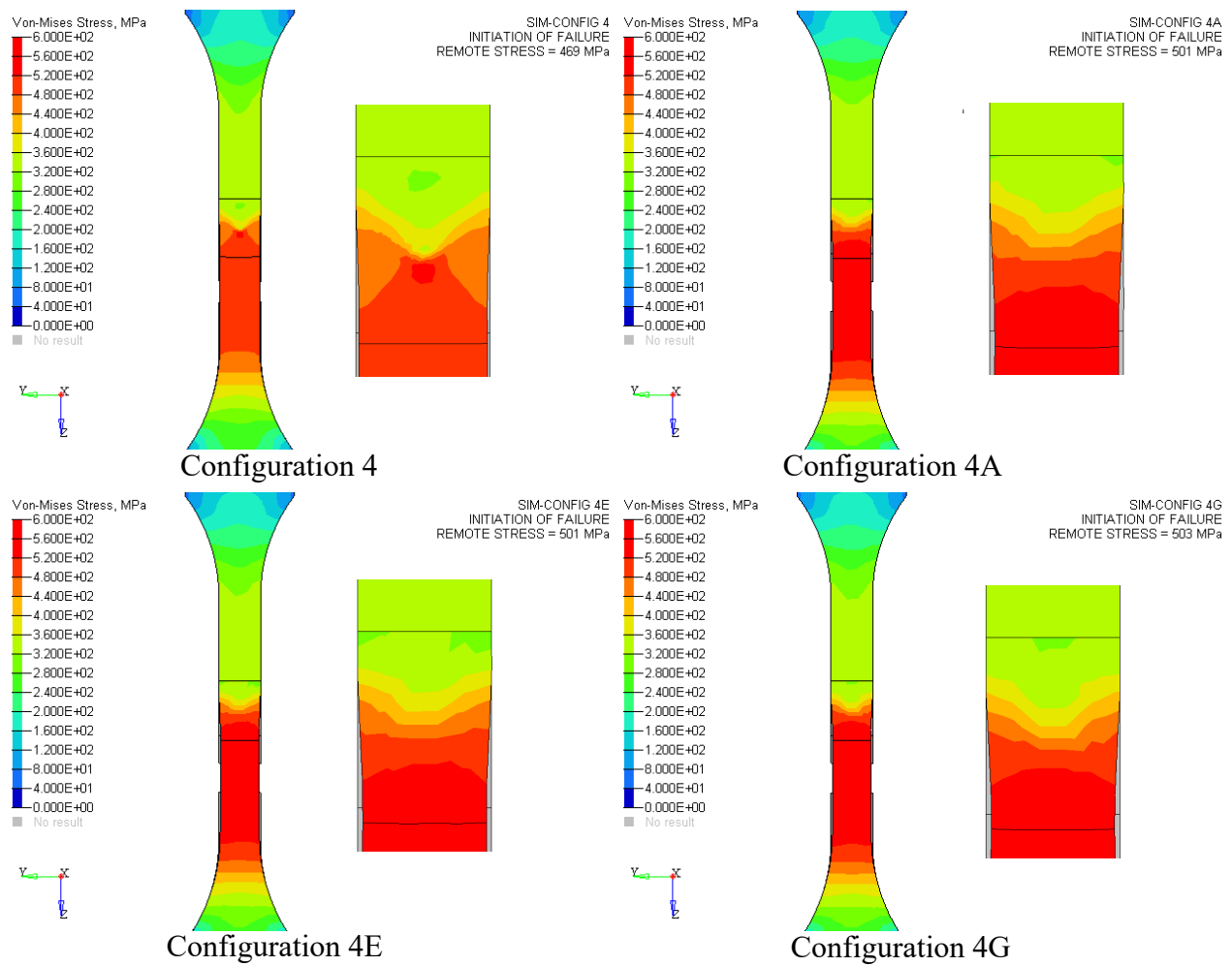


Figure 97. Von Mises stresses distribution in main part at initiation of failure for RBE SJMs without hole

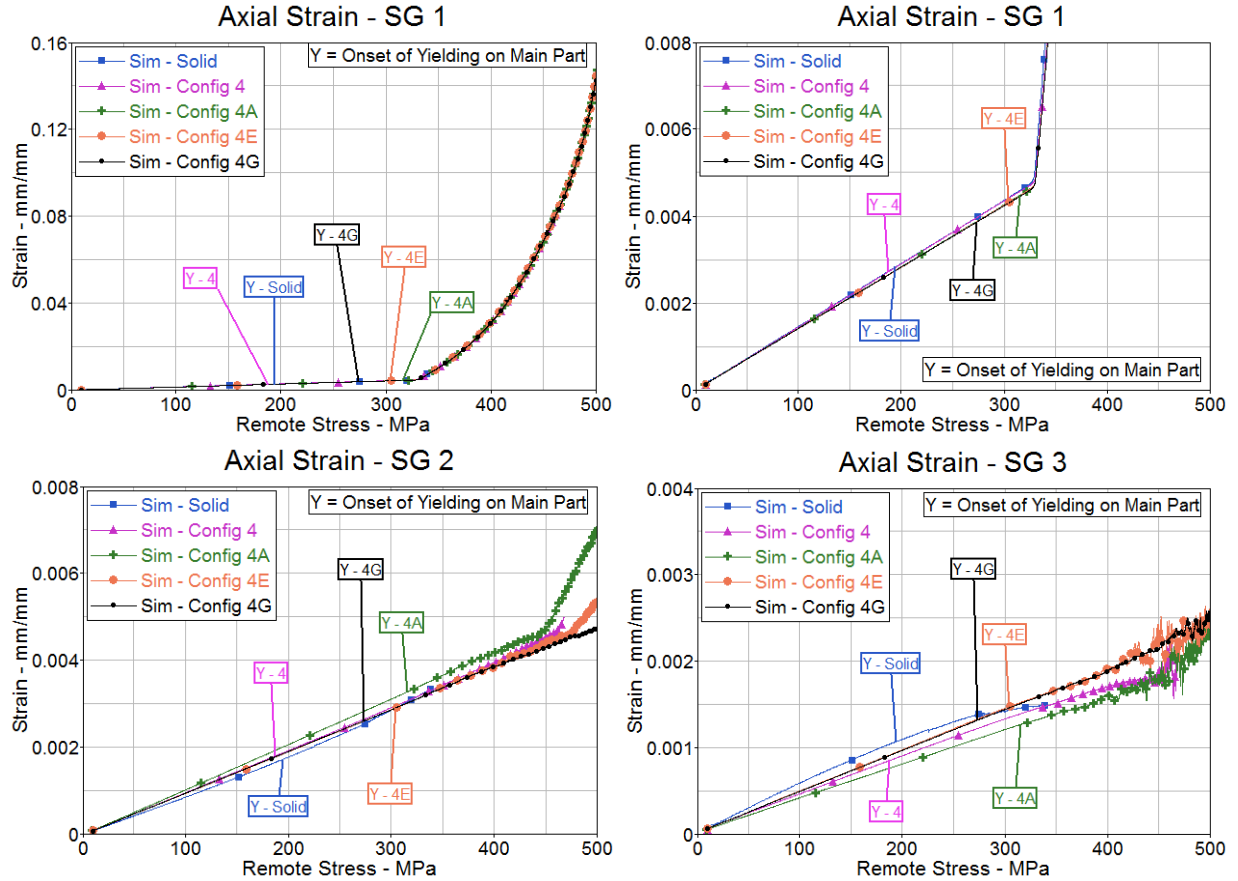


Figure 98. Axial strain introduced in the DJM and the RBE SJMs without hole

Strains at the SG locations shown in figure 23 are compared in figure 98. The top-right plot on figure 98 is a zoom-in of the SG 1 plot on top left. For all the models of this simplified technique, strains at the SG 1 location are in good correlation to the DJM. Strains at SG 2 and SG 3 deviate from the DJM. This can be attributed to the differences in LT for the different configurations.

4.2.2.4.3 Bolt Loads

The shear force on the bolt and the load recorded in the cross-section plane on the transfer part are compared to deduce the LT by the bolt and that transferred by friction as shown in figure 99. For the DJM, the load transferred by the bolt is approximately 75% on average compared to approximately 96% in the SJM configurations. The remaining load is transferred by friction.

Figure 100 shows the comparison of axial loads on the bolt. As expected, the initial axial load for all the models is approximately 2300 N, which is the preload applied to each model. Overall, the axial loads on all the configurations of this simplified technique are very similar. The correlation of axial loads to the DJM is not good.

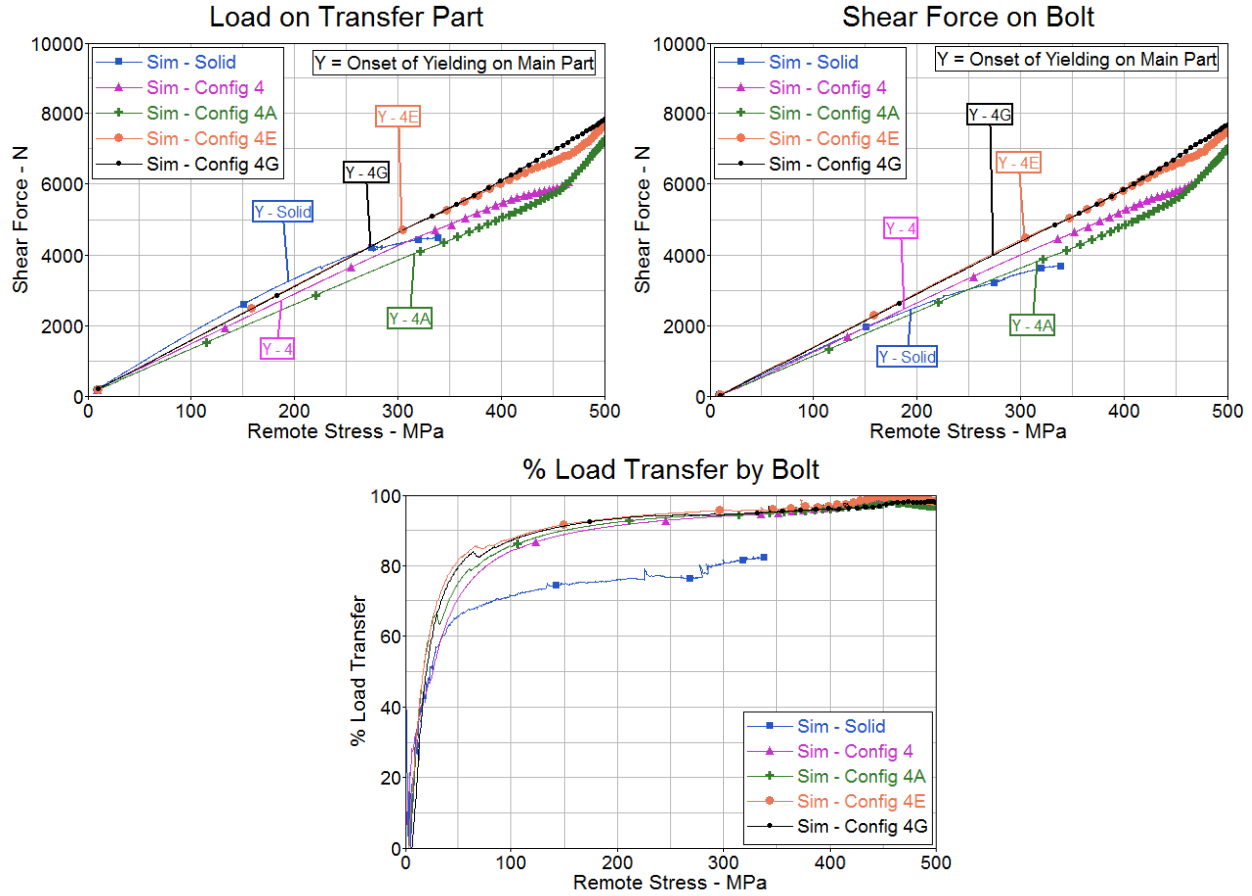


Figure 99. Comparison of LT by bolt for the DJM vs. the RBE SJMs without hole

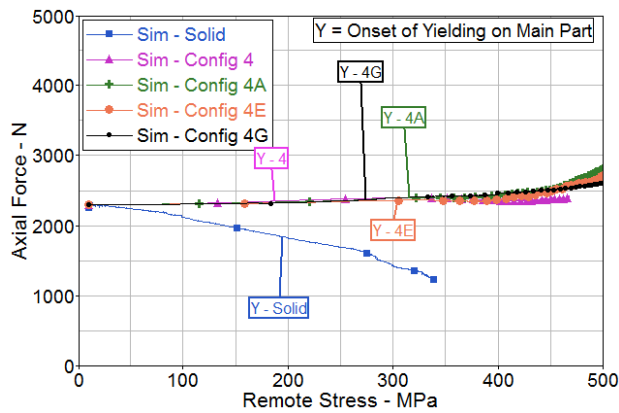


Figure 100. Comparison of axial force on bolt for the DJM and the RBE SJMs without hole

4.2.2.4.4 Energy

Configuration 4G most closely matched the DJM results and, therefore, was chosen as a representative for comparing the energies at failure; it is shown in figures 101–102. In comparison to the energy distribution in the DJM (total energy approximately 19 J), this SJM shows a total energy of approximately 210 J. The energy levels are higher for the SJM because the SJMs reach

failure at much higher remote stress, therefore introducing more energy into the structure. In addition, for this simplified model, the majority of the internal energy (approximately 155 J or 74%) is stored in the main part away from the patch area and 10% for the DJM. The main part patch stores 88% for the DJM and 24% for the SJM. This can be attributed to the shift in stress concentrations, toward the load introduction side, created by the simplified joint. Note that the energy distribution for Configuration 4G may not apply to the fine-mesh model like Configuration 4. Because this research was geared toward large FE models, fine-mesh models were not studied in detail.

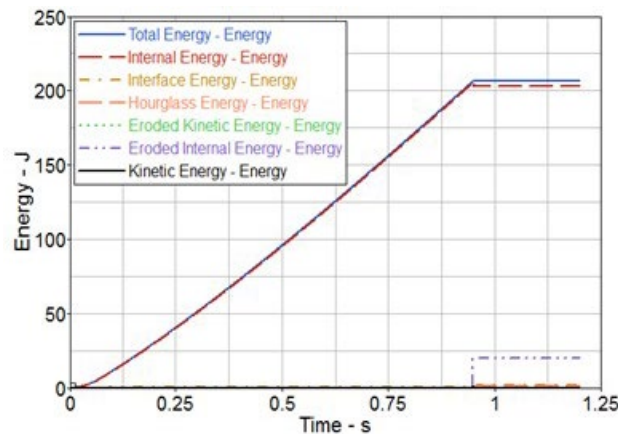


Figure 101. The energy levels in RBE SJM with no hole at QS loading for Configuration 4G

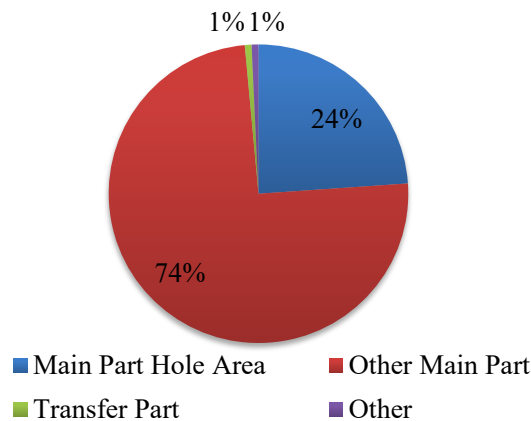


Figure 102. Energy levels in RBE SJM with no hole at QS loading for Configuration 4G

Based on figure 103, at low remote stress, the energy density on the main part and the transfer part of the DJM is much higher than the simplified configurations because of the presence of high clamp-load stresses in the DJM. Overall, the energy on the main part and the transfer part of this simplified technique configurations does not compare well with the DJM. This can be attributed to the shift in stress concentrations—and therefore plastic deformations—away from the patch area seen on this SJM.

The energy in the bolt shank, shown in figure 104, is higher in the simplified configurations compared to the DJM. This result is expected because the shear and axial force on the bolt shank of the SJMs is much higher than the DJM, as shown in figures 99–100.

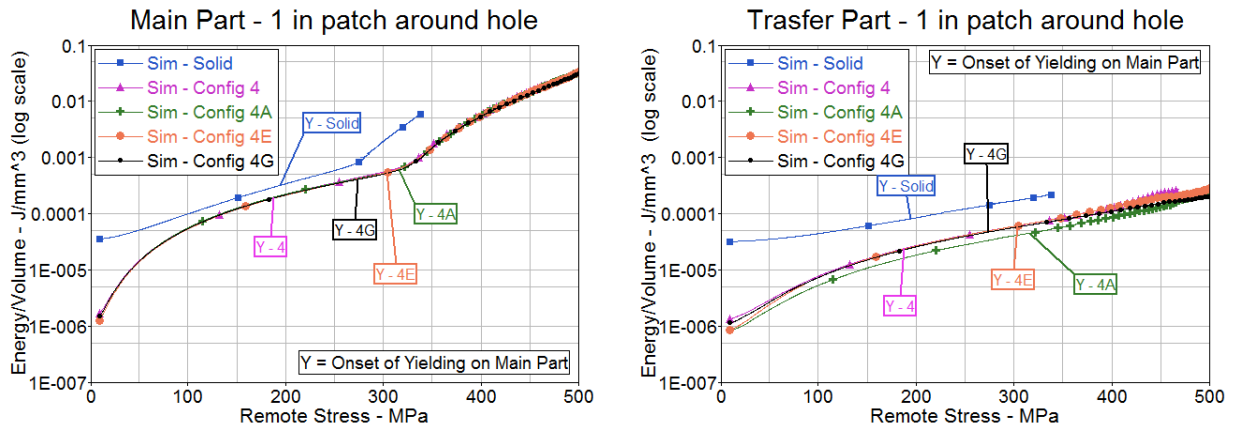


Figure 103. Strain energy per volume in patch areas for the DJM and the RBE SJMs without hole

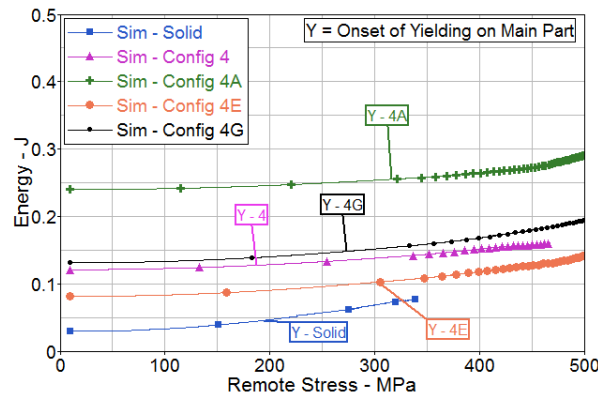


Figure 104. Comparison of bolt internal energy for the DJM and the RBE SJMs without hole

4.3 HIGH SPEED

4.3.1 DJM

Following a similar approach to the analysis of the quasi-static results, the DJM is evaluated for high-speed stroke rates.

4.3.1.1 LT Comparison

LT test results presented in section 2.3.3 exhibit an increase in the average LT under high stroke rates. In an attempt to capture the same trend from the numerical analysis, a material model was generated to accurately capture the strain-rate sensitivity for these aluminum specimens (see section 3.6.1 for detailed information).

The same DJM that was used for conducting simulations at quasi-static stroke rate was also used for simulations at stroke rates of 20 in./s, 50 in./s, and 100 in./s. Figure 105 shows a comparison of LT at different stroke rates for that particular FE model. Note that the LT results in figure 105 are calculated using equation 5, using strains. Contrary to what the testing data show, the numerical model results do not show an increase in the LT for higher stroke rates. Figure 106 shows the comparison between the testing data and the numerical analysis results for the 100 in./s configuration.

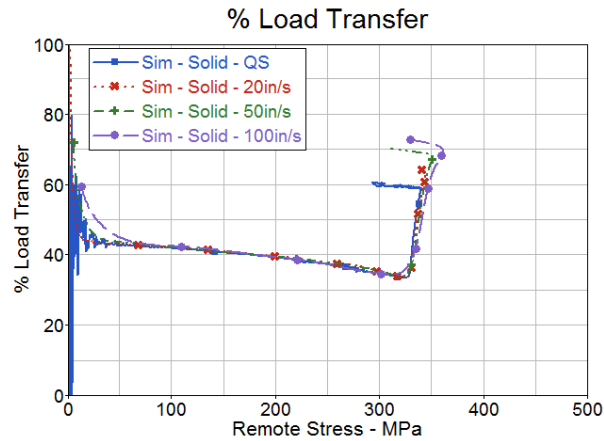


Figure 105. LT Comparison at different stroke rates for DJM

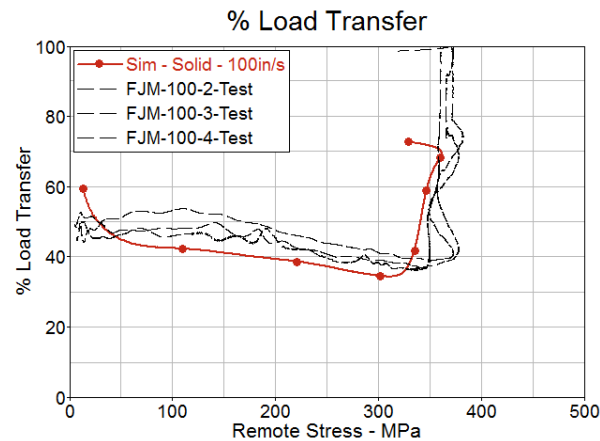


Figure 106. LT comparison of DJM vs. test results at 100 in./s

4.3.1.1.1 Inclusion of SL

To improve the FEA for high stroke rates, the SL model [43], used for testing, was included in the analysis. The setup for FEA with the SL system is shown in figure 107.

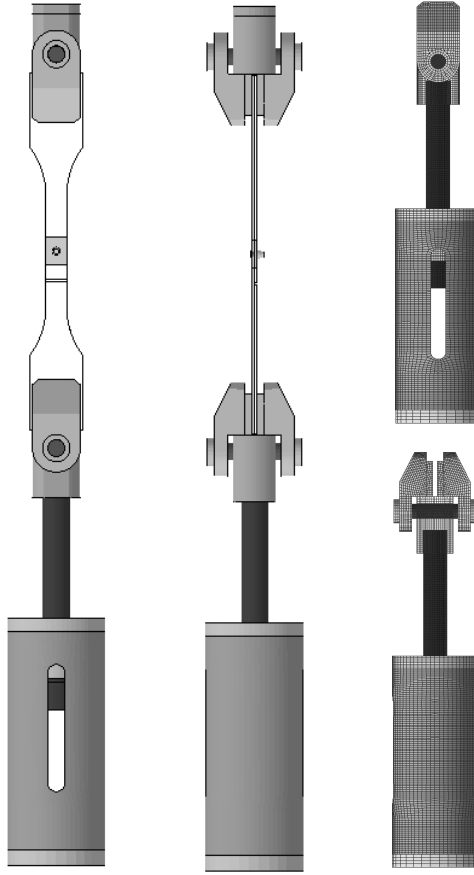


Figure 107. Solid FE model with SL

Figure 108 shows the LT with the addition of the SL system to the detailed DJM. An increase in the LT was captured for high stroke rates and can be seen by comparing figure 108 to figure 105. To understand how the SL system affected the LT, the load versus displacement is compared for the FEA with and without SL, for the 100 in./s stroke rate in figure 109. It is clear that when the SL was included in the FEA, a stiffer response was observed in the load introduction side of the specimen. The comparison to testing results at 100 in./s (see figure 110) indicates that with inclusion of the SL, the model captures the increase in LT and provides better correlation to test data. Comparison of simulation results to testing for other stroke rates is documented in appendix C.

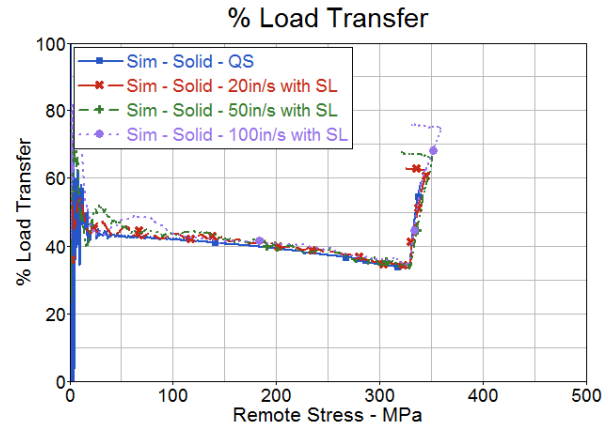


Figure 108. LT Comparison at different stroke rates for DJM using SL

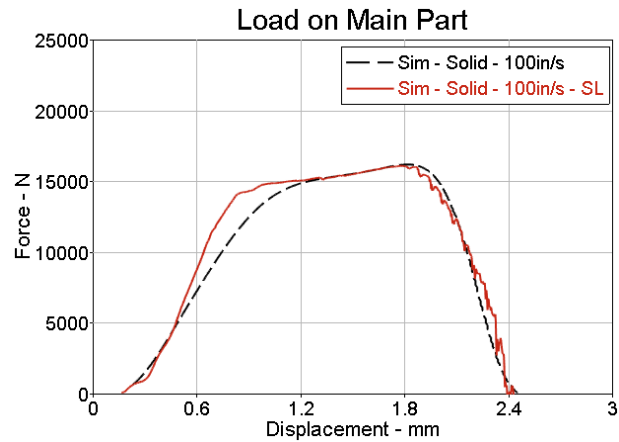


Figure 109. Load vs. displacement comparison of DJM with vs. without SL at 100 in./s stroke rate

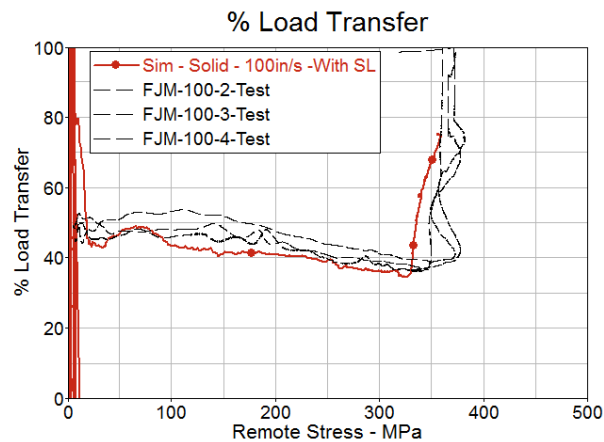


Figure 110. LT results comparison for solid bolt model with SL vs. test results at 100 in./s

4.3.1.1.2 SL Studies

In the SL used for testing, a washer was used in the system, as shown in figure 111. The washer was made out of rubber, which is known to absorb energy and to provide a damping effect. In an attempt to further improve the computational model, the washer at the interface of the loading pin and SL was modeled as rubber using LS-DYNA material model MAT_057. Some of the mechanical properties for the washer were obtained by performing a quasi-static compression test on the washer itself (30% compression), whereas some were arbitrarily chosen (typical properties).

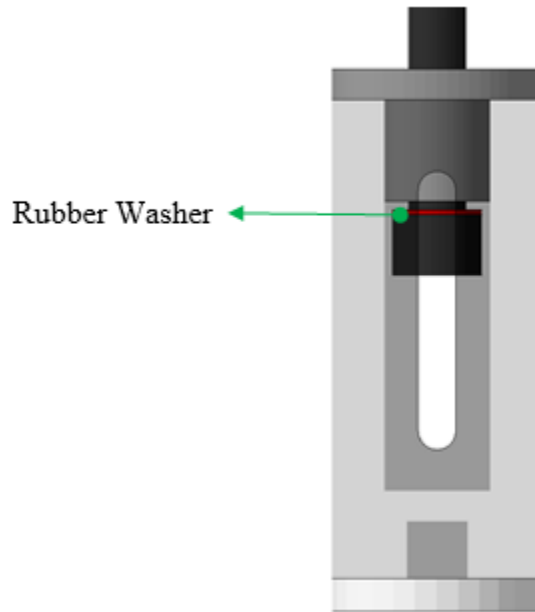


Figure 111. SL modeled with rubber washer

The results with the rubber washer were compared to the experimental results and the simulation results without the rubber, as shown in figure 112. The addition of the rubber results in a slight increase in the average LT, which results in a better correlation to the experimental data. Nevertheless, this model was not used for this study because of the large deformations on the rubber that resulted in numerical instabilities and the fact that the actual material properties for the rubber material were not available.

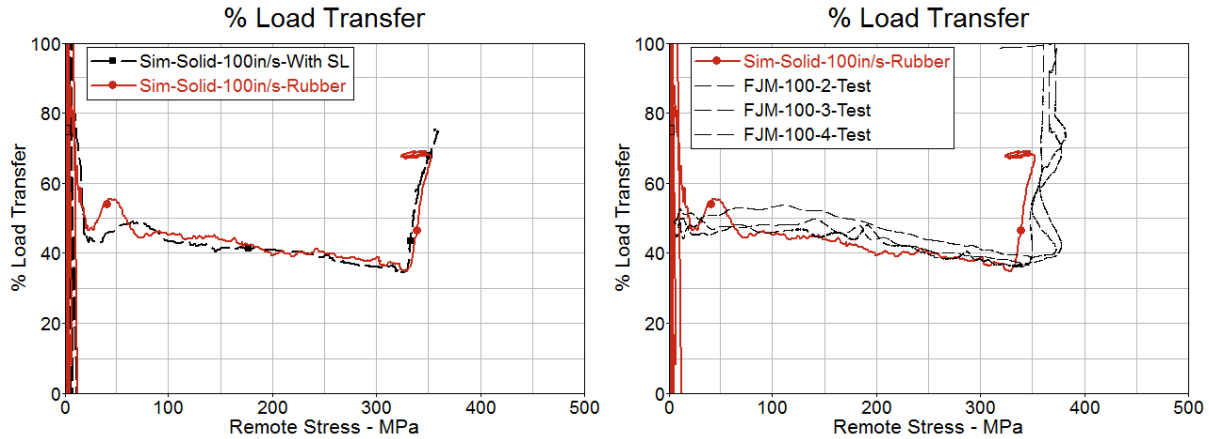


Figure 112. LT results for the SL model with rubber washer at 100 in./s

Figure 113 shows the results for another simulation in which the entire SL assembly was modeled as rigid material. The LT shows a significant peak at the beginning of the simulation as no energy is absorbed by the fixture, transferring all the load to the specimen. For obvious reasons, it was decided not to use this model. Nevertheless, it explains why important load-bearing parts cannot always be modeled as rigid.

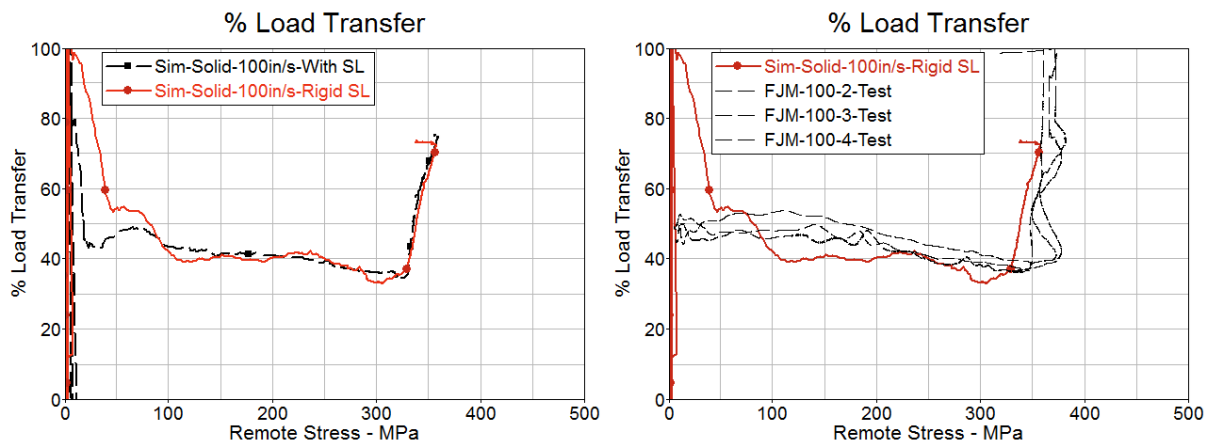


Figure 113. LT simulation results for DJM with rigid SL at 100 in./s

4.3.1.2 Stresses and Strains

The clamping stresses developed on the plates from the application of bolt preload were independent of the test's stroke rate because it was done prior to the tensile testing. Therefore, the clamping stress distribution is similar to the quasi-static case shown in figure 49. Figure 114 shows a comparison of von Mises stress contours of the main part just before failure initiation. As expected, stress concentrations were located around the hole net section for all the stroke rates. For higher stroke rates, the von Mises stress fields are also larger, showing the effect of higher strain rates. Figure 115 shows the von Mises stresses on the main part for different stroke rates. Higher stresses on the main part are observed away from the hole, for 100 in./s, when compared to other stroke rates.

The strains at the three SG locations are plotted in figure 116. The top-right plot on figure 116 is a zoom-in of the SG 1 plot on top left. The effect of strain rates is also observed at the SG 1 location. Higher strains are achieved for the 100 in./s stroke rate at SG 1 location, compared to other rates, when the specimen has reached failure.

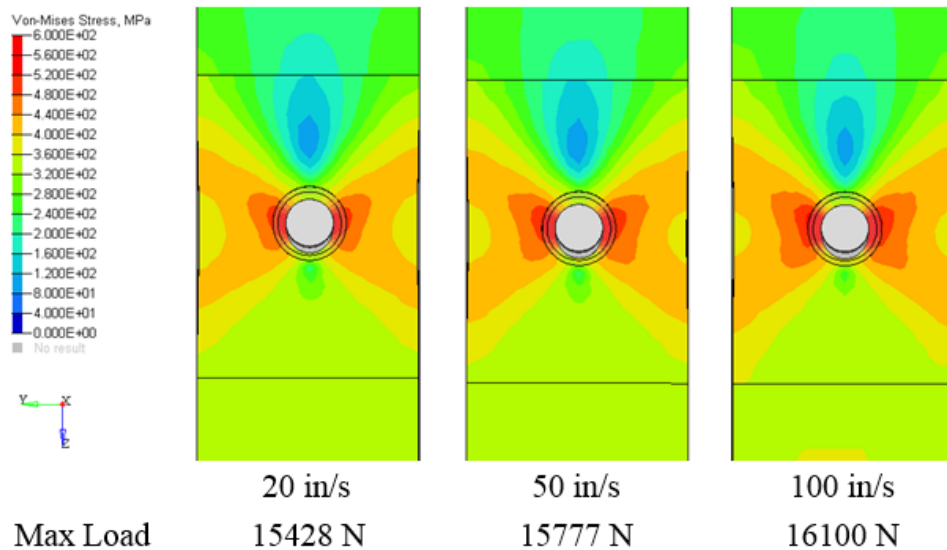


Figure 114. Von Mises stresses at failure initiation for DJM at different stroke rates

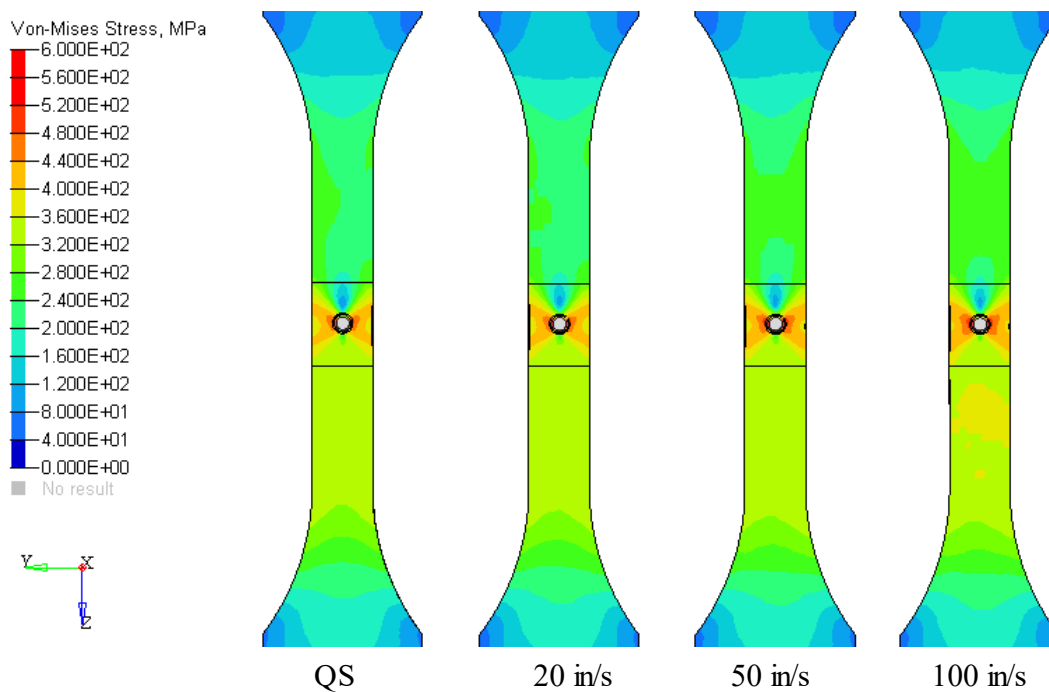


Figure 115. Von Mises stresses at failure initiation for DJM at different stroke rates—main part

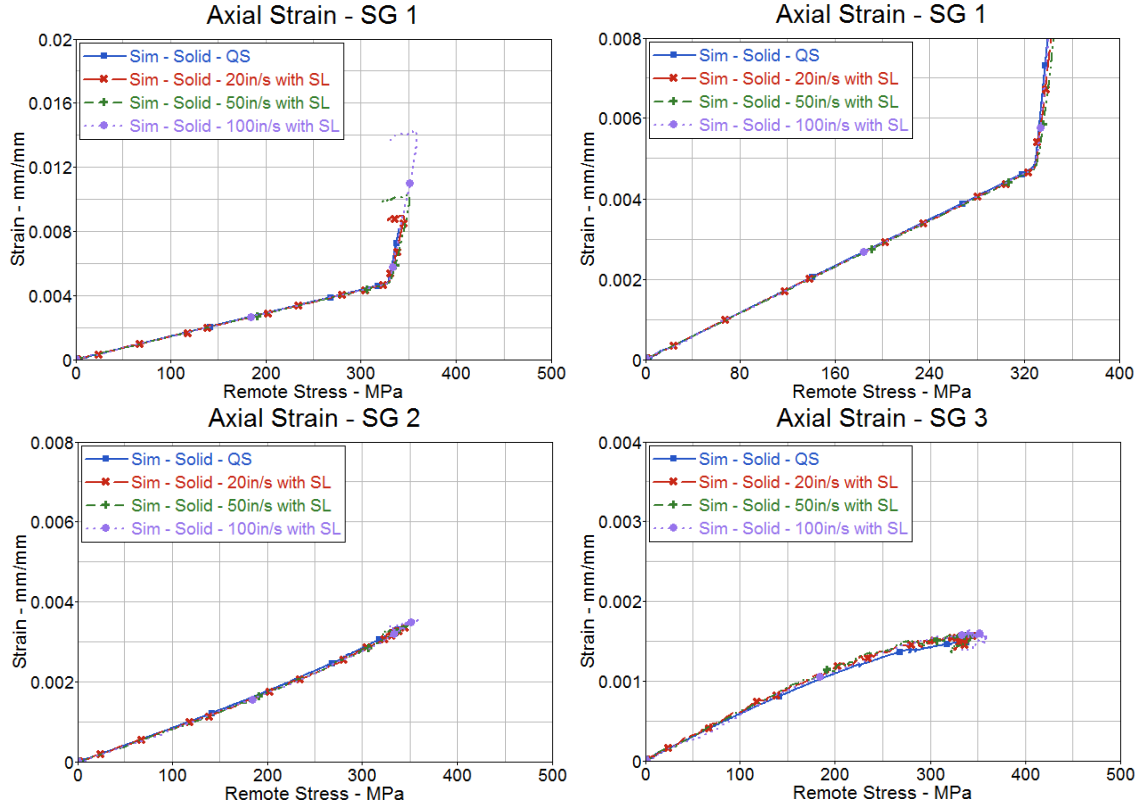


Figure 116. Strain comparison for DJM at high stroke rate simulations

The comparison of strains from the simulation versus test for a stroke rate of 100 in./s is presented in figure 117. The comparison for strains at other rates is presented in appendix D. Strains from the simulations do not reflect the oscillations seen on the test data. The sensitivity of the SL has been documented, and the differences seen in the strains could be due to the simplification of the SL model.

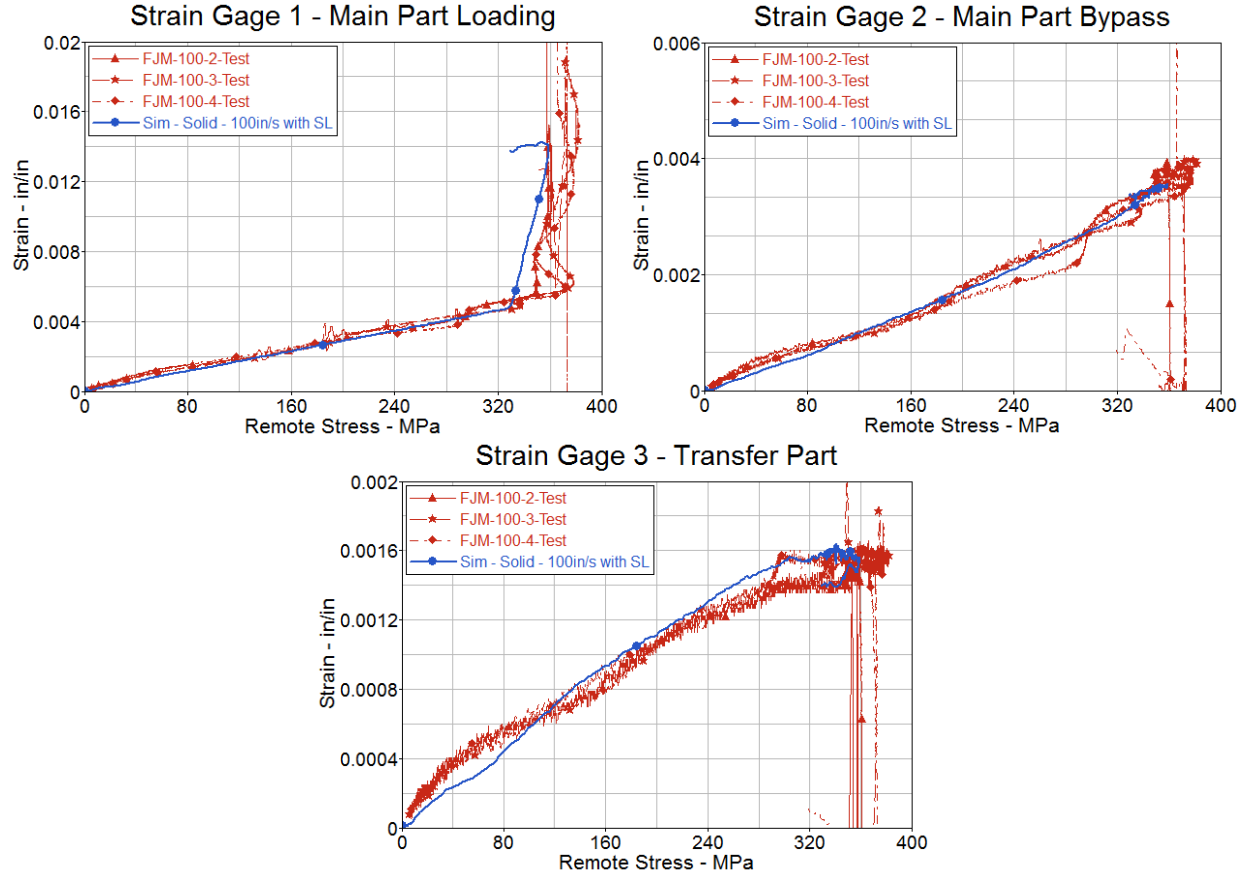


Figure 117. Strain comparison for DJM vs. test at 100 in./s stroke rate

4.3.1.2.1 Strain Rates

The axial strain rates at SG 1 location were plotted for both experimental and simulation data, as shown in figure 118. Higher strain rates were observed on the simulation models throughout the loading on the specimen. The strain rates became similar closer to failure of the specimen. Whereas the simulation is a more controllable scenario, it is difficult to control the stroke rates on an actual physical experiment, even while employing the SL.

Using the DJM results, axial strain rates were also obtained at the area around the hole where failure initiates, as shown in figure 119. As expected, the strain rates increased with stroke rates. Strain rates as high as 400 s^{-1} were obtained for a stroke rate of 100 in./s.

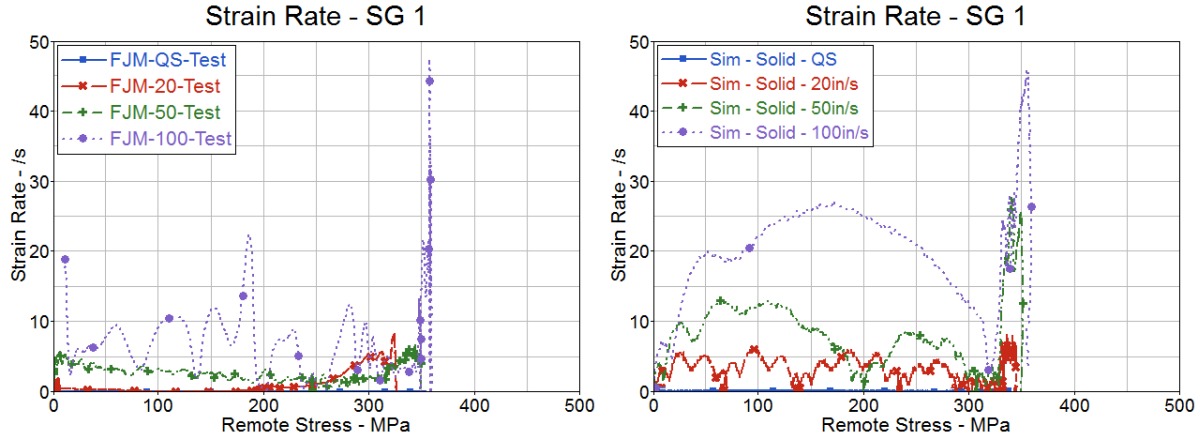


Figure 118. Strain-rate comparison of test and DJM for different stroke rates at SG 1 location

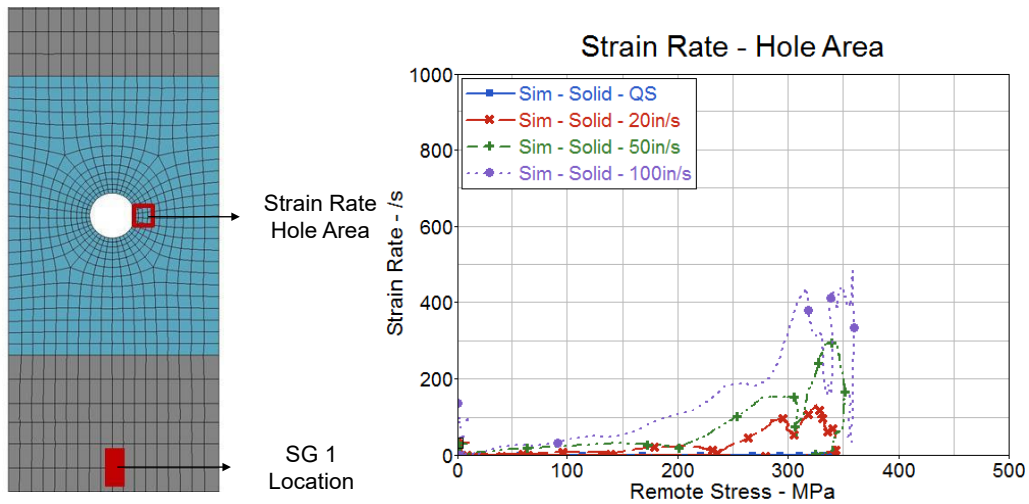


Figure 119. Strain-rate comparison on main part patch area of DJM at different stroke rates

4.3.1.3 Bolt Loads

As shown in figure 120, the axial loads for the higher stroke rates are similar to the quasi-static. This figure also shows that the shear force on the bolt for higher stroke rates has a more linear behavior compared to the quasi-static results.

Figure 120 also shows that higher loads are seen on the transfer part as the stroke rate increases. This last statement agrees with the previously presented percentage of LT plots. The percentage of LT by the bolt is lower and more linear compared to the quasi-static results. This indicates that a slightly higher percentage of load is transferred through contact for higher stroke rates.

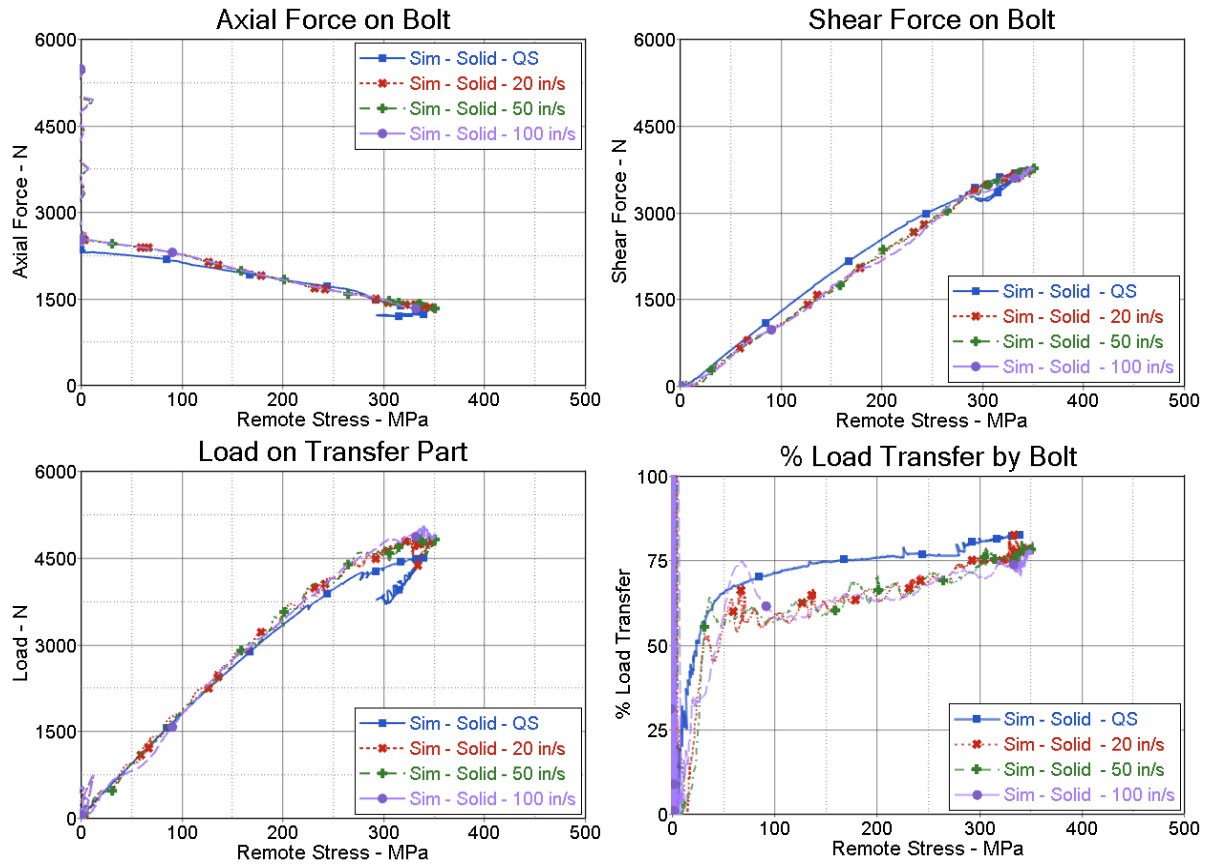


Figure 120. Comparison of bolt loads and LT by bolt for different stroke rates—DJMs

4.3.1.4 Energy

The energy levels from simulations for different stroke rates are shown in figure 121. For comparison purposes, the time is normalized by maximum simulation time, and energies from the SL are not included. Note that the majority of the total energy is translated into internal energy for all the models. The residual internal energy in the model increases with stroke rate, increasing as much as 52% from quasi-static to 100 in./s. The reason for this is attributed to higher stresses induced in the main part with increasing strain rate.

The distribution of internal energy of the DJM for the different stroke rates is presented as pie charts, shown in figure 122. The distribution of internal energy was split into the main part hole area, rest of the main part, transfer part, and the bolt and nut (referred to as other). The main part hole area, transfer part, and the bolt and nut can be summed to represent the fastener joint.

As a percentage distribution, there is a decrease of 10% of the internal energy in the joint when comparing quasi-static to 100 in./s stroke rate. Additionally, as the stroke rate was increased, the internal energy stored in the main part patch area (as a percentage) is lower. This could be due to higher stresses induced in the rest of the specimen, as shown in figure 115. It is also interesting to note that, as a percentage, the energy in the bolt and nut increases by 5%, and the energy on the main patch area decreases by 15%, when comparing quasi-static to 100 in./s stroke rate.

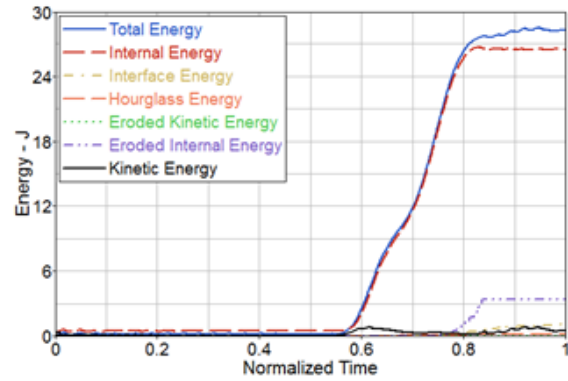
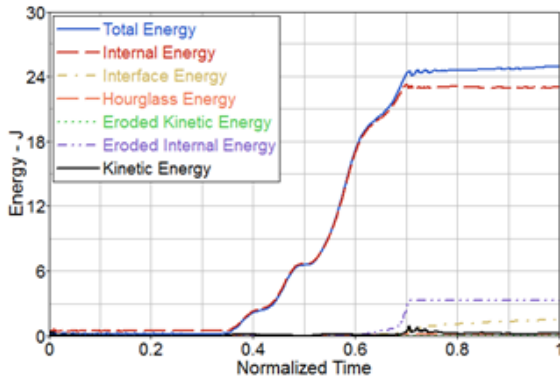
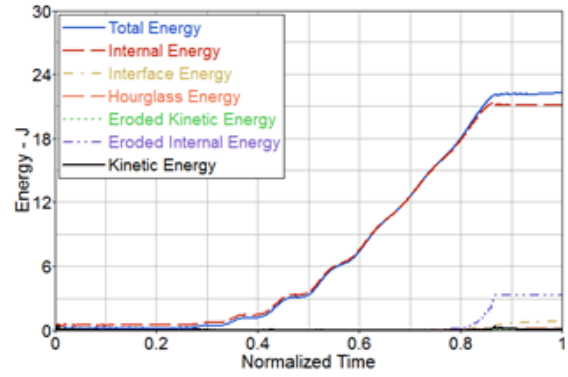
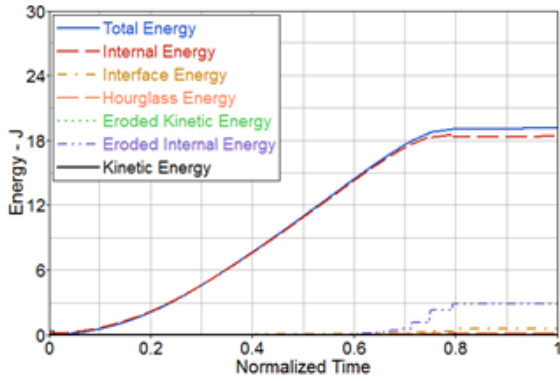


Figure 121. Total energy comparison for specimen at different stroke rates—DJM

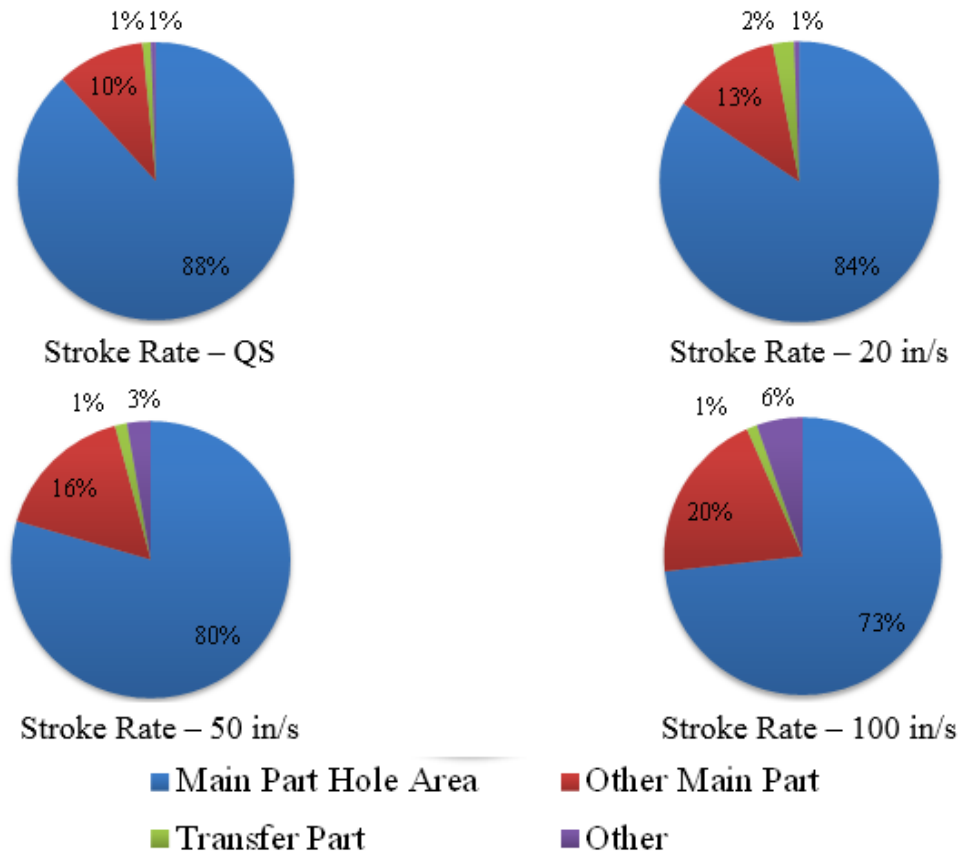


Figure 122. Internal energy comparison for specimen at different stroke rates—DJM

4.3.2 Mesh-Independent Spotweld Beam Model

Based on the prior results, it was concluded that the shell mesh-independent spot-weld beam model currently provides the most practical way for modeling joints on large-scale FE models. Therefore, the evaluation of high stroke rates for simplified joints was done using Configuration 2B, which was defined in section 3.1.2.2. The QS results for this model were presented in section 4.2.2.2.

4.3.2.1 LT Comparison

The LT for Configuration 2B for high stroke rates is compared to the DJM and is shown in figure 123. Because the SJMs use shell elements, the LT is evaluated using cross-section forces with equation 10. Note that the LT for DJM is also evaluated the same way in figure 123. The same approach was used for comparing all the SJMs at quasi-static rate (documented in section 4.2).

Based on figure 123, the LT for the simplified joint in Configuration 2B is similar to the DJM for all stroke rates. Differences are observed at higher remote stresses, but this can be attributed to the joining method used in Configuration 2B, which results in failure at much larger remote stress than the DJM. Overall, the SJM is able to capture the initial increase in LT as the stroke rate is increased.

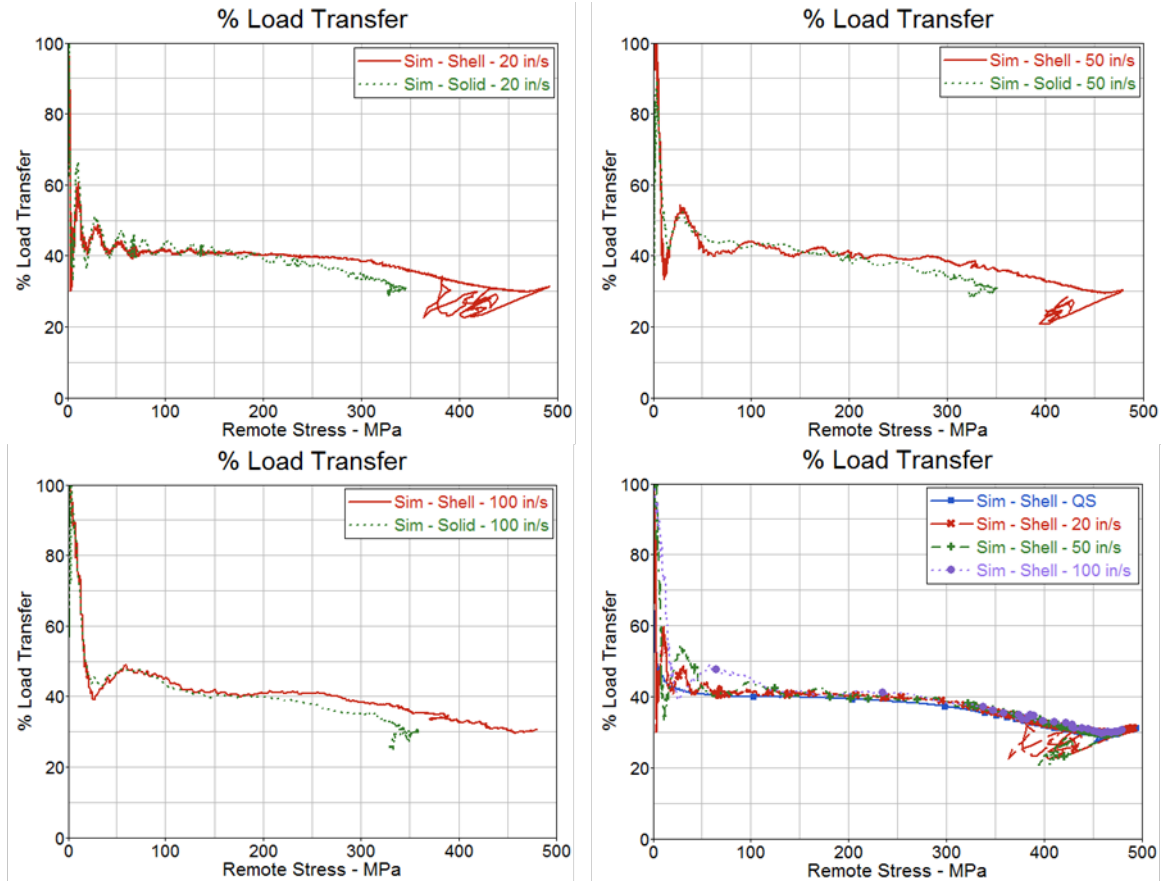


Figure 123. LT comparison at different stroke rates for DJM vs. mesh-independent spotweld SJM Configuration 2B

4.3.2.2 Stresses and Strains

As discussed earlier in section 4.1.2.3.2, the stresses are highly concentrated on the load introduction side of the main part, which is where necking and ultimate failure occur. Similar stress contours are observed under high-speed loading, as shown in figure 124. The levels of stress concentration and maximum loading also seem to slightly reduce for higher stroke rates.

Strains at different stroke rates for the SJM are compared in figure 125. The top right plot on figure 125 is a zoom-in view of SG 1 plot on the top left. Overall, the strains are similar for all the stroke rates, with minor differences at SG 2 and 3. For increasing stroke rates, the final strains at the gauge locations were decreasing as compared to the DJM, in which the strains at the gauge locations increase with stroke rate. The absence of a fastener hole results in a different loading mechanism, which could be causing such behavior. The magnitude of strains at the gauge locations were still much higher for SJMs due to the large load required for failure. Strains for 100 in./s stroke rate are compared to the DJM in figure 126. The strains are similar at all gauge locations for lower remote stresses, but because the SJM does not reach failure until much higher remote stress, the strains begin to differ after approximately 250 MPa of remote stress.

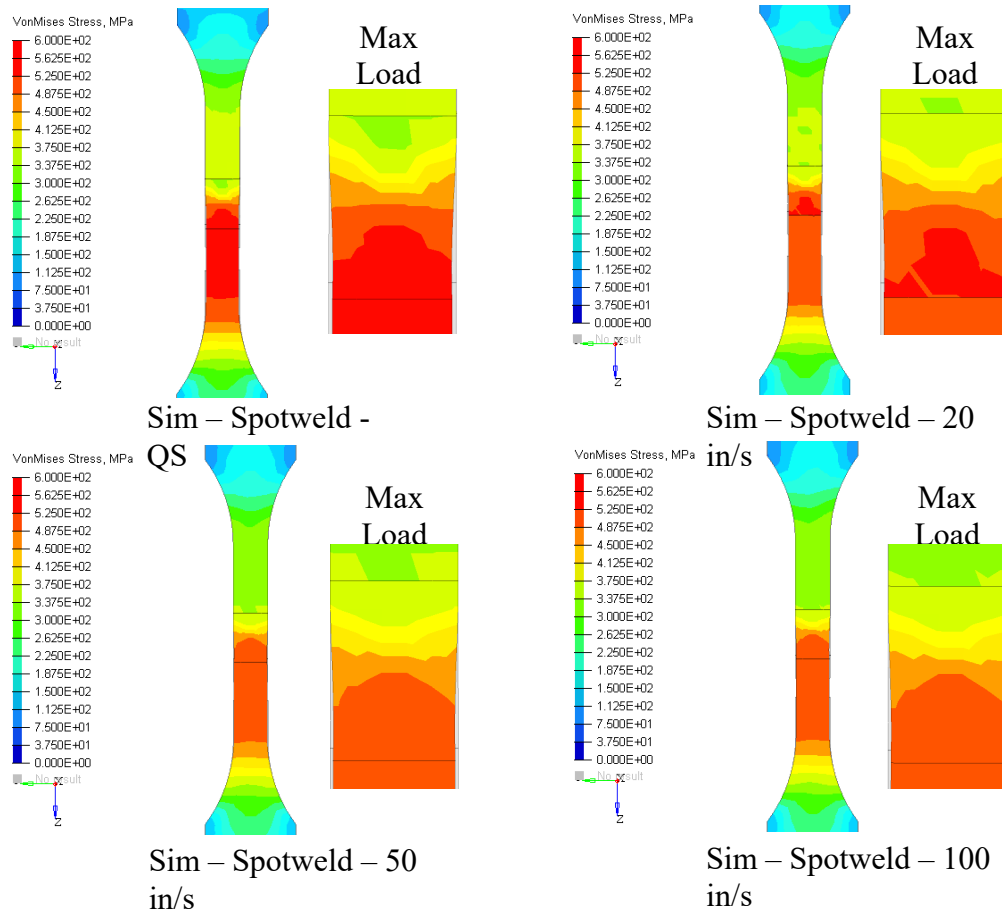


Figure 124. Stress distribution of main part and maximum load for mesh-independent spotweld beam model Configuration 2B at different stroke rates

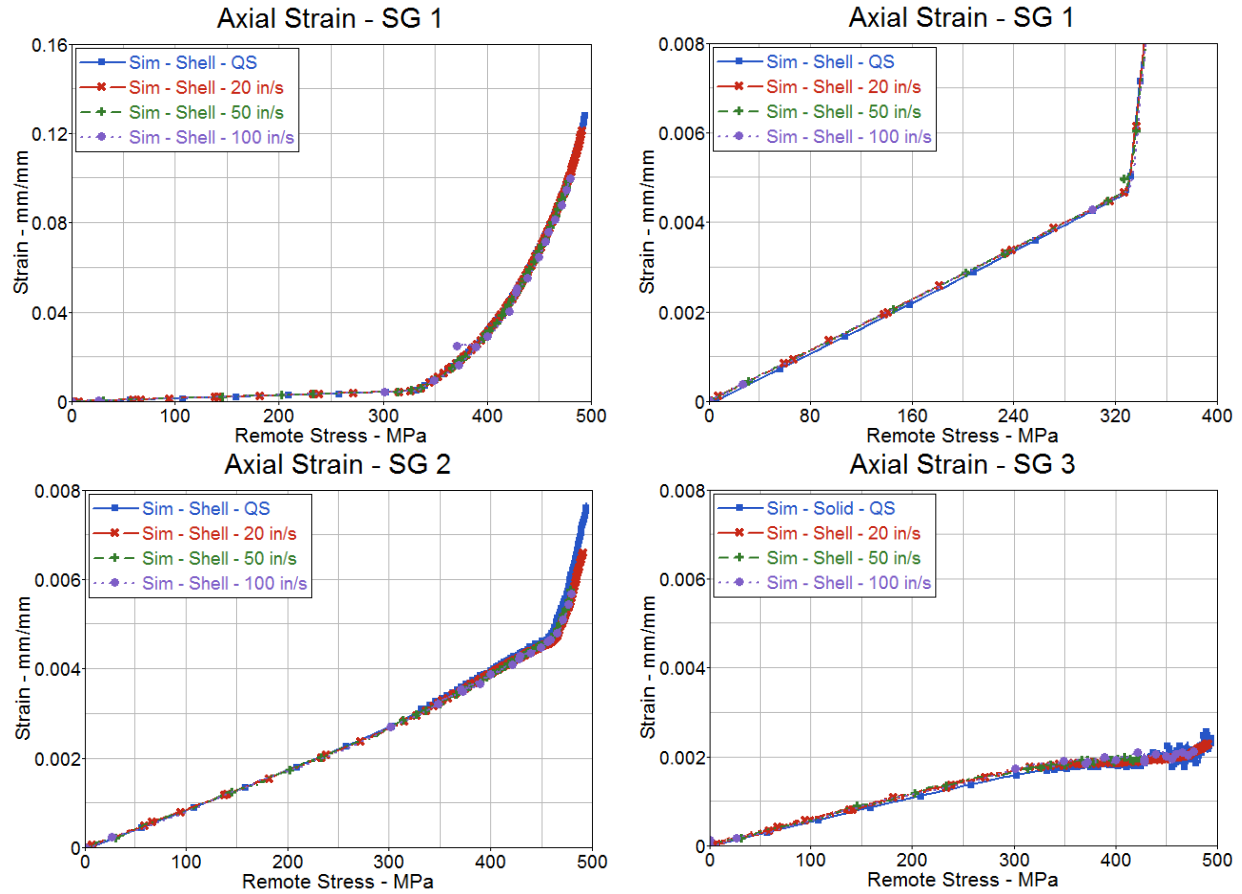


Figure 125. Strain comparison for high stroke rates for mesh-independent spotweld beam model Configuration 2B

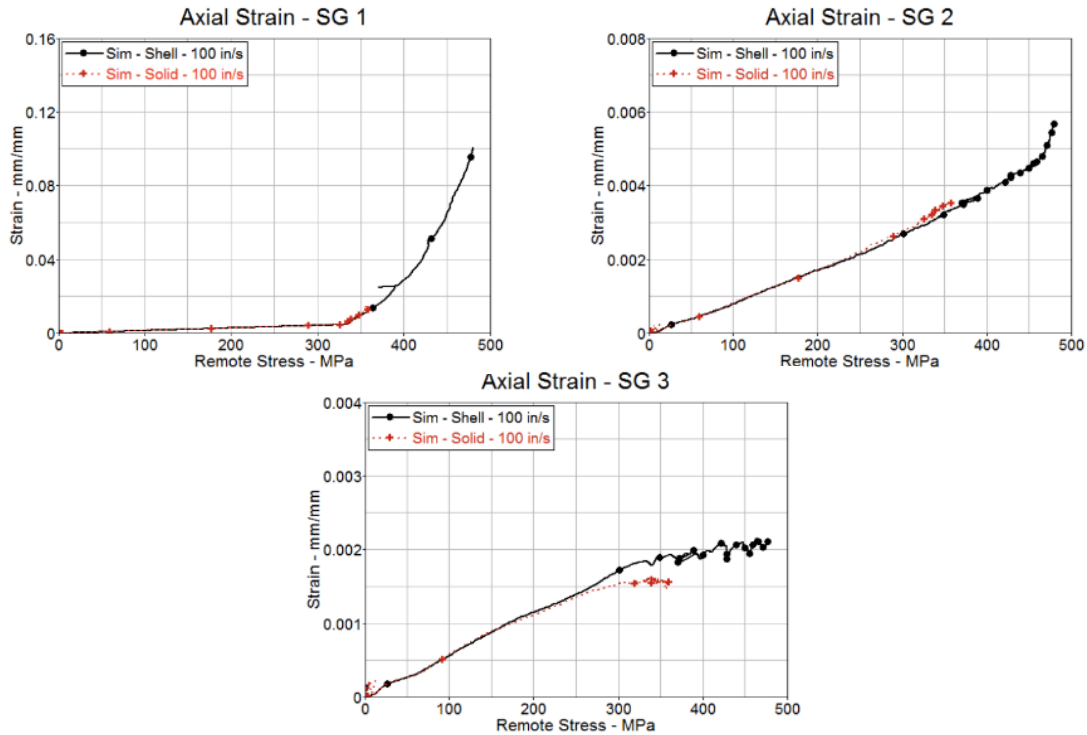


Figure 126. Strain comparison of the mesh-independent spotweld beam model Configuration 2B to the DJM at 100 in./s stroke rate

4.3.2.2.1 Strain Rates

The strain rates at the SG 1 location are compared to the DJM in figure 127. The strain rates are similar for the DJM and SJMs for different rates, up until remote stress of 200 MPa. When plastic deformations begin, the strain rates differ.

The strain rates near the fastener are a lot lower for the mesh independent spotweld beam model 2B compared to the DJM, as shown in figure 128. The loading mechanism is different for the SJMs because of the absence of a fastener hole, and as a result the stress concentrations and the strain distribution are also different.

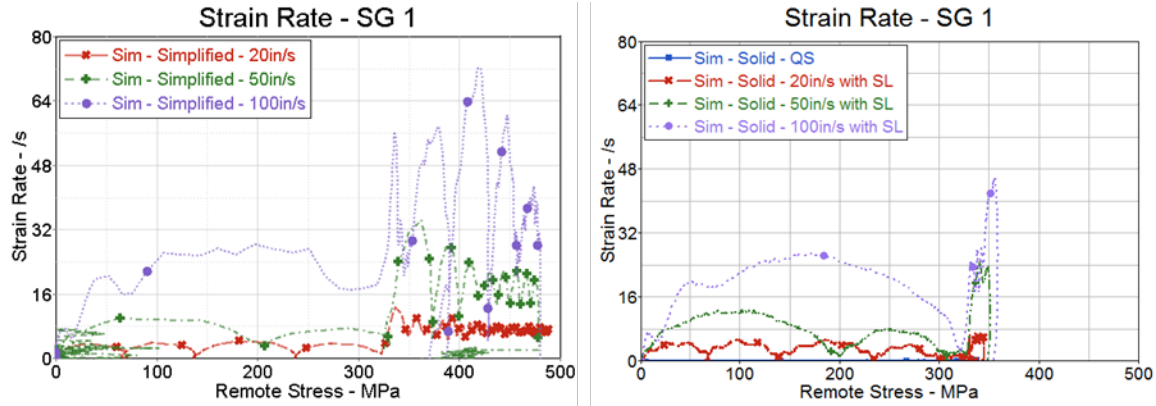


Figure 127. Strain-rate comparison for mesh-independent spotweld beam model 2B vs. DJM for high stroke rates at SG 1 location

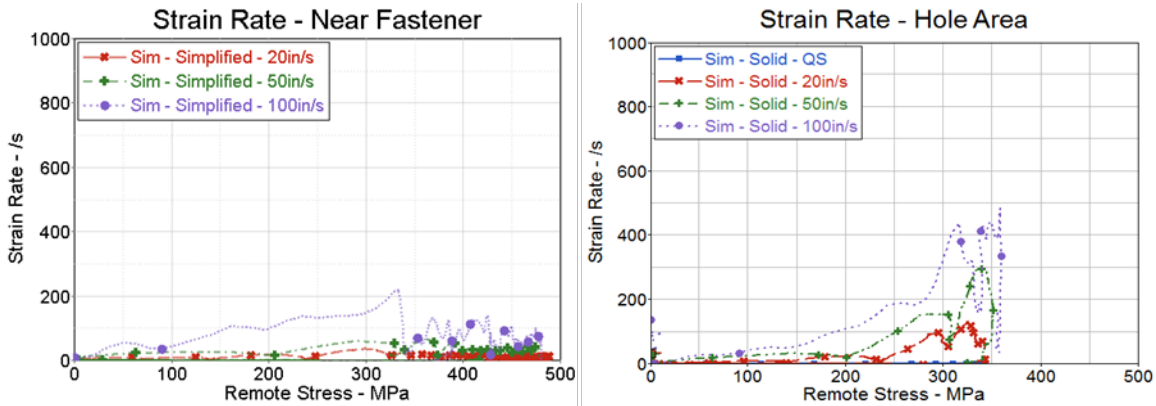


Figure 128. Strain-rate comparison for mesh-independent spotweld beam model 2B vs. DJM for high stroke rates near fastener

4.3.2.3 Bolt Loads

A comparison of the bolt loads of the mesh-independent spotweld beam model 2B are shown in figure 129. The axial forces on the bolt start at approximately 2300 N for all cases, as that was the applied preload. A larger drop of the axial force was observed for the QS test compared to higher stroke rates. The shear force exhibited on the bolt was very similar for all stroke rates, but the load on transfer part differed slightly. As a result, the LT by the bolt was also slightly higher for QS compared to the higher stroke rates. Overall, the LT by the bolt versus friction shows similar trends, as the DJM shows in figure 120, in which the QS exhibits higher LT by the bolt compared to higher stroke rates.

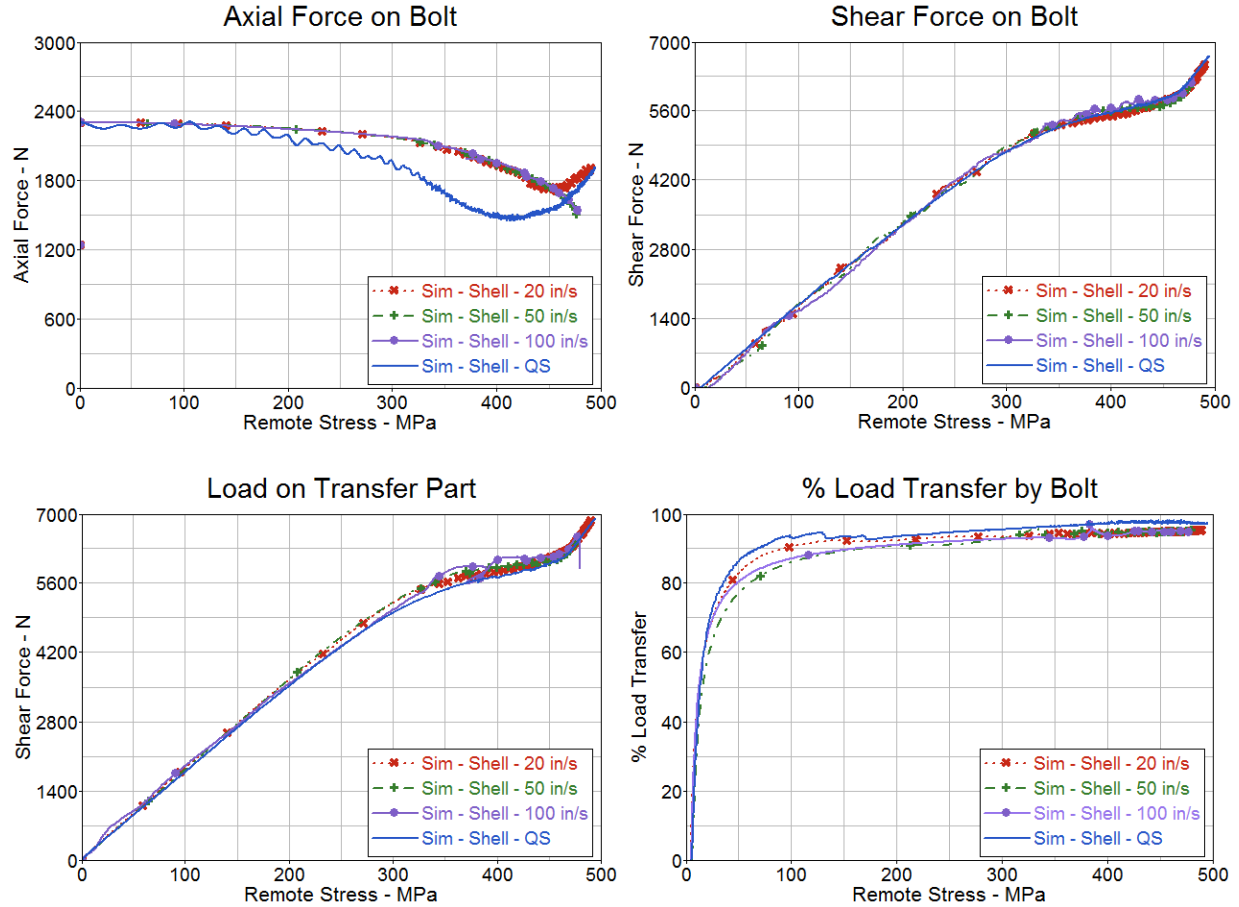


Figure 129. Comparison of bolt loads of the mesh-independent spotweld beam model 2B at different stroke rates

4.3.2.4 Energy

The energy levels from simulations for different stroke rates are shown in figure 130. For comparison purposes, the time is normalized by maximum simulation time, and energies from the SL are not included. Note that the majority of the total energy is translated into internal energy for all models. The residual internal energy in SJMs decreases with stroke rate, decreasing as much as 21% from quasi-static to 100 in./s.

The distribution of internal energy in the simplified model, for different stroke rates, is shown in pie charts in figure 131. The distribution of internal energy was split into main part hole area, rest of the main part, transfer part, and the bolt and nut (other). Note that as the stroke rate increased, the percentage of internal energy stored in the main patch area also increased. The main patch area, the transfer patch area, and the bolt and nut can be summed to represent the fastener joint. There is an increase of 5% internal energy in the joint when comparing quasi-static to the 100 in./s stroke rate. The percentage energy on the bolt remains the same for all the stroke rates.

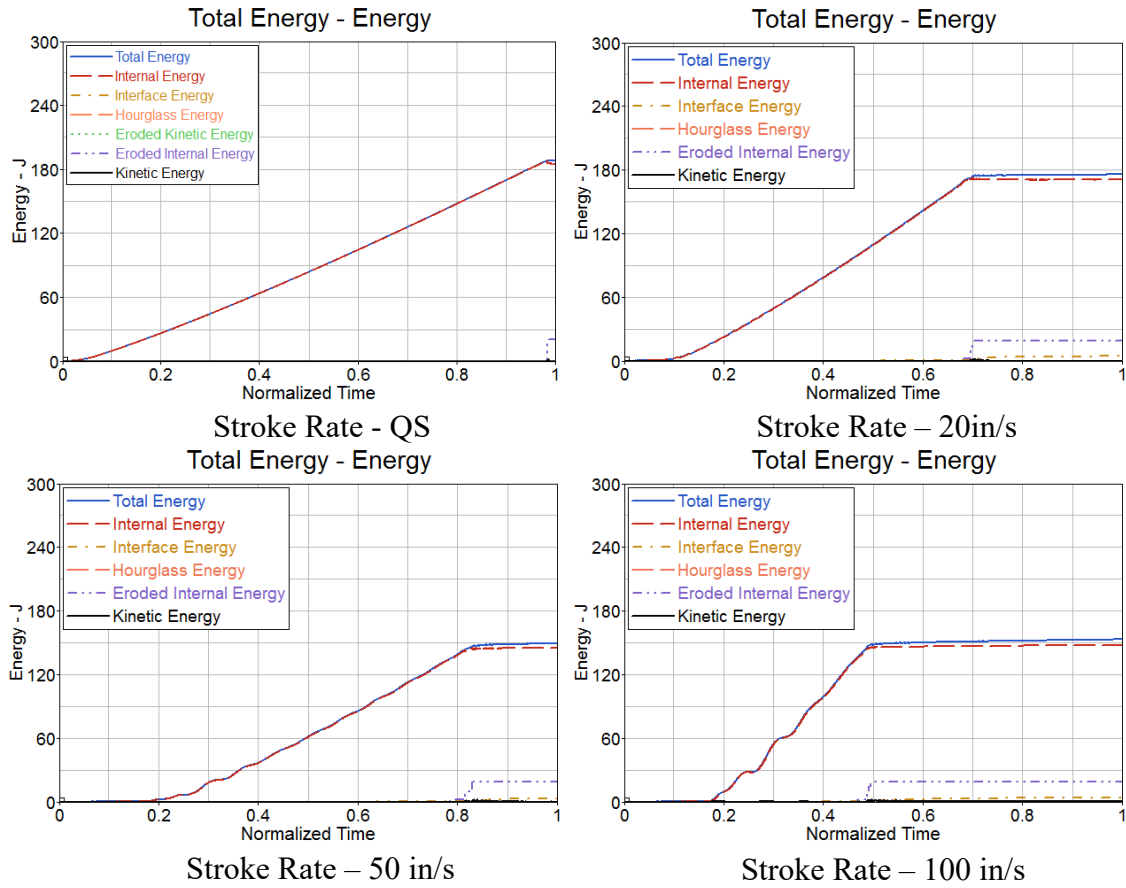


Figure 130. Energy distribution for different rates on specimen using—mesh-independent spotweld beam model Configuration 2B

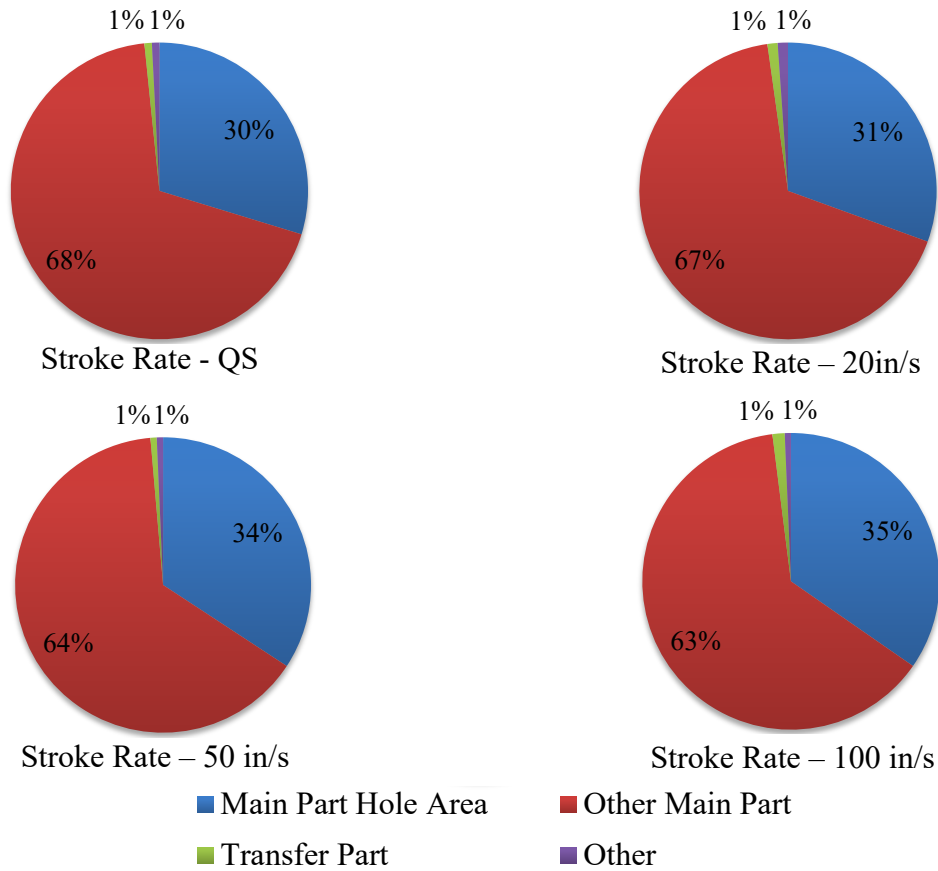


Figure 131. Internal energy comparison for different stroke rates on specimen using mesh-independent spotweld beam model Configuration 2B

In comparison to the DJM, the energies behave the opposite when stroke rate is increased from QS to 100 in./s. To better understand this, it is first important to understand the joining mechanism for the two, as shown in figure 132. The two red circles on the SJM joint represent the nodes that are constrained. The DJM consists of a fastener hole and a detailed fastener model. Figure 133 shows the plastic strain distribution on the main part, at the initiation of failure, for different stroke rates on the DJM. Note that as the stroke rate is increased, more plastic deformations are observed. Because of the presence of the fastener hole, the edge of the hole has higher stress concentrations and, therefore, sees higher strain rates compared to other areas of the specimen. This is shown in section 4.3.1.2.1. As a result, the authors believe that because of the use of strain-rate-sensitive material properties, the areas experiencing high strain rates can take higher loads, therefore allowing more deformations to occur in other areas before failure is induced. As a result, a higher load is required to reach failure and, therefore, higher energies are observed as the stroke rate is increased.

Figure 134 shows the plastic strain distribution on the main part, at the initiation of failure, for different stroke rates on the simplified model. Note that as the stroke rate is increased, less plastic deformations are observed. It appears that for the QS case on the simplified model, there is more time to distribute the loading and therefore several elements see higher plastic strains, whereas in the case of 100 in./s as the failure is initiated before such distribution. The authors believe that

because of the large mesh size and constraint mechanism used, the elements are not able to distribute the load under higher stroke rates and as a result the failure for SJMs occur at lower loads when comparing QS to 100 in./s stroke rates.

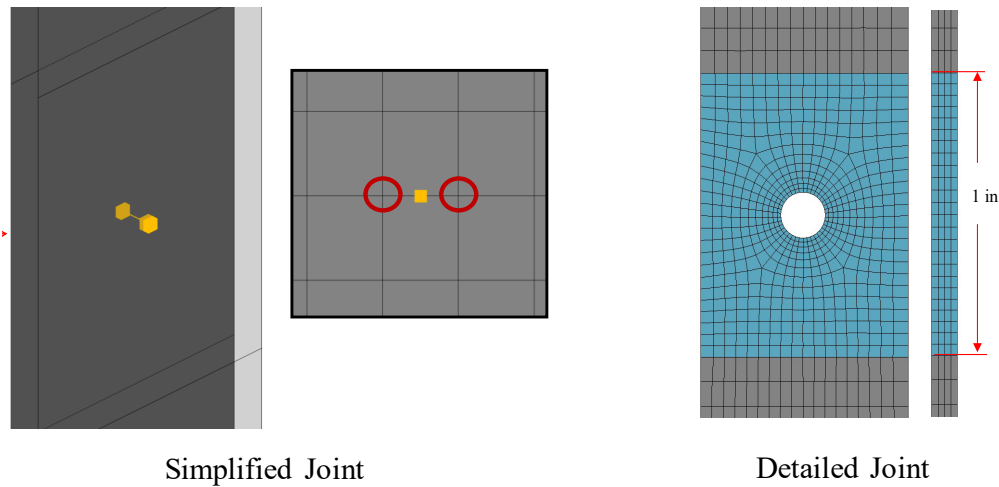


Figure 132. Joining mechanism showing two nodes constrained in the mesh-independent spotweld beam model Configuration 2B and solid elements in DJM

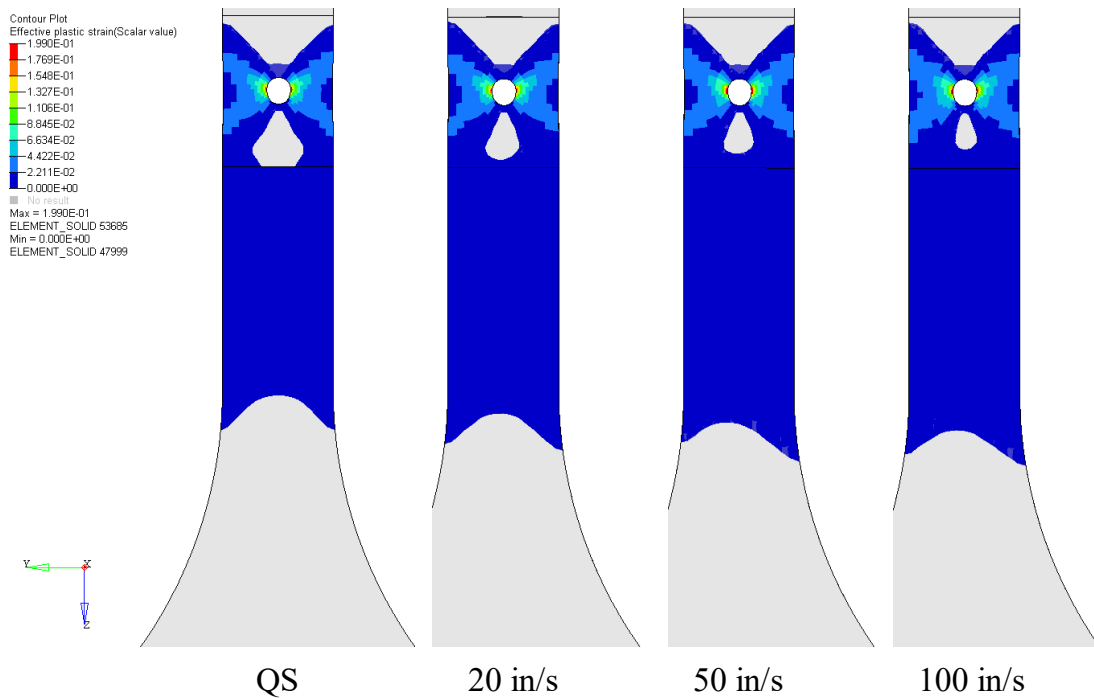


Figure 133. Plastic strain distribution at initiation of failure on main part of DJM for different stroke rates

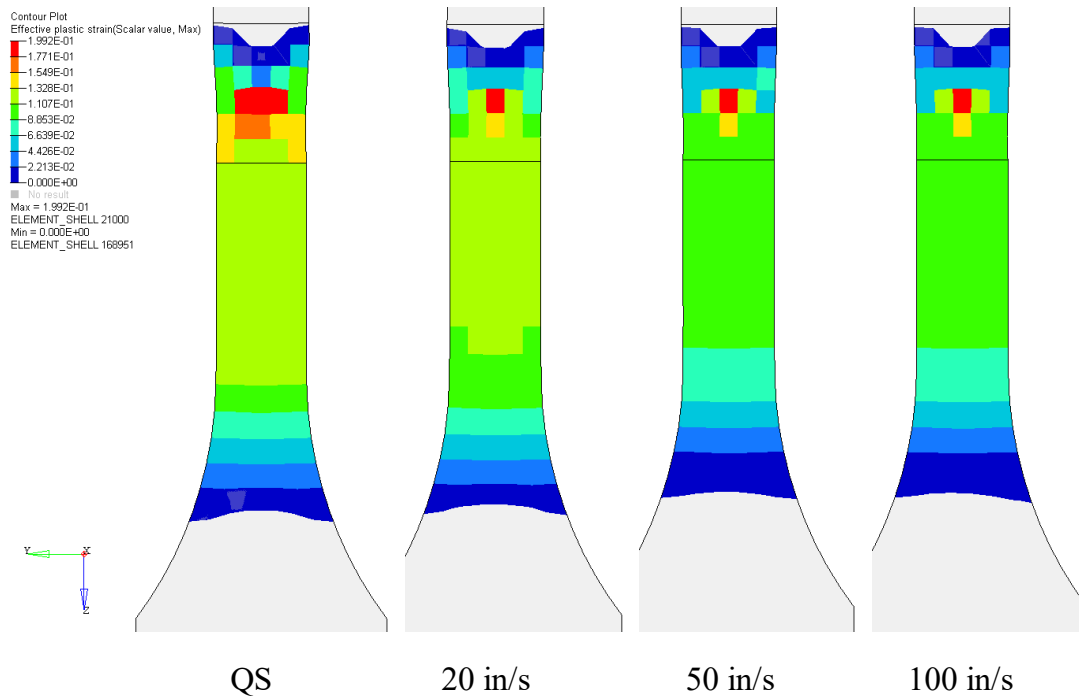


Figure 134. Plastic strain distribution at initiation of failure on main part of mesh-independent spotweld beam model Configuration 2B for different stroke rates

5. RESULTS AND DISCUSSION

In this study, simplified joint numerical modeling methods were explored and analyzed in detail to support crashworthiness computational analysis of large structural models. At first, single-shear lap joint specimens were physically tested at stroke rates varying from QS to 100 in./s to characterize the load transferred. The specimen assembly was comprised of the main part, transfer part, and the bolt. The main part and transfer part were manufactured using aluminum 2024-T3, and the fastener was a HI-LOK™ 18. Details of the specimen geometry are provided in section 1.1.1. To ensure that desired stroke rates were achieved before loading of the specimen, a SL system was used as a part of the test fixture.

After testing, an DJM was generated that was used to further investigate stress distributions, fastener loads, strain-rate effects, and energy distribution in the test assembly, which would not be possible by traditional experimental techniques. This model was also used to validate the FEM methods by comparing the numerical results to experimental data. The DJM was used as a baseline to evaluate the performance of different simplified techniques at the QS stroke rate. Finally, the simplified technique with the best overall performance during the QS evaluation was also used for further comparisons at higher stroke rates.

5.1 EXPERIMENTAL TESTING

Three different experimental tests were performed for this study:

1. Test for preload characterization
2. Test for characterization of material properties
3. The single-shear fastener joint test to characterize the LT at different stroke rates

The test setup, procedure used, and results are published in detail in section 2.

A preload versus torque curve was generated and used to identify the preload on the specimen prior to testing. On average, the preload value on the specimens was 2300 N, as detailed in table 1. The aluminum used for manufacturing the main part and transfer part was also tested. Five specimens were tested at QS speed and the coefficient of variation for the extracted properties was within 10%, which indicated good conformance of the test data. The material data extracted from these tests are summarized in section 2.2. The material data at high stroke rates were available from [43].

The setup for the LT tests was complex and involved many different components, such as the SL system and the ABF. Tests were performed at different stroke rates (QS, 20 in./s, 50 in./s and 100 in./s). It was found that the percentage of LT for tests performed at QS remained at approximately 40%. An increase in the percentage of LT was observed for higher stroke rates of up to 10% for 100 in./s. The failure observed for all the specimens was a tear-out of the plate material at the net section.

5.2 VALIDATION OF FE MODELING METHODS

An DJM was created to validate the FEM methods and to use as a baseline for comparison to simplified joint FE models. The specimen assembly of the DJM consists of 21,980 solid elements, with a minimum element size of 0.206 mm. As noted, the preload and material properties were extracted from the experiments and applied to the FE model.

Overall, a good level of correlation between the DJM results and the experimental data at QS speed was achieved (see figure 48). At first, the numerical analyses conducted at high stroke rates did not result in an increase of LT as evidenced in the experiments. The addition of the SL system to the FE model showed a better comparison of LT between the numerical analysis and the experiment, as shown in figures 108 and 110. With this, the FEM methods were considered validated and used to compare to other SJMs, both at quasi-static and high-stroke rates.

5.3 JOINT PERFORMANCE AT QUASI-STATIC STROKE RATES - SJMS VERSUS DJM

Currently, for crashworthiness analysis, simplified joint modeling is important because it is the only feasible way to account for all the connections associated with large numerical models. For this study, the selected fastener was an HL-18, which is much stronger than the plates it connects, meaning that failure of the structure occurs at the plates. Such joints are also common in aircraft structures [11]. Note that the conclusions drawn in this research only apply to these defined simplified cases.

The SJMs compared in this study were selected based on the practicality for large-scale structural analysis. In-depth analysis and comparison of each simplified technique to the DJM is provided in section 4. One of the most important reasons for utilizing simplified joints is the savings in computational cost. As explained previously, the computational cost in the LS-DYNA explicit solver is controlled by the minimum element length. A summary of the total number of elements, the minimum element length, and the runtime for detailed and selected simplified FE models is provided in table 4. Based on table 4, it can be concluded that using SJMs does provide significant savings in computational cost achieved by using larger elements.

Table 4. Element size and runtime summary of DJM and selected simplified RBE SJMs

	Number of Elements	Min Element Length (mm)	Run Time (min)	Computational Time Savings (%)
DJM	21980 Solid Elements	0.206	595	
RBE SJM Configuration 1 (1B)	1076 Shell and 1 Beam	2.038 shell, 2.286 beam	99	83.4
RBE SJM Configuration 2 (2B)	957 Shell and 1 Beam	3.644 shell, 2.286 beam	61	89.7
RBE SJM Configuration 3 (3B)	947 Shell and 1 Beam	3.644 shell, 2.286 beam	76	88.1
RBE SJM Configuration 4 (4G)	957 Shell and 1 Beam	3.644 shell, 2.286 beam	65	89.1

Although significant computational time savings are achieved, it is paramount to analyze the performance and accuracy of these SJMs. A critical flaw identified in all the SJMs is the load required to reach failure. As shown in table 5, for all SJMs, approximately 40%–45% more load is required to induce failure. In the solid model, the fastener clearance hole is a weak point, where stress concentrations are created and failure is initiated (net section failure). However, because of the absence of the fastener clearance hole and the nature of constraints imposed by the simplified joints, the joint is no longer a weak point. In fact, the joint becomes stiffer because the stress concentrations are mitigated, away from the joint area (see figure 29), and the net section now has a larger width. Consequently, the SJMs require a larger load to initiate failure, as compared to the DJM, which may result in higher load carrying capabilities.

Because the SJMs require larger loads to reach failure, the total energy in the system and the total internal energy are also higher. The energy levels for detailed and SJMs, after failure occurs, are compared in table 5. Considering the joint (see figure 29) to be comprised of the 1-inch patch on the main part and transfer part plus the fastener, it has been found that approximately 89% of the total internal energy is stored there for the DJM, whereas only between 24%–30% is stored in the joint for the simplified bolt models. The importance of the fastener hole is highlighted by this

analysis. Incorporating the effects of the fastener hole is critical to obtain the correct energy distribution for a single-point shear loaded fastener joint.

Table 5. Comparison of remote stress at failure and energy after failure for DJM and RBE SJMs

	Remote Stress at Failure (MPa)	Excess Load for Failure Compared to Solid (%)	Total Energy (J)	Total Internal Energy (J)	Internal Energy in Joint* (J)	Internal Energy in Joint (%)
DJM	348		19	18	16	89
RBE SJM Configuration 1 (1B)	490	40.8	170	169	50	30
RBE SJM Configuration 2 (2B)	495	42.2	185	188	55	31
RBE SJM Configuration 3 (3B)	490	40.8	205	200	50	25
RBE SJM Configuration 4 (4G)	503	44.5	210	205	50	24

* Note: Joint consists of patch area on the Main Part and Transfer Part + Bolt + Nut (see figures 27–28)

Table 6 shows the comparison of LT before and after the initiation of yield on the specimen. The remote stress at which yielding begins on the specimen is also documented in table 6. Note that yielding on the DJM and the SJMs begins at different remote stresses. This can be attributed to the different constraints imposed by the simplified joints and, therefore, different structural response. Table 6 shows that many simplified joint configurations show $\leq 5\%$ difference in LT below yield. The differences in LT increase beyond yield. Note that for simplified joints that involve contacts (Configurations 2, 3, and 4), the LT is mesh sensitive. For the fine-mesh models, the LT for these three configurations is lower than for the coarse mesh models. Configurations 2B and 2M show very good correlation in terms of LT.

Table 6 enables the user to select the appropriate SJM on the basis of LT. Nevertheless, note that although the LT may be in good agreement, other parameters such as bolt loads may not compare well. It is recommended that the user understand the overall behavior of the (particular) SJM. Note that the results presented are also for single-point LT obtained from single-shear lap joint tests.

In addition, it was found that the contribution of the bolt to the LT is always higher in the SJM (80%–97%) compared to the DJM (60%–80%). This implies that the LT by friction is lower for the SJMs. Because the fastener (clearance) hole, the bolt head, and the nut are not modeled, the compressive forces induced by the bolt head and nut—due to preload—are lower, and therefore

the effect of friction on faying surfaces is minimized, resulting in a majority of the LT being carried out by the bolt.

Table 6. Comparison of LT for DJM and SJMs

Model	Configurations	Remote Stress at Initiation of Yield (MPa)	Difference in LT Before Yield (Compared to Solid) (%)	Difference in LT After Yield (Compared to Solid) (%)
DJM	DJM	194	-	-
RBE Bolt SJM with Hole	1	75	0–4 Higher	4–10 Higher
	1A	259	0–7 Higher	5–7 Higher
	1B	138	0–4 Higher	4–5 Higher
Mesh- Independent Spotweld Beam SJM	2	269	0–17 Lower	16–17 Lower
	2A	294	0–11 Higher	11–12 Higher
	2B	282	0–3 Higher	1–3 Higher
	2E	293	0–5 Higher	1–5 Higher
	2K	301	0–9 Higher	6–9 Higher
	2L	292	0–9 Higher	6–9 Higher
	2M	288	0–0.5 High/Low	0–7 Lower
	2O	299	1–7 Lower	2–9 Lower
Mesh- Independent Spotweld Beam SJM with EP	3	180	0–8 Lower	8–1 Lower
	3A	288	0–1 Higher	1–1 Higher
	3B	302	0–11 Higher	11–12 Higher
RBE Bolt SJM with No Hole	4	188	5–7 Lower	5 Low–2 High
	4A	316	3–10 Lower	3 Low–3 High
	4E	304	5 Low–3 High	3–5 High
	4G	274	5 Low–0.5 High	0.5–6 Higher

In terms of the axial loads on the bolt, as expected, the DJM showed a drop in axial loads from the initial preload. All the SJMs except Configuration 4 also exhibited a drop in axial loads from the initial preload (Configurations 1-1B, 2-2O, and 3-3B). However, the drop in axial loads for the SJMs occurred at different remote stresses. In most SJMs (except Configuration 4), the axial loads also increased after the initial drop. Only for a few SJMs, the axial loads surpassed the initial preload—close to reaching failure (Configuration 3, 2E, 2M). Therefore, overall, it can be concluded that for simplified Configurations 1, 2, and 3, the axial loads are sensitive to the mesh arrangement at the joint. For Configuration 4, the axial loads showed an increasing behavior, and the loads were similar for all the different variations of Configuration 4.

The shear loads showed data scatter for all the configurations. For some cases, the shear forces in the fastener were higher than the DJM, whereas for others, the shear forces were lower. For all

variations in Configuration 4, the shear forces showed good correlation to the DJM at low remote stresses. Therefore, it can be concluded that fastener shear forces are sensitive to mesh and the constraints imposed by the simplified joints.

The SG locations are shown in figure 23. From a comparison of axial strains, it was found that the strain at SG 1, which was on the load introduction side of the main part, showed very good correlation with the DJM. This indicated that the use of shell elements was sufficient to capture the axial strains. However, because the LT changed in the SJMs, the strains at SG 2 and SG 3 also varied when compared to the DJM. The strains at SG 2 and SG 3 were in good agreement to the DJM only for Configurations 2B and 2M, which showed good correlation of LT. The stresses and strains at preload did not compare well to the DJM due to the absence of the fastener hole and the fastener head and nut. Finally, the stress distribution at the failure initiation was also different for the SJMs because of stress concentrations occurring at different locations.

5.4 JOINT PERFORMANCE AT HIGH STROKE RATES—MESH-INDEPENDENT SPOTWELD BEAM MODEL CONFIGURATION 2B VERSUS DJM

5.4.1 LT

The tests showed that the LT increased for higher stroke rates. Through simulation of the DJM, it was found that modeling the SL system was critical to capture the LT exhibited in testing. Good correlation of LT for high stroke rates was observed for the DJM after including the SL. The correlation can further be improved by modeling more details of the SL, as shown in section 4.3.1.1.2.

The SJM Configuration 2B (mesh-independent spotweld beam model, section 3.1.2.2) was chosen for high stroke rate studies. Configuration 2B already showed good correlation of LT to the solid model for quasi-static rate. This joint method is the most practical for large FE models because of its simplicity and has been used in several crash studies involving large aircraft structures [7, 12]. For high stroke rates, the SJM—Configuration 2B—with the SL also showed good correlation to the DJMs.

5.4.2 Stresses and Strains

For the DJM at increasing stroke rates, the von Mises stress fields around the fastener hole and SG 1 area, on the main part, were also getting larger. When the specimens reached failure, the strains at the SG locations were also higher for increasing stroke rates. In comparison to the test data, the strains at the gauge locations for the simulations were similar but do not capture the oscillations seen on the test. The strain rates on the simulation were slightly higher at the SG 1 location but became similar to the test when the specimen was closer to failure. For the elements that failed in the simulation, at the net section, the strain rates were 400/s for 100 in./s, 300/s for 50 in./s, and approximately 130/s for 20 in./s stroke rate. The measurement of strain rates at this location on the test was not feasible.

As observed in the quasi-static analysis, the failure load for the SJMs was also larger for higher stroke rates compared to the DJM, and this can be attributed to the absence of the fastener clearance hole. Although the failure loads were higher, the trends of stresses and strains for SJMs were the opposite to what was observed in the DJM. For instance, the maximum load and the von Mises

stress fields showed a decreasing trend for higher stroke rates, whereas for the DJM, the maximum load and von Mises stress fields showed an increasing trend for higher stroke rates. Similarly, the strains at the gauge locations were also lower for higher stroke rates in the SJMs. The strain rates at the SG 1 location were similar to the DJM. The strain rates near the fastener (failing elements) were much lower for the SJMs compared to the DJM, with just 200/s for 100 in./s, 80/s for 50 in./s, and approximately 50/s for 20 in./s stroke rate.

5.4.3 Fastener Loads

For the DJM, the axial loads on the fastener were similar for all the stroke rates. The shear forces for higher stroke rates were lower and showed a more linear behavior compared to the QS analysis. As a result, the T by the fastener was also lower for higher stroke rates, and after overcoming the initial slip, the LT also showed a linear behavior compared to the QS analysis.

For the SJMs, the axial forces were higher than QS for the larger stroke rates, whereas the shear forces were similar. The LT by fastener was lower than QS for higher stroke rates but much higher in general than the results from the DJM.

5.4.4 Energies

A summary of the energies from the QS and high stroke rate simulations for detailed and SJM is provided in table 7. For the DJM, the total energy and the total internal energy increased for higher stroke rates. The percentage of internal energy stored in the joint decreased by 10% for the DJM when comparing QS to 100 in./s stroke rate. This indicated that at higher stroke rates, although the strain rates were much higher at the net section (fastener clearance hole area), there were also higher deformations away from the hole.

The opposite trend was observed on the SJMs, in which the total energy and total internal energy decreased with increasing stroke rate. The percentage of internal energy stored in the joint also increased by 5% for QS to 100 in./s stroke rate. Although the trend was opposite for the SJMs, the magnitude for total energy was much higher because of the shell models reaching failure at a much higher load.

Table 7. Comparison of internal energy for high stroke rate simulations for the DJM vs. RBE Configuration 2B SJM

	Stroke Rate	Total Energy (J)	Total Internal Energy (J)	Internal Energy on Rest of Specimen (%)	Internal Energy in Joint (%)
DJM	QS	19	18	11	89
	20	22.5	21	15	85
	50	25	23	17	83
	100	28.5	26.5	21	79
RBE SJM Configuration 2B	QS	188	185	69	31
	20	175.5	173	68	32
	50	151	145	65	35
	100	153	148	64	36

* Note: Joint Consists of patch area on the Main Part and Transfer Part + Bolt + Nut (figure 29)

6. CONCLUSIONS

There is a significant desire from industry, academia, and certification authorities to use analysis in the design and certification process of aircraft to minimize cost and reduce the time to certification. However, detailed joint modeling is not practical in large structures with a large number of fasteners. In this study, simplified joint numerical modeling methods were explored and analyzed in detail to support crashworthiness computational analysis of large structural models. This was accomplished by testing a lap shear joint specimen under tension at different stroke rates; generating and validating a detailed three-dimensional (3D)/solid FE joint model (DJM) to be used as a baseline; comparing various simplified finite element (FE) joint models (SJMs) to the baseline at quasi-static (QS) loading; and finally comparing the best candidate SJM to the DJM detailed model at different stroke rates.

For the case of single point LT, in which the fastener is much stronger than the joining plates and the failure is expected on the plates, it can be concluded that SJMs can be used for low loading conditions. Beyond yield, the difference in results increases, and a thorough understanding of the limitations and behavior of the selected simplified method is important. Overall, the simplified methods successfully captured the LT mechanism of the joint, but because of the absence of a fastener clearance hole and bolt head and nut, the failure modes and energy levels differed.

It was found through testing that the LT increased when single-point bolted joints were subjected to high stroke rates. To capture the same increase in the numerical models, it was imperative to model the SL that was used for testing. Further analysis of the DJM subjected to high stroke rates revealed that at high strain rates the total energy, total internal energy, stress fields, strains, and maximum load increased. However, the internal energy distribution changed with 10% less internal energy at the joint (1-inch patch) for 100 in./s stroke rate compared to QS.

The use of simplified joints did result in significant savings in computational cost, and therefore may be employed for a quick evaluation of design concepts or for preliminary studies. For areas in which detailed information is required, it is recommended to use a DJM. It is rather difficult, a priori, to determine if the SJMs suffice as a replacement for DJMs because they are subject to the end use and purpose of the particular overall model.

Simplified joints have been used to model large structures successfully; however, a clear understanding of their limitations, selection, and use are necessary.

7. RECOMMENDATIONS AND FUTURE WORK

This study was performed using a steel fastener and aluminum plates, with the fastener subjected to shear through tensile loading of the specimen. For a complete understanding of the effects and limitations of simplified joining methods, the following topics should also be studied:

1. Single point LT using rivets.
2. Single point LT using steel bolt and rivets but under compression.
3. Multiple point LT using steel bolts and rivets in both tension and compression. Whereas the understating of single fastener joint is important, most of the components in large-scale structures are connected using several fasteners placed in different patterns. It would be valuable to understand the performance of simplified finite element joining methods for such joints.
4. Bending of bolts.
5. Component level study of bolted and riveted joints.

Covering all these topics could provide comprehensive insight and data into joint performance, and how the representation of joints can be improved for large-scale FE models intended for crash analysis. As the tools and computing power increase, allowing for larger numerical models, the development of modeling methods is also critical for maintaining accuracy.

8. REFERENCES

1. Ostergaard, M. G., Ibbotson, A. R., Le Roux, O., and Prior, A.M. (2011). Virtual testing of aircraft structures. *CEAS Aeronautical Journal*, 1(1–4), 83–103.
2. Fasanella, E. L., and Jackson, K. E (2001). *Crash simulation of a vertical drop test of a B737 fuselage section with auxiliary fuel tank*. Presented at the Third Triennial International Fire & Cabin Safety Research Conference, Atlantic City, NJ.
3. Fasanella, E. L., Jackson, K. E. and Lyle, K. H. (2002). Finite Element Simulation of a Full-Scale Crash Test of a Composite Helicopter. *Journal of the American Helicopter Society*, 47(3), 156–168.
4. Olivares, G., and Yadav, V. (2007). *Mass transit bus-vehicle compatibility evaluations during frontal and rear collisions*, Proceedings from the 20th International Technical Conference Enhanced Safety of Vehicles, Lyon, France.

5. Dhole, N., Yadav, V., and Olivares, G. (2012). *Certification by Analysis of a Typical Aircraft Seat*. 12th International LS-DYNA Users Conference, Dearborn, Michigan.
6. Olivares, G. (2006). *Transit bus crashworthiness: Finite Element modeling and validation*. International Crashworthiness Conference, Athens, Greece.
7. Byar, A. (2003). "A crashworthiness study of a Boeing 737 fuselage section," Ph.D. dissertation, Drexel University, Philadelphia, PA.
8. FAA. (2003, May). AC 20-146, *Methodology for Dynamic Seat Certification by Analysis for Use in Parts 23, 25, 27 and 29 Airplanes and Rotorcraft*. Washington, D.C.: Government Publishing Office.
9. Bickford, J. H. (2007). *Introduction to the design and behavior of bolted joints: non-gasketed joints*, Boca Raton, FL: CRC Press.
10. Fisher, J. W., Struik, J. and Kulak, G. (1974). *Guide to design criteria for bolted and riveted joints*, Hoboken, NJ: Wiley Press.
11. Skorupa, A., and Skorupa, M. (2012). *Riveted lap joints in aircraft fuselage: design, analysis and properties, Vol. 189*, New York, NY: Springer Publishing.
12. FAA Report. Crashworthiness Analysis of Generic Narrow Body Aircraft. (DOT/FAA/(TC-20/3). Publication in progress.
13. LSTC. (2011) "LS-DYNA," Livermore, CA: Livermore Software Technology Corp., Retrieved from: <http://www.lstc.com/products/ls-dyna>.
14. Keshavanarayana, S., Smith, B. L., Gomez, C., Caido, F. (2010). Fatigue-based severity factors for shear-loaded fastener joints. *Journal of Aircraft*, 47(1), 181–191.
15. Barrios, W. (1978). Stresses and Displacements due to Load Transfer by Fasteners in Structural Assemblies. *Engineering Fracture Mechanics*, 10(1), 115–176.
16. Jarfall, L. (1969). Fatigue Cycling of Riveted or Bolted joints. (FFA report HF-1239), The Aeronautical Research Institute of Sweden.
17. Narkhede, S., Lokhande, N., Gangani, B., and Gadekar, G. (2010). *Bolted Joint Representation in LS-DYNA® to Model Bolt Pre-Stress and Bolt Failure Characteristics in Crash Simulations*. Presented at the International LS-DYNA Users Conference, USA.
18. Ghods, F. (2011). "Finite element modeling of single shear fastener joint specimens: a study of clamp-up, friction and plasticity effects." (Thesis), Wichita State University.
19. Oskouei, R. H., Keikhosravy, M., and Soutis, C. (2010). A finite element stress analysis of aircraft bolted joints loaded in tension. *Aeronautical Journal*, 114(1155), 315.

20. Soo Kim, T., and Kuwamura, H. (2007). Finite element modeling of bolted connections in thin-walled stainless steel plates under static shear. *Thin-Walled Structures*, 45(4), 407–421.
21. Kim, J., Yoon, J., and Kang, B. (2007). Finite element analysis and modeling of structure with bolted joints. *Applied Mathematical Modelling*, 31(5), 895–911.
22. Montgomery, J. (2002). *Methods for modeling bolts in the bolted joint*, ANSYS user's conference, Vol. 5.
23. Marzenmiller, A., Schweizerhof, K., and Rust, W. (1994). *Joint Failure Modeling in Crashworthiness Analysis*. Presented at the Second International LS-DYNA3D Conference, San Francisco, CA.
24. Tanlak N., Sonmez, F.O., and Talay, E. (2011). Detailed and simplified models of bolted joints under impact loading. *The Journal of Strain Analysis and Engineering Design*, 46(3), 213–225.
25. Sonnenschein, U. (2008). *Modelling of bolts under dynamic loads*. Presented at LS-Dyna Anwenderforum, Bamberg, Germany.
26. Du Bois, P. A. (2000). *Crashworthiness engineering with LS-DYNA*. Stuttgart, Germany: Daimler-Chrysler AG.
27. Birch, R. S., and Alves, M. (2000). Dynamic failure of structural joint systems. *Thin-walled structures*, 36(2) 137–154.
28. Swedish Defence Research Agency Technical Report. (2002). Mechanically fastened joints: critical testing of single overlap joints. (FOI-R-0441-SE).
29. Wang, G. S. (2001). *Computational Method for Evaluating the Fatigue Life of Mechanical Joints*. Kista, Stockholm: Aeronautics division, Swedish Defence Research Agency.
30. Zeng, L., Haylock, L., Zonker, H., Goodman, J., and Burg, J. (2006). “Effects of Coating Tribology on Fastener Single and Double Shear Strength,” No. 2006-01-3155, SAE Technical Paper.
31. Young, W. C., and Budynas, R. G. (2002). *Roark's formulas for stress and strain*, Vol. 7, New York, NY: McGraw-Hill.
32. Ireman T. (1998). Three-dimensional Stress Analysis of Bolted Single-lap Composite Joints, *Composite Structures*, 43(3), 195–216.
33. Schijve, J. (2009). Fatigue damage in aircraft structures, not wanted, but tolerated?, *International Journal of Fatigue*, 31(6), 998–1011.
34. Jarfall, L. (1986). Shear Loaded Fastener Installations, *International Journal of Vehicle Design*, 7(3–4), 337–380.

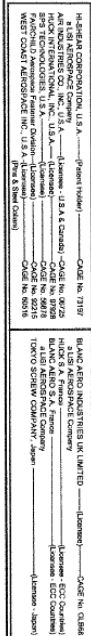
35. Ekh,J., Schon, J., and Melin, L. G., "Secondary bending in multi fastener, composite-to-aluminium single shear lap joints," *Composites Part B: Engineering*, Vol. 36, pp. 195-208, 2005.
36. van der Linden, H. H. (1985). Fatigue Rated Fastener Systems - An AGARD Coordinated Testing Program. (DTIC ADA164689).
37. Hi-shear Corporation, (July 2004). "Product Specification hi-lok/ hi-tigue and hi-lok fastening systems hi-lok/ hi-tigue and hi-lok collars," Spec. No. 345.
38. Hi-shear Corporation, 2600 Skypark Drive, Torrance, CA 90509
39. Vand, E., Hemmati, R., Oskouei, H., and Chakherlou, T. N. (2008). An experimental method for measuring clamping force in bolted connections and effect of bolt threads lubrication on its value. *Proc. of World Academy of Science: Engineering & Technology*, Vol. 48, (457–460).
40. Transducer Techniques, LLC., 42480 Rio Nedo Temecula, CA 92590.
41. Tohnichi America Corporation, 1303 Barclay Blvd., Buffalo Grove, IL 60089.
42. MTS Systems Corporation, 1400 Technology Drive, Eden Prairie, MN 55344.
43. FAA Report. (2007). Crashworthiness of Composite Fuselage Structures Material Dynamic Properties (Phase-I). (DOT/FAA/(AR)-09/8).
44. Micro-Measurements, 951 Wendell Blvd., Wendell, NC 27591
45. Day, J., Bala, S. (2006) *General Guidelines for Crash Analysis in LS-DYNA*, Copyright Livemore Software Technology Corporation.
46. Livermore Software Technology Corporation (2007). *LS-DYNA Keyword User's Manual Volume I*, Livermore, CA: Livermore Software Technology Corporation.
47. Yadav, V. (2006). "Finite element modeling and side impact study of a low-floor mass transit bus," (Thesis), Wichita State University.
48. Livermore Software Technology Corporation (n.d.). LS-DYNA User's Guide, Retrieved from <http://www.dynasupport.com/tutorial/ls-dyna-users-guide>, accessed 06 June, 2014.
49. Livermore Software Technology Corporation (2014). *LS-DYNA Theory Manual*, Livermore, CA: Livermore Software Technology Corporation.
50. Bala, S. (2006). *Deformable Spotwelds in LS-DYNA for Impact and NVH Applications*, Copyright Livemore Software Technology Corporation.
51. Nakalswamy, K. K. (2010). Experimental and numerical analysis of structures with bolted joints subjected to impact load, *UNLV Theses/Dissertations/Professional*

Papers/Capstones, Paper 227, 2010,
<http://digitalscholarship.unlv.edu/thesesdissertations/227>

52. U.S. Dept. of Transportation Report. (2003). *Metallic Material Properties Development and Standardization*. (MMPDS-01).
53. W.S. Hampshire Inc. (2014) "Teflon-Typical Properties of PTFE," 365 Keyes Ave., Hampshire, IL, 60140. http://catalog.wshampshire.com/Asset/psg_teflon_ptfe.pdf
54. Livermore Software Technology Corporation (2014). *LS-DYNA Keyword User's Manual Volume II*, Livermore, CA: Livermore Software Technology Corporation.
55. FAA Report. (2018). Round Robin Exercise For Tension Testing Of Laminated Composites at Different Strain/Stroke Rates. (DOT/FAA/TC-18/10).
56. ASTM Standard B209 - 10, "Standard Specification for Aluminum and Aluminum-Alloy Sheet and Plate," ASTM International, West Conshohocken.

Appendix A is the details of a HI-LOK™ fastener by Hi-Shear Corporation.

2600 SKYPARK DRIVE, TORRANCE, CALIFORNIA 90509 U.S.A.



SEE COLLAR STANDARDS
FOR COLLAR STRENGTHS.
LOWER STRENGTH (PIN OR
COLLAR) DETERMINES
SYSTEM STRENGTH.

SPECIFICATION: Hi-Lok Product Specification 342.

Pin Part Number Only (25)
HL18PB8-8
TTTT

Second dash number indicates maximum grip in 1/16ths. See Finish note for explanation of code letters.

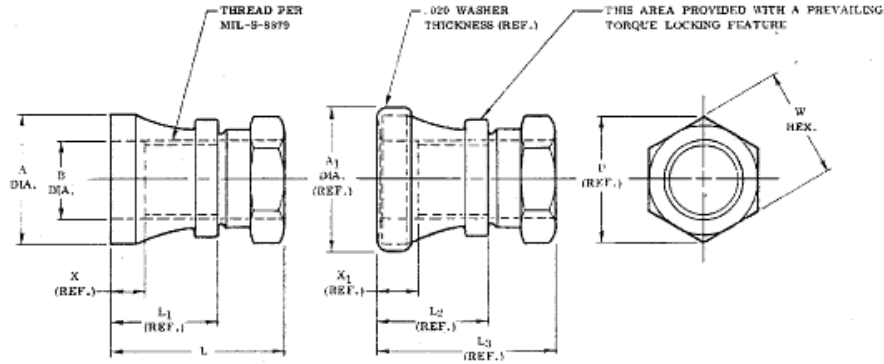
ISSUANCE DATE	7-19-82	HL-LOK® PIN PROTRUDING SHEAR HEAD ALLOY STEEL 1/16 GRIP VARIATION
APPROVED DATE	7-24-82	
REVISION		
DATE	10-17-82	
DRAWING NUMBER		HL18

STANDARDS COMMITTEE FOR HI-LOK® PRODUCTS

2500 SKYPARK DRIVE, TORRANCE, CALIFORNIA 90509 U.S.A.

HI-SHEAR CORPORATION, U.S.A. (Parent/Origin) CASE No. 72187
2500 Skypark Drive, Torrance, CA, U.S.A. (Licensee - U.S.A. Country) CASE No. 08728
AIR INDUSTRIES CO., INC., U.S.A. (Licensee - U.S.A. Country) CASE No. 07108
HICK INTERNATIONAL, INC., Oakbrook, U.S.A. (Licensee - U.S.A. Country) CASE No. 08118
SPS TECHNOLOGIES, U.S.A. (Licensee - U.S.A. Country) CASE No. 08118
FACON/ALC Americas, Inc., U.S.A. (Licensee - U.S.A. Country) CASE No. 08118
WEST COAST AEROSPACE INC., U.S.A. (Licensee - U.S.A. Country) CASE No. 08118
(Print & Sign Here)

HI-SHEAR FASTENERS EUROPE LTD., U.K. (Licensee - CASE No. 01086)
Export of Hi-Shear Products to U.S.A.
HICK INTERNATIONAL, GmbH & Co., Germany (Licensee - SEE Country)
SANTO CHAMINGO GRANAT, S.A., Spain (Licensee - SEE Country)
SOMMERFELD S.A., France (Licensee - SEE Country)
TOKYO DENSO COMPANY, Japan (Licensee - Japan)



DASH NO.	PIN NOM. DIA.	THREAD	A DIA.	A1 DIA (REF.)	B DIA.	L LENGTH	L1 (REF.)	L2 (REF.)	L3 (REF.)	P (REF.)	W HEX.	X (REF.)	X1 (REF.)	UTS POUNDS MIN.	TORQUE OFF IN. LBS.
5	5/32	8-32UNJC-3B	.292	.337	.173	.447	.270	.300	.487	.344	.314	.107	.137	1,400	15-25
6	3/16	10-32UNJF-3B	.307	.360	.200	.457	.280	.310	.477	.344	.314	.107	.137	1,800	25-35
8	1/4	1/4-28UNJF-3B	.412	.482	.261	.552	.340	.370	.572	.380	.346	.112	.142	3,000	60-80
10	5/16	5/16-24UNJF-3B	.518	.575	.325	.672	.430	.460	.692	.484	.440	.122	.152	5,000	130-160
12	3/8	3/8-24UNJF-3B	.628	.690	.388	.744	.470	.500	.784	.557	.503	.122	.152	7,000	200-240
14	7/16	7/16-20UNJF-3B	.713	.770	.450	.882	.560	.590	.882	.624	.565	.137	.167	9,500	270-330
16	1/2	1/2-20UNJF-3B	.815	.872	.513	.942	.610	.640	.962	.763	.690	.137	.167	12,500	370-430
18	9/16	9/16-18UNJF-3B	NOTE: USE HL79-18												
20	5/8	5/8-18UNJF-3B	NOTE: USE HL79-20												
24	3/4	3/4-16UNJF-3B	NOTE: USE HL79-24												
28	7/8	7/8-14UNJF-3B	NOTE: USE HL79-28												
32	1	1-12UNJF-3B	NOTE: USE HL79-32												

- NOTES:**
- Go thread penetration shall be 3/4 of one revolution minimum.
 - Dimensions apply after finish.
 - Use HL79 for oversize replacement.

MATERIAL: Collar - 2024 aluminum alloy per QQ-A-430 or QQ-A-225/6.
Washer - "NW" = 300 series stainless steel.
"TW" = 5052 aluminum alloy per QQ-A-250/8, or 2024 aluminum alloy per QQ-A-250/4 OR QQ-A-250/5.

HEAT TREAT: Collar - Age to T6 condition per MIL-H-6088.
Washer - "NW" = None.
"TW" = Age to T6 condition per MIL-H-6088 (for 2024 only).

FINISH: Collar - HL70(-) = Anodize per MIL-A-8625, dye color red, and cetyl alcohol lube per Hi-Shear Spec. 305.
HL70CM(-) = Chemical conversion coat per MIL-C-5541, Class 1A, and cetyl alcohol lube per Hi-Shear Spec. 305.
HL70D(-) = Anodize per MIL-A-8625 and solid film lube per MIL-L-46010, Type I.
HL70K(-) = Anodize per MIL-A-8625 and solid film lube per "Lubeco" 905.
HL70TF(-) = Anodize per MIL-A-8625 and Hi-Kote 2 solid film lube per Hi-Shear Spec. 292.
HL70TT(-) = Anodize per MIL-A-8625, dye color red and transblue.
Collar & Washer - HL70DTW(-) = Collar finish is the same as HL70D(-). Washer finish is anodize per MIL-A-8625, dye color grey, or blue (for 2024 only).
HL70NW(-) = Collar finish is the same as HL70(-). Washer is passivated.
HL70TW(-) = Collar finish same as HL70(-). Washer finish is anodize per MIL-A-8625, dye color grey, or blue (for 2024 only).

SPECIFICATION: Hi-Lok Product Specification 345.

CODE: Dash number indicates nominal thread size in 1/32nds.
See Finish note for explanation of code letters.

EXAMPLE: HL70-B = 1/4-28 Hi-Lok collar only.
HL70TW-B = 1/4-28 Hi-Lok collar with aluminum washer.

U.S. patents 3,390,906; and foreign patents.
"Hi-Lok" and "HL" are Registered Trademarks of Hi-Shear Corporation.

DRAWN	DATE	BY	TITLE	DRAWING NUMBER
	7-27-60	VAN		
APPROVED	7-27-60	MEC	HI-LOK® COLLAR 2024 - T6 ALUMINUM ALLOY 1/16" GRIP VARIATION - SHEAR APPLICATION	HL70
(31) REVISION	11-28-95	J.F.Obispo		

©1994 Hi-Shear Corporation

APPENDIX B—SIMPLIFIED JOINT MODELING TECHNIQUES

Appendix B is an illustration and a short description of several joint modeling methods. It includes a detailed three-dimensional (3D)/solid joint finite element (FE) model (DJM) and simplified FE joint models (SJMs).

Research using FE modeling DJMs [B-1–B-3] and SJMs [B-4–B-5] has been conducted under various loading conditions. Some of the DJMs and SJMs, which can be modeled in LS-DYNA, are documented in table B-1. The SJMs are evaluated based on their applicability to large structural crashworthiness FE models.

In addition to the methods described in table B-1, researchers have developed more complex ways of representing a bolt using simplified elements. Gadekar et al. [B-6] developed and validated a bolt model, using LS DYNA, employing three different element types, as shown in figure B-1. The bolt shank was modeled with a beam element and is connected to the periphery of the clearance hole using contact springs. Shell element patches, representing the bolt head and nut, are modeled as rigid bodies.

They found that under shear loading, stress patterns closely matched with realistic physical behavior for both configurations. The tensile and compressive behavior of the beam bolt SJM closely matched that of the DJM. The physical tensile test showed a softer response in the elastic region compared to simulation predictions. The frictional forces were also well predicted by the proposed models and they closely matched the physical test results. Gadekar et al. concluded that both approaches show good correlation with theoretical calculations and physical test results under shear and tensile loadings. The beam model is advantageous if failure forces for the bolted joint are known under different loading conditions. In the context of crash applications, further detailed study is required using dynamic loading.

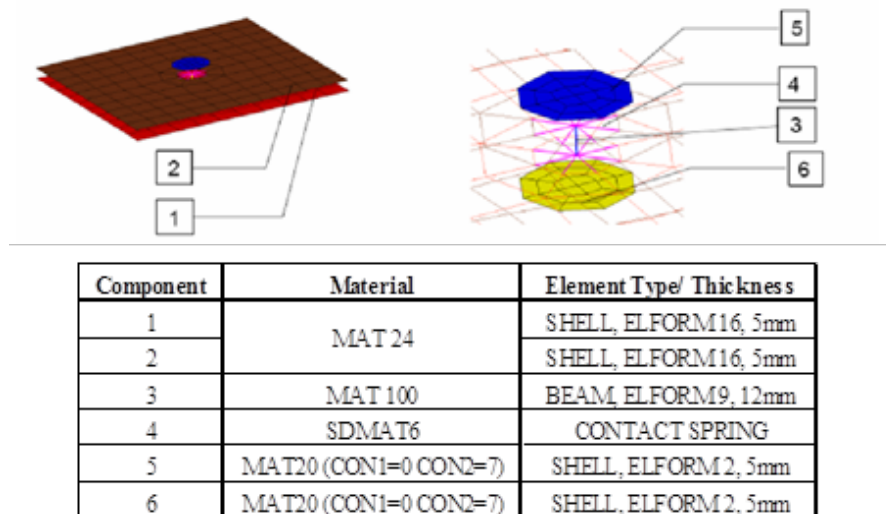


Figure B-1. FE bolt model by Gadekar et al. [B-6]

Figure B-2 shows a bolt model generated by U. Sonnenschein [B-7]. This model consists of three different components. The bolt shank is modeled with a beam element, and shell elements are used

for the head and nut. Null beams are modeled around the periphery of the clearance hole for contact purposes. The model showed good force characteristics and correlation to calculated bolt failure. Plastic deformations observed in the test were also reflected in the simulation.

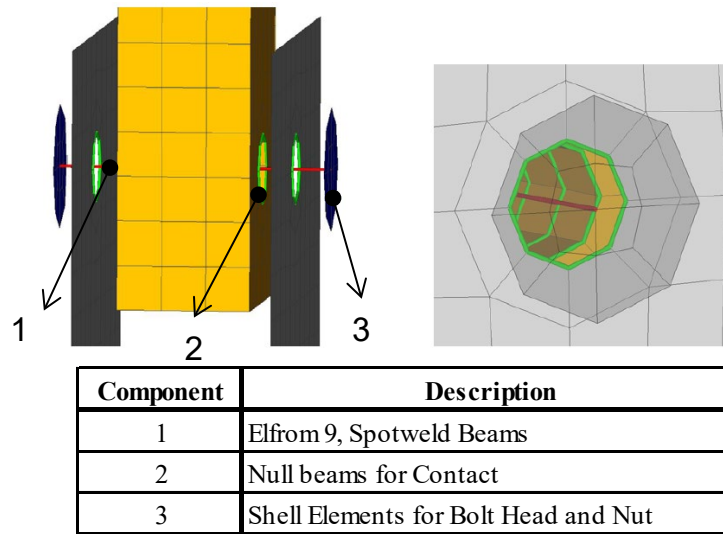


Figure B-2. FE bolt model by U. Sonnenschein [B-7]

Table B-1. Bolt modeling techniques used in FEM

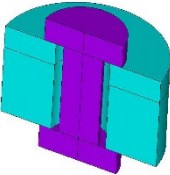
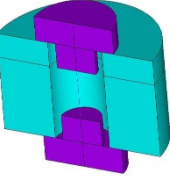
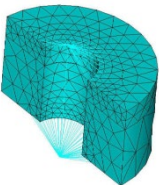
Technique	Illustration	Description	Advantages	Disadvantages	FE Modeling	REF
1. Solid Bolt Model		Head, nut and bolt shank modeled with solid elements	<ul style="list-style-type: none"> - Provides best accuracy - Allows transfer of tensile, bending, and thermal loads - Complete stress distribution can be obtained - Allows preload application - Failure can be modeled 	<ul style="list-style-type: none"> - Requires contact definitions - Consists of high number of elements - Not practical for large structural models 	<ul style="list-style-type: none"> - Not practical for large structural models - Requires modeling of hole 	
2. Hybrid Bolt Model		Head and nut modeled with solid elements. Shank with beam element	<ul style="list-style-type: none"> - Allows transfer of tensile, bending, and thermal loads - Complete stress distribution can be obtained - Allows preload application - Failure can be modeled 	<ul style="list-style-type: none"> - Requires contact definitions - Consists of high number of elements - Not practical for large structural models 	<ul style="list-style-type: none"> - Not practical for large structural models - Requires modeling of hole 	
3. Spider Bolt Model		Head, nut, and bolt shank modeled with beam elements	<ul style="list-style-type: none"> - Allows transfer of tensile, bending, and thermal loads - Requires small number of elements and simplified process of extracting results - Failure can be modeled 	<ul style="list-style-type: none"> - Requires contact definitions - Properties of beams have to be set to represent the head and nut moment of inertia and volume - Time consuming for large models 	<ul style="list-style-type: none"> - Time consuming for large models - Requires modeling of hole 	

Table B-1. Bolt modeling techniques used in FEM (continued)

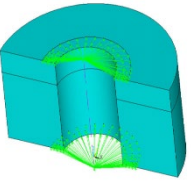
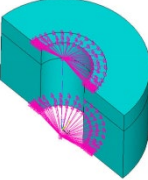
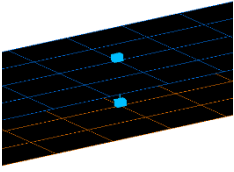
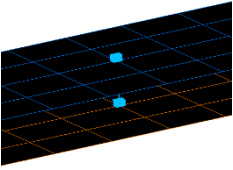
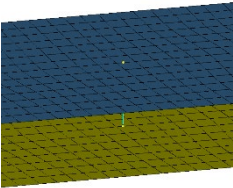
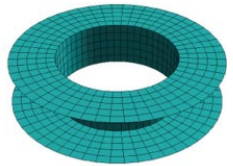
Technique	Illustration	Description	Advantages	Disadvantages	FE Modeling	REF
4. Coupled Bolt Model		Only bolt shank modeled with beam element. DOF of surround nodes coupled with beam to represent head and nut. Many different variations exist.	<ul style="list-style-type: none"> - One beam element to define bolt - Allows preload application - Does not require contact definition - Can be modeled without hole - Failure can be modeled 	<ul style="list-style-type: none"> - Allows only axial loads to be transferred through coupled nodes 	<ul style="list-style-type: none"> - Time-consuming setup for large models 	
5. Rigid Body Element (RBE) Bolt Model		Only bolt shank modeled with beam element. Surrounding nodes of hole connected with beam using RBE to represent head and nut	<ul style="list-style-type: none"> - One beam element to define bolt - Allows preload application - Does not require contact definition - Allows transfer of tensile, bending and thermal loads - Failure can be modeled 	<ul style="list-style-type: none"> - Rigid elements do not account for stiffness 	<ul style="list-style-type: none"> - Time consuming setup for large models - Requires modeling of hole 	
6. Massless Truss Element Bolt		Head and nut not modeled. Truss element represents bolt shank. Connected node to node. Type of a nodal constraint.	<ul style="list-style-type: none"> - One beam element to define bolt - Hole is not modeled - Does not require contact definition - Failure can be modeled 	<ul style="list-style-type: none"> - Only transfers axial loads - Absence of fastener hole mitigates stress concentrations 	<ul style="list-style-type: none"> - Time consuming setup process as mesh has to be controlled because connection is node to node 	[B-4]

Table B-1. Bolt modeling techniques used in FEM (continued)

Technique	Illustration	Description	Advantages	Disadvantages	FE Modeling	REF
7. Massless Beam Element Bolt		Head and nut not modeled. Beam element represents bolt shank. Connected node to node. Type of a nodal constraint.	<ul style="list-style-type: none"> - One beam element to define bolt - Hole is not modeled - Does not require contact definition - Failure can be modeled 	<ul style="list-style-type: none"> - Absence of fastener hole mitigates stress concentrations 	- Time-consuming setup process as mesh has to be controlled because connection is node to node	[B-4]
8. Mesh-Independent Spotweld Modeled with Beams		Head and nut not modeled. Beam element represents bolt shank. Connected to parts using tied contact	<ul style="list-style-type: none"> - Allows transfer of tensile, bending, and thermal loads - One beam element needed - Mesh-independent; therefore less preprocessing time - Failure can be modeled 	<ul style="list-style-type: none"> - Requires contact definitions - Absence of fastener hole mitigates stress concentrations - Results vary with position of beam relative to center of contact segment 	<ul style="list-style-type: none"> - Practical for large models - Does not require modeling holes - Quick modeling 	[B-4], [B-8]
9. Shell Elements Bolt		Shell elements used to model head nut and bolt shank	<ul style="list-style-type: none"> - Provides better accuracy than beams - Allows transfer of tensile, bending, and thermal loads - Allows preload application - Failure can be modeled 	<ul style="list-style-type: none"> - Requires contact definitions - Consists high number of elements - Not practical for large structural models 	<ul style="list-style-type: none"> - Not practical for large structural models - Requires modeling of hole 	[B-5]

REFERENCES

- B-1. Ghods, F. (2011). “*Finite element modeling of single shear fastener joint specimens: a study of clamp-up, friction and plasticity effects.*” (Thesis), Wichita State University.
- B-2. Oskouei, R. H., Keikhosravy, M., and Soutis, C. (2010). A finite element stress analysis of aircraft bolted joints loaded in tension. *Aeronautical Journal*, 114(1155), 315.
- B-3. Soo Kim, T., and Kuwamura, H. (2007). Finite element modeling of bolted connections in thin-walled stainless steel plates under static shear. *Thin-Walled Structures*, 45(4), 407–421.
- B-4. Marzenmiller, A., Schweizerhof, K., and Rust, W. (1994). *Joint Failure Modeling in Crashworthiness Analysis*. Presented at the Second International LS-DYNA3D Conference, San Francisco, CA.
- B-5. Tanlak N., Sonmez, F.O., and Talay, E. (2011). Detailed and simplified models of bolted joints under impact loading. *The Journal of Strain Analysis and Engineering Design*, 46(3), 213–225.
- B-6. Narkhede, S., Lokhande, N., Gangani, B., and Gadekar, G. (2010). *Bolted Joint Representation in LS-DYNA® to Model Bolt Pre-Stress and Bolt Failure Characteristics in Crash Simulations*. Presented at the International LS-DYNA Users Conference, USA.
- B-7. Sonnenschein, U. (2008). *Modelling of bolts under dynamic loads*. Presented at LS-Dyna Anwenderforum, Bamberg, Germany.
- B-8. Du Bois, P. A. (2000). *Crashworthiness engineering with LS-DYNA*. Stuttgart, Germany: Daimler-Chrysler AG.

APPENDIX C—LOAD TRANSFER TEST RESULTS

Load transfer (LT) results for a detailed three-dimensional (3D)/solid joint finite element (FE) model (DJM) and test results at quasi-static, 20 in./s, 50 in./s, and 100 in./s stroke rates.

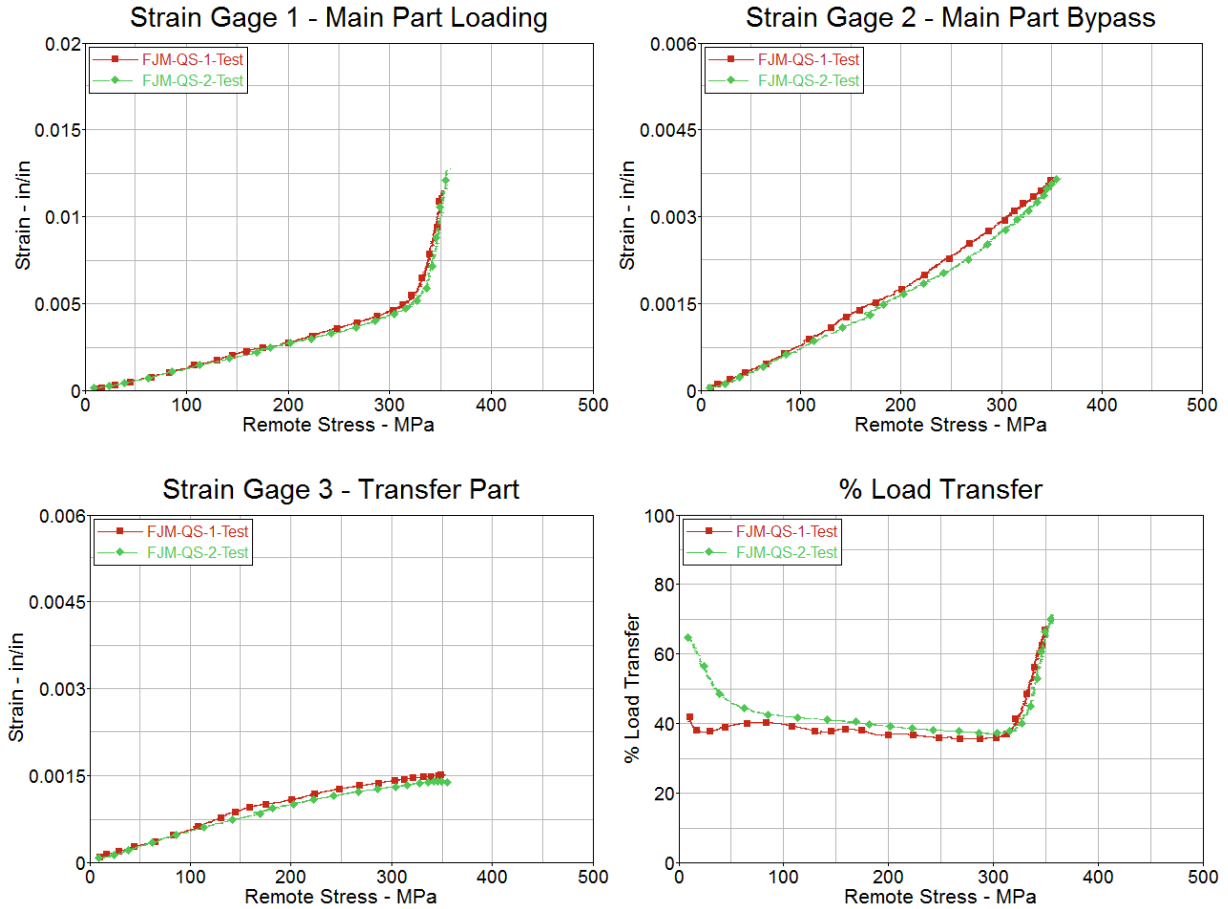


Figure C-1. LT test results at quasi-static stroke rate

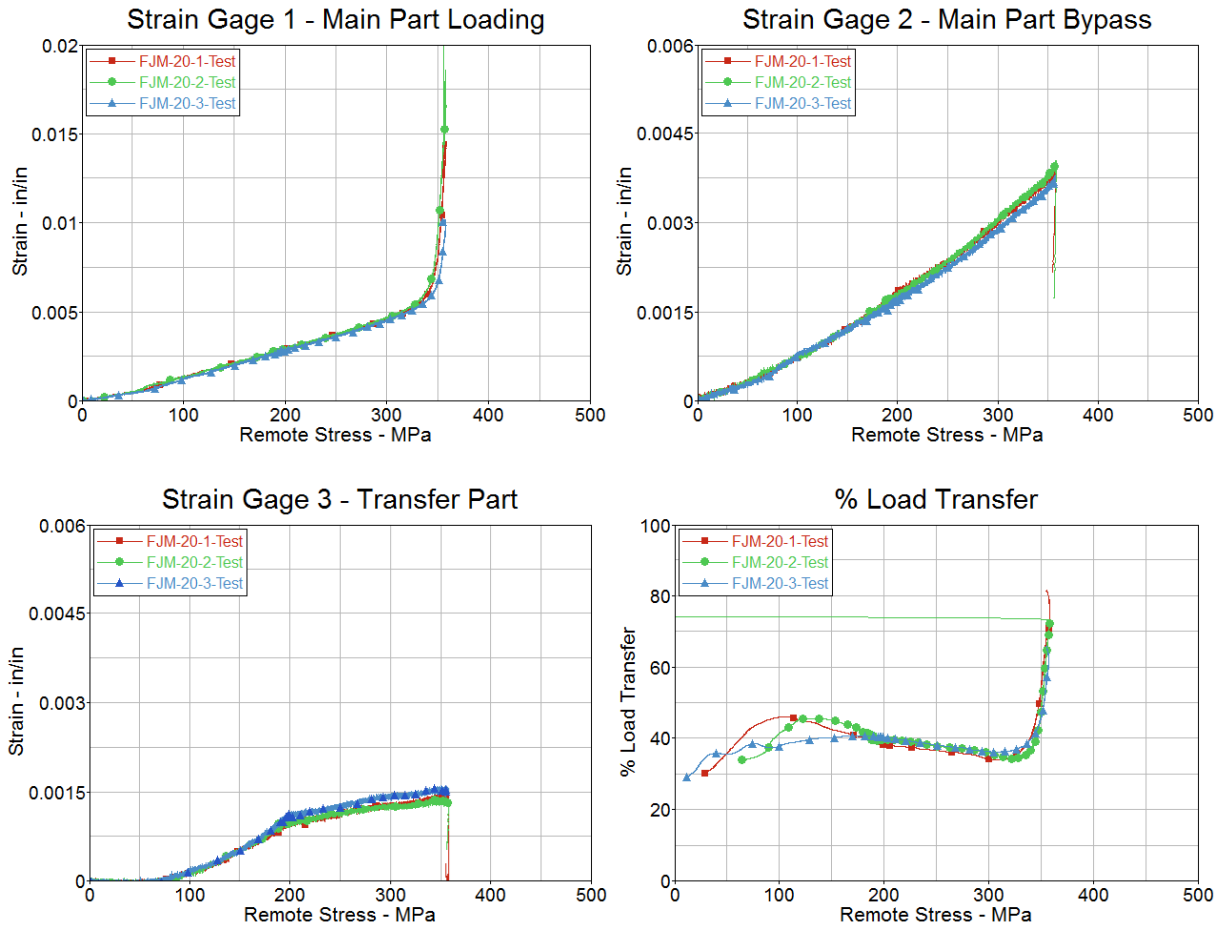


Figure C-2. LT test results at 20 in./s stroke rate

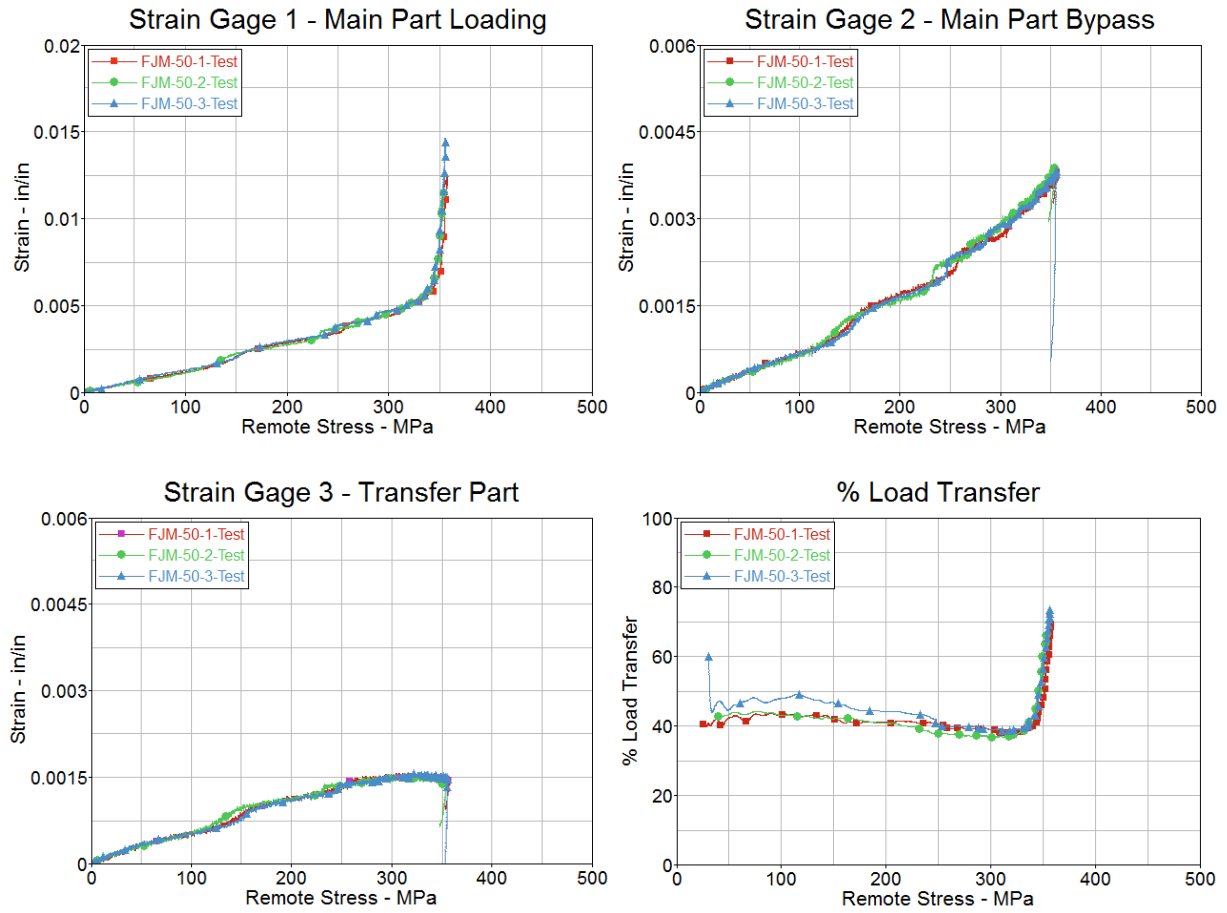


Figure C-3. LT test results at 50 in./s stroke rate

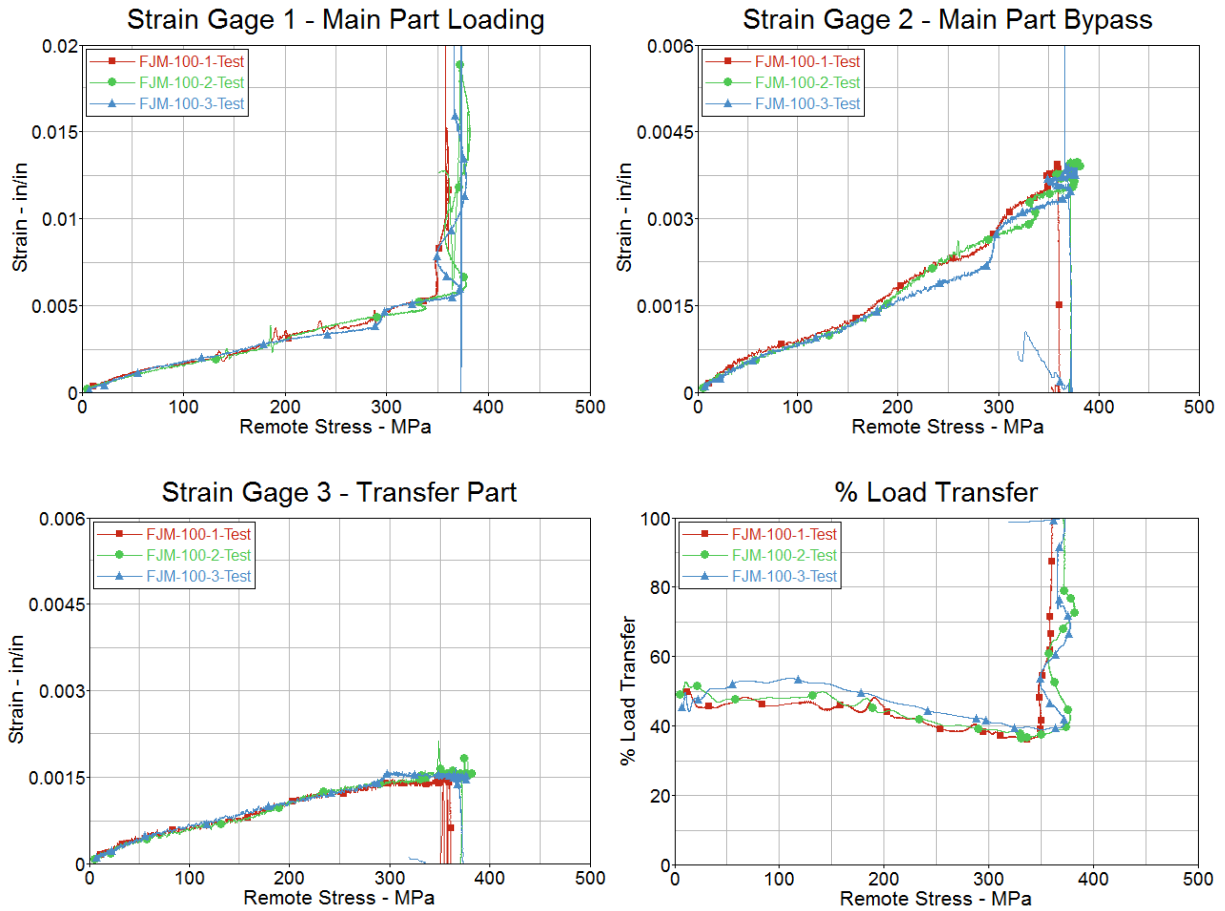


Figure C-4. LT test results at 100 in/s stroke rate

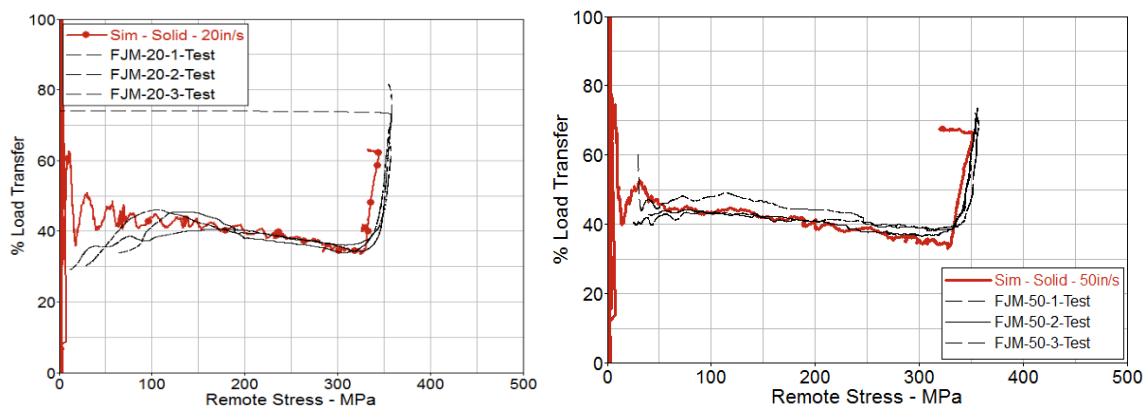


Figure C-5. LT comparison of DJM results to test results at 20 in/s and 50 in/s stroke rate

APPENDIX D—STRAIN COMPARISON FOR HIGHER STROKE RATES

Comparison of strain results for a detailed three-dimensional (3D)/solid joint finite element (FE) model (DJM) and test at quasi-static, 20 in./s, and 50 in./s stroke rates. Strains from the simulations do not reflect the oscillations seen on the test data. The sensitivity of the slack inducer (SL) has been documented, and the differences seen in the strains could be due to the simplification of the SL model.

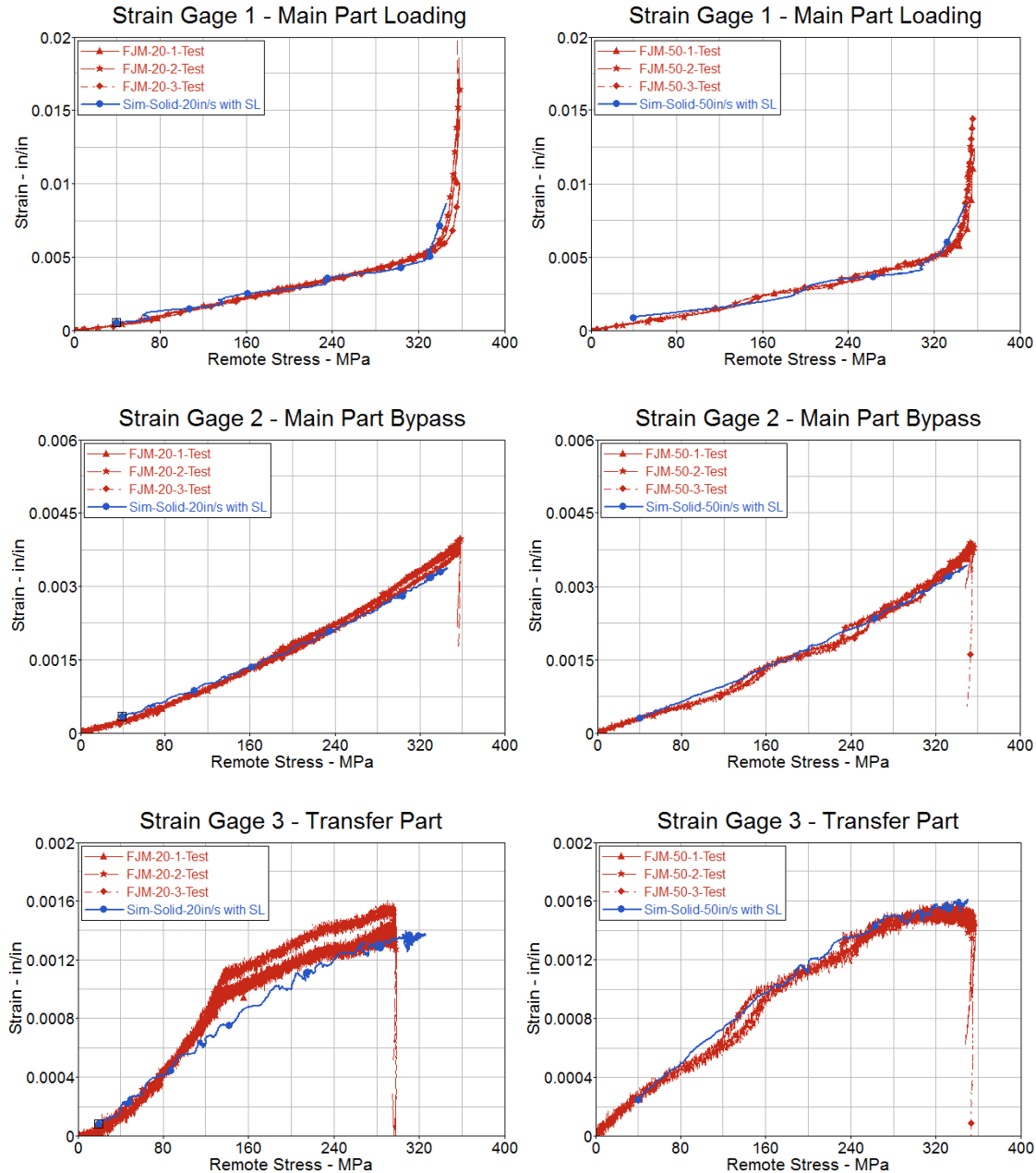


Figure D-1. Strain comparison for DJM results including SL and test results at 20 in./s and 50 in./s stroke rate

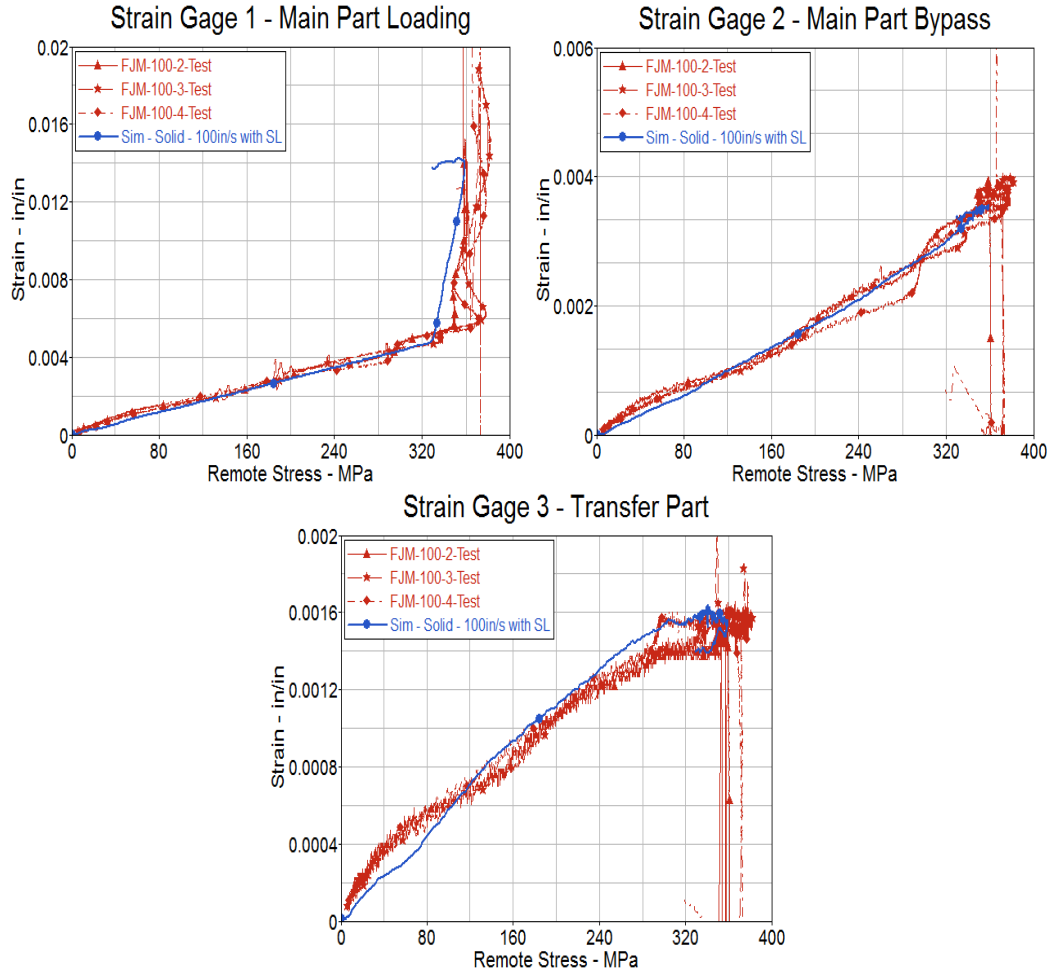


Figure D-2. Strain comparison for DJM results, including SL and test results at 100 in./s stroke rate